UNDERSTANDING THE EFFECTS OF SURFACE TEXTURING ON THE HEAT TRANSFER CHARACTERISTICS OF SPRAY COOLING

A dissertation
submitted to the faculty of the
University of Minnesota

by

Sankarganesh Muthukrishnan

IN PARTIAL FULFILLMENT OF THE REQUIREMENTS
FOR THE DEGREE OF DOCTOR OF PHILOSOPHY

Vinod Srinivasan, Advisor

November 2021

Acknowledgments

I would like to thank my advisor, Professor Vinod Srinivasan, for his guidance and support throughout my doctoral studies at the University of Minnesota, Twin Cities, and the Indian Institute of Science (IISc) Bangalore, India. I appreciate his patience in affording me the flexibility to develop my research at my own pace and offer timely counsel when required while simultaneously providing me with opportunities to explore and evolve my teaching capabilities. I sincerely appreciate his ethical behavior and foresight in offering me an opportunity to work on different topics, thus, helping me get familiarized with a diverse range of topics within heat transfer. I am very grateful to my doctoral committee members, Prof. Terrence Simon, Prof. Satish Kumar, and Prof. Jiarong Hong, for taking their time off their busy schedules and providing a platform for communicating creative thoughts and criticisms. My special thanks to Prof. Richard J. Goldstein and Prof. Terrence W. Simon believed in my teaching potential and provided me an opportunity to be their Teaching Assistants during my first year of Ph.D. It is also my pleasure to have been a TA for Prof. Jiarong Hong, Prof. Matt Anderson, Prof. John Bischof, Prof. Alptekin Aksan, Prof. Frank Kelso, and Prof. Allison Hubel. The lessons (both academic and non-academic) and values that I learned from them will help in my life and career.

My sincere thanks to the CSE research shop members, Patrick Nelson, Ron Boystrom, Bob Jones, William Gruhlke, and Peter Ness for their technical help and support fabricating my experimental setup. My deepest gratitude to all the Minnesota Nano Center members, especially Tony Whipple, Lage Von Dissen, Wanjohi Kimani, Mark Fisher, Laura Parmeter, Glenn Kuschke, Bashir Jama, and Gregory Cibuzar, for aiding and assisting me in fabricating my samples for experiments. Special thanks to Vince Genova and Thomas

Pennell of the Cornel Nano-fabrication labs for helping me with sample fabrication. My deep appreciation to Ben Guengerich and Peter Zimmerman (Polaris Student workshop) for their help and assistance in using 3D printing, waterjet, laser-cutting, and other mechanical equipment in the ME department. I am grateful to Richard (Nistar) Maharaj and Mike for offering their helping hands and random morning/evening small talks, which motivated me to be a better person. My sincere thanks to John Gardner for his guidance and support throughout my Ph.D. program. My deepest gratitude to Ian Wright, Naveen Bhati, Kavinesan Karpaya, Rilyn Fox, and Xijun Tan for putting extra effort into getting my experimental setup up and running. Special thanks and gratitude to Ian Wright for being helping me acclimate to the Minnesotan weather and culture.

My warmest regards to my fellow graduate students and friends – Ankit Saini, Manish Sachdeva, Gaurav Nayak, Daniel Escobar, Umesh Madanan, Roshan Ranganathan, Chinmayi Band, Akash Dhotre, Merin A P, Krishna Chandra, Amey Joshi, Arpan Chatterjee, Jinwei Yang, Santhosh Kumar Sankar, Biswaranjan Mohanty, Abhinav Tripathi, Sampreeti Jenna, Sakshi Arya, Guru Venkatesan, for their helping, motivating, and critically discussing academic and non-academic topics with me. My heartfelt thanks to Abhay Ladhe, Sarita Hardas, Deepti Verma, Ujval Umesh, Thrilok Nagamalla, Kshitij Karki, Jaan Sharma Pathak, Lalitha Belur, Nikhil Jain, Charu Sharma, Pranav Suri, Satya Bharadwaj, Pooja Sudharshan, Jaden Evenson, Mohan Chettiyar, Shyam Gannavaram, Shivam Sharma, Elizabeth Arnold, and Kelsi Lynde for making me feel at home in Minnesota. My sincere gratitude to my friends from IISc Bangalore – Muthukumar Mariappan, Anamika Singh Pratiyush, Jeet Kumar Gaur, Bhavin Rathod for their continued support and appreciation throughout my Ph.D. program. To my evergreen friends, Prakash

Thirunavukkarasu, Karthik KRD, Santhana Bharathy, and Kamalkannan Kannaiyan – a million thanks to you all for standing by my side during the most challenging times and struggles.

Last but not least, I wholeheartedly thank my mom (Jyothi Vardhani), dad (Muthukrishnan), younger sister (Vidya), brother-in-law (Prasanna Venkatesh) and other relations for their love, care, affection, unwavering support, and encouragement throughout my research career. This thesis and career would not have been possible without their sacrifice and blessings. Special thanks to my Fiancé (Narayani) for her love, affection, and patience during recent and unpredictable times in India.

Dedicated to my dad

Abstract

Enhanced surfaces show improved heat transfer characteristics in the two-phase regime due to enhanced capillary action near the contact line region. The role of contact-line evaporation on spray impingement heat transfer is systematically studied by spraying de-ionized water on silicon substrates with micropillar arrays. The pillar height, the pillar diameter, and the pillar spacing of the micropillar array were varied from *5 to 50 μm* while keeping the porosity constant at *0.75*. An air-assisted nozzle was used to create a liquid spray with a Sauter Mean Diameter of *~ 35 μm* depending on flow conditions. Most test runs were conducted at a water flow rate of *30 ml/min* and an air-liquid mass flow rate ratio of *~ 0.57*. Temperature and heat flux data were processed to estimate the macroscale heat transfer parameters, including critical heat flux (*CHF*), heat transfer coefficient (*HTC*), and peak cooling efficiency. The results show a continuous increase in the critical heat flux (*CHF*) as the pillar diameter is decreased until a pillar diameter of 5 μm. Below *d = 5 μm* (i.e., for *d = 2 μm and 0.8 μm*), a monotonous decrease in the heat transfer performance was observed. Likewise, the effects of pillar height were non-monotonic, with CHF and peak heat transfer coefficient attaining a maximum as the height-to-diameter ratio approaches unity (*h/d ~ 1*). The transition from Cassie–Baxter state to Wenzel state is critical for liquid penetration into the forest of micropillar array. Surfaces with *2-μm* and *0.8-μm* pillar arrays exhibit inferior cooling performance due to low liquid penetration.

Silicon substrates containing *5-μm* and *10-μm* pillar arrays (const. *h ~ 8 μm*) with varying pillar spacing (*p ~ 0.2d, 0.5d, 1d, 1.5d, 2d*) were fabricated to investigate the role of pillar spacing on the spray cooling performance. Each pillar-array geometry tested has a CHF maximum for pitch-to-diameter ratio (*p/d*) of ~ 1. Based on the results obtained and insights gained, surfaces with pillar diameter (*d*) ≈ pillar spacing (*p*) ≈ pillar height (*h*) is preferred. Overall, *5-μm* and *10-μm* arrays with *h/d ~ 1* yielded some of the maximum performance values for the given flow settings. The Cassie–Baxter state to Wenzel state transition theory stands valid for surfaces with small pillar spacing, i.e., *p/d < 1*. On the other extreme, in-plane Laplace pressures become essential to ensure complete wetting. Hence, pillar-arrayed surfaces with *p/d > 1* show diminishing results.

The effect of liquid flow rates and air flow rates were also investigated independently using textured surfaces. Values of CHF as high as *830 W/cm^2* were achieved with a water flow rate of *82 ml/min*, along with cooling efficiency of 49%.

High-speed images containing crucial information on the solid/liquid/vapor interface were obtained Total internal reflectance (TIR) technique. A sapphire substrate with indium tin oxide (ITO) heater was used as a substrate. For the first time, high-temperature experiments (*T > 120 ºC*) were performed using plain surface and *10-μm* pillared surface. Images were processed to obtain contact-line parameters such as wetted area fraction, and contact-line perimeter per unit area. Time-averaged results reveal the superior performance of the *10-μm* pillared surface is due to the enhanced wicking capabilities of the micropillar

configuration at elevated heat flux values. The time-series data of wetted area fraction plotted for both plain and *10-μm* surface show that the CHF occurs when the evaporation time scale is less than the re-wetting time scale. With wicking enhancement and faster in-plane capillary suction flows, the *10-μm* surface was able to maintain the re-wetting time scale to be lower than the evaporation time scale, thereby delaying CHF to a value 35% greater than that of plain surface CHF. From the model presented, it is clear that the substrate approaches CHF when the heating time scale of the substrate is equivalent to the liquid imbibition time scale.

Table of Contents

List of Figures

List of Tables

Nomenclature

ALR	Ratio of air to liquid mass flow rates
A_{chip}	Area of the chip
C_p	Specific heat capacity of liquid
d_{32}	Sauter Mean Diameter, $d_{32} = \frac{\sum_i d_i^3}{\sum_i d_i^2}$
h_{fg}	Latent heat of vaporization
h	Heat transfer coefficient
k	Thermal conductivity of chip
$\dot{m}$"	Mass flow rate per unit area or mass flux
q"	Heat flux
Q_{net}	Net heat input to the chip
Q_{in}	Heat power input supplied by the voltage supply
Q_{loss}	Heat loss from the chip due to conduction and natural convection.
Re	Droplet Reynolds number
T_i	Inlet temperature of the liquid coolant
T_m	Temperature measured by the thermocouple junctions
T_s	Surface temperature of the chip

t_{chip}	Thickness of the chip
We	Weber Number ($We = \rho V^2 d_{32}/\sigma$)
ρ	Air density, kg/m^3
η	Cooling efficiency

Chapter 1

Introduction

1.1 Background

Over the last three decades, advances in the field of nanofabrication have successfully scaled down transistor sizes to tens of nanometers, enabling electronic systems to become smaller and faster. For example, an Intel (Quad) Core^{TM} i7 processor with a clock speed of *1.7 GHz* has more than 2.6 billion transistors within a square area of *7 cm^2*. On the other hand, drastic miniaturization of these chips has led to higher packing density, contributing to more power dissipated per unit area. Furthermore, progress in parallel processing heightened the non-uniformity in power distribution within these processors, leading to non-uniform temperature distributions. Intelligent thermal energy management solutions are needed to improve reliability and prevent premature failure of these power-hungry processors.

Figure 1.1 shows microprocessor data trends collected over the past 42 years. The crucial parameters collected include the transistor count, frequency, power consumed, and logical cores. Following Moore's law, the transistor count has continued to double every two years. However, the microprocessor's clock speed (shown as the frequency in fig 1.1), which directly relates to its processing speed, has saturated. This stagnation in the microprocessor's clock frequency, for almost 15 years, is due to the constraints in the processor power consumption set by the heat transfer limits *(~100 W/cm^2*) of current

cooling technologies. Further, the development of GaN-based power electronics such as radar, power switching devices, and avionics systems, has led to higher dissipation than Si-based electronics (~ *1000 W/cm*^{2}) [6]–[8].

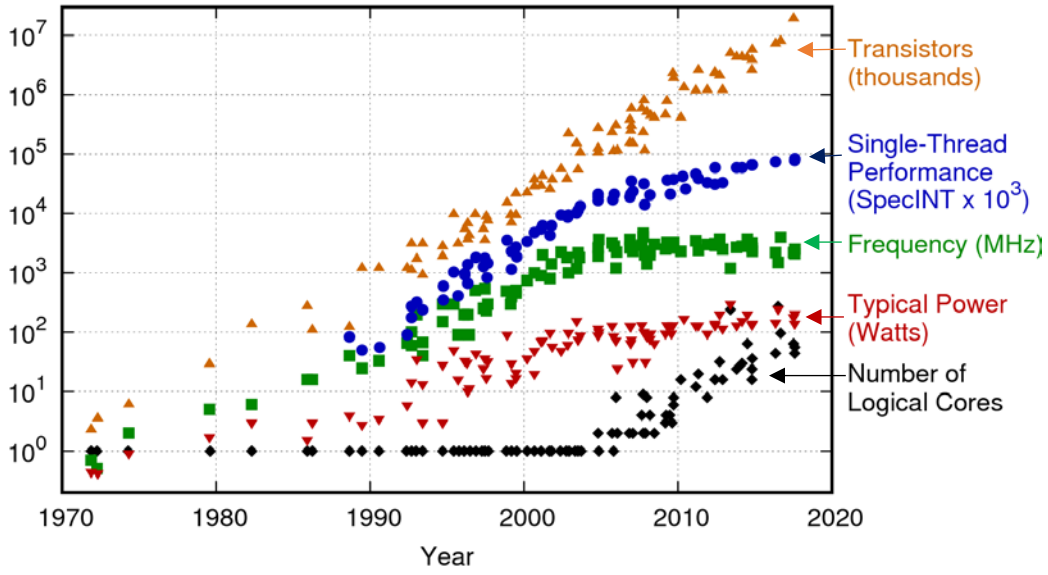

[9]**Fig. 1.1 Microprocessor trend data collected over 42 years. Original data up to 2010 was gathered and plotted by M. Horowitz, F. Labonte, O. Shacham, K. Olukotun, L. Hammond, and C. Batten. New plot and data collected for 2010-2017 by K. Rupp (Image source: www.karlrupp.net)**

Commercially available state-of-the-art direct cooling technologies include immersion cooling [10], heat pipes [11], micro-channels [12], [13], evaporative cooling [14], [15], jet impingement [16], and spray cooling [3], [9], [17], [18]. Effective cooling mechanisms are required to remove excess heat while maintaining an optimum temperature (below *65°C*) conducive to safe operation [19]. Amongst all the two-phase cooling technologies, spray cooling has the inherent advantage of maintaining uniform surface temperature while using a limited liquid inventory [20].

Liquid sprays generated by breaking down the liquid bulk into tiny droplets by applying enough kinetic energy to overcome the surface tension forces. This process of generating sprays is called atomization. Commercially, several atomizers (or spray

nozzles) are available, including pressure atomizers, rotary atomizers, air-assisted atomizers, electrospray atomizers, etc. The spray cooling process commences with the generation of liquid spray, followed by the spray impact on the heated surface directly. Upon impact, droplets may spread over the surface and evaporate or merge to form a thin liquid film [3]. At high heat fluxes, the thin liquid film extending over the heater surface can absorb large amounts of heat energy. If sufficiently thin, the liquid film maintains surface temperatures below the maximum allowable levels. The heated liquid film either evaporates or is swiftly washed away by the fresh influx of liquid owing to the high volumetric flow rates of the liquid supplied by the spray nozzle.

In general, the process of spray cooling is dependent on numerous parameters, and these parameters can be broadly categorized as *(a) fluid properties, (b) spray characteristics, and (c) surface roughness/chemistry.* Due to the polydispersity of sprays and non-uniformity in the volumetric flux distribution, spray characteristics can be controlled only to a limited extent to improve the cooling performance. For a vertical, downward directed spray under the earth-gravity, some of the critical spray parameters are:

1. *Sauter Mean Diameter (SMD):* Sauter Mean Diameter is the characteristic diameter of a sphere with the same volume/surface area ratio of the entire spray. In atomization and combustion, SMD (d_{32}) is used to characterize the mean diameter of the spray.

$$d_{32} = \frac{\sum n_i d_i^3}{\sum n_i d_i^2} \tag{1.1}$$

SMD is an important spray parameter that primarily depends on the nozzle orifice diameter (d_0), the nozzle pressure drop (ΔP), viscosity (μ_l), and surface tension (γ) of the liquid.

2. *Volumetric flux (Q"):* Volumetric flux is the volume flow rate of liquid per unit surface area. The mean droplet velocity does not account for the cumulative effect of multi-

droplet impact and is often not measured in most heat transfer studies. Hence, volumetric flux is widely used. It has the same units of mean droplet velocity (m/s) and is easy to correlate with other spray cooling parameters.

$$Q" = \frac{Q}{A} \tag{1.2}$$

Where Q is the volume flow rate of the liquid, A is the cross-sectional area of the heater surface.

1.2 Motivation

Modern-day applications such as autonomous vehicles, artificial intelligence networks, big-data projects, cryptocurrencies, and intelligent power grids rely on massive, energy-intensive data centers to perform sophisticated computations. In 2020, data centers consumed around *1%* of the global electrical power consumption and released carbon footprints equivalent to that of the airline industry [21]. The power distribution pattern within a typical data center shows over *50%* power expenditure for cooling [22]. Reliance on conventional air-conditioning systems with a large fraction of electrical power devoted to air-compression and cooling, leads to high overall power expenditure for cooling. Maintaining optimal operation temperatures while removing large amounts of heat generated is essential for safe and reliable operation. Besides the poor thermal performance, these centralized air-cooling systems fail to address the demand for large heat flux removal (~ *100 - 1000 W/cm*^{2}) with high heat transfer coefficients.

Among the available cooling techniques, spray cooling is an attractive option that could remove a large amount of waste heat through latent heat of vaporization. Some of the noteworthy applications uses liquids sprays to achieve superior cooling performance are freeze/flash drying with Liquid N_2, cryogenic cooling in laser surgery, quenching in metal

processing, X- ray medical devices, supercomputers [3], [18], [23]. Often, the spray cooling research community were motivated to increase the upper limit of the thermal runaway using high coolant flow rates, surface texturing, nozzle orientation, and nozzle multiplexing. However, very few of those research works strive to explore the underlying thermo-fluidic interfacial phenomena and delineate the complex thermophysical mechanisms affecting spray cooling performance. The overarching aim of this thesis is to study the role of surface roughness on the thermal performance and probe into the phase change dynamics of spreading coolant using experimental methods.

1.3 Organization of thesis

The present chapter discusses the current trends in microprocessor's architecture and demand for implementation of two-phase cooling techniques such as spray cooling to remove large amounts of heat flux from these devices.

Chapter 2 presents the critique of spray cooling literature from a technical perspective. Issues and challenges associated with tweaking the spray cooling performance parameters to obtain superior thermal performance were discussed. At the end, the objectives of this thesis are discussed in detail.

Chapter 3 outlines the fabrication process used to modify/create the surface topology on top of silicon and sapphire wafers. This chapter demonstrates the spray cooling test-rigs used for capturing the thermal performance of textured surfaces.

Chapter 4 showcases the cooling curves obtained for all the surfaces tested. Heat transfer data were processed to obtain thermal performance parameters near the peak heat flux and plotted against the pillar geometric parameters to obtain a conjecture that explains the role of localized contact-line dynamics on the global heat transfer performance.

Chapter 5 discusses the spray cooling test results obtained for the surfaces containing micropillars with varying pillar spacing. A discussion was laid out to explain the potential reasons for the superior performance of surfaces with optimum pillar spacing. Results obtained for varying water/air flow rates are included in this chapter.

Chapter 6 discuss the experimental methodology for the Total Internal Reflectance Microscopy (TIRM) experiments. Results pertaining to Contact-line parameters like contact-line perimeter and wetted area are plotted for both plain and textured surfaces. Importance of contact-line evaporation was discussed in detail with experimental evidence.

Chapter 7 concludes the thesis by summarizing the vital results obtained during this work and paves way for the future work.

Chapter 2

Literature Review

2.1 Introduction and Background

The process of spray cooling and the progress made in the study of spray-wall interaction are described in several review papers [2], [3], [18], [24], [25]. The spray cooling process is a complex phenomenon bringing together fluid-flow/heat transfer mechanisms such as droplet impingement and spreading, menisci coalescence, liquid-film formation, evaporation, and surface nucleation. To understanding the droplet spreading and evaporation phenomena, let us consider a liquid meniscus spreading over a wetting surface ($\theta_Y < 90°$) under the influence of gravity (see fig. 2.1a). Based on the liquid film thickness (δ), the liquid meniscus can be divided into three regions:

- *Adsorbed film region,* where liquid molecules are firmly held to the solid surface through attractive van der Waals forces.
- *Bulk or 'macroscopic' region,* defined as the region where $\delta > 0.1\ \mu m$.
- *Transition or 'contact-line' region, which* lies between the bulk region and the adsorbed film region.

For a given liquid, the transport processes in the contact line region are regulated by the intermolecular forces of attraction between the solid and the liquid molecules and the curvature of the interface. The variation of the adhesion forces, the curvature, and the thermal resistance are shown in fig. 2.1b. Adhesion forces experienced by the liquid

molecules (also known as disjoining pressure, Π_D) can be modeled using Lennard – Jones potential and is given by

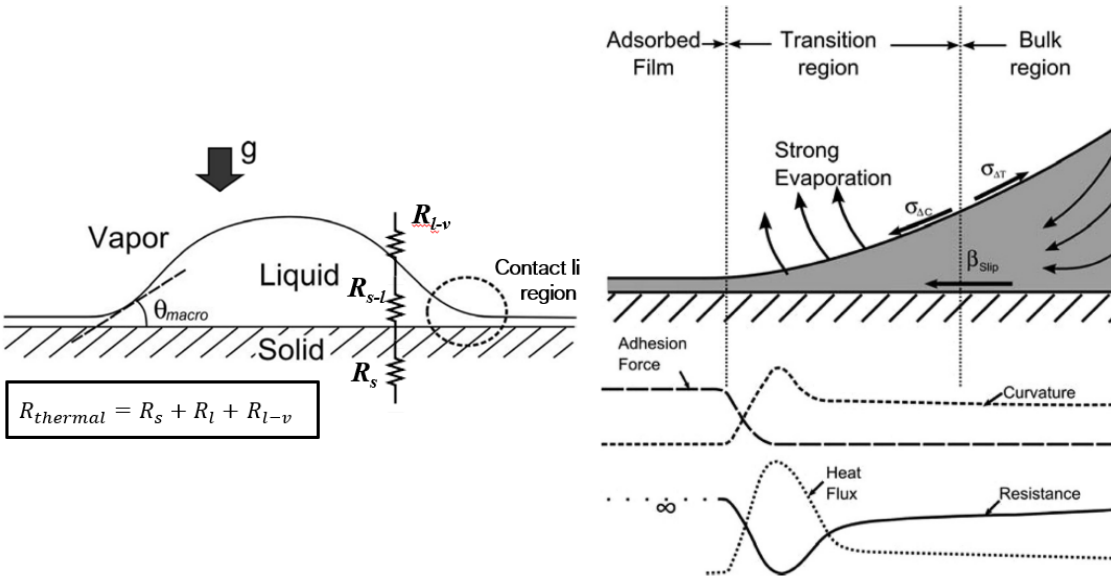

Fig. 2.1 (a) Schematic of a liquid droplet on a surface (b) Zoomed view of the contact line region - showing the variation of the adhesion force, the liquid-vapor curvature, the heat flux, and the thermal resistance at the contact line region during evaporation [1].

$$\Pi_D = -\frac{A_H}{6\pi\delta^3} \tag{2.1}$$

where A_H is the Hamaker constant. From a heat transfer perspective, the hindrance to the evaporation process can be modeled as the summation of three thermal resistances in series (fig. 2.1a) – (1) the conduction resistance (R_s) of the solid (usually designed to be very low), (2) the conduction resistance of the liquid (R_l), and (3) the interfacial heat transfer resistance at the liquid-vapor interface (R_{l-v}).

In the adsorbed film region, the disjoining pressure of the liquid film is enormous, and therefore, the overall thermal resistance to evaporation is very high [1], [26], [27]. Thus, very little evaporation occurs in this region. On the other side, the liquid film thickness is relatively high in the bulk region, offering high thermal resistance to heat conduction at the solid-liquid interface. In the transition region (or contact-line region), the

overall thermal resistance reaches its minimum due to limited conduction resistance because of small liquid film thickness and declining interfacial resistance. For this reason, the evaporation mass flow and hence, the rate of heat transfer is very high in the contact-line region. As the liquid mass evaporates, the gradient in the liquid film thickness and interfacial curvature along the film enables the liquid in the bulk region to flow towards the contact-line region through capillary and intermolecular forces, thereby replenishing the dry spots.

Single sessile droplet impinging dry or wetted surface is a key element for understanding spray/wall interactions [28]. The impingement of single drops onto a heated wall was experimentally investigated in a large number of studies [29]–[35]. Mostly, Weber ($We = \rho V^2 d_{32}/\sigma$) number and Reynolds ($Re = \rho V d_{32}/\mu$) number were used as a reference to categorize the hydrodynamic outcomes after droplet impact on a solid surface. Khavari et al. [8] showed that the droplet adheres and spreads over the surface to form a thin liquid film at low Weber numbers (We < *100*). On the other hand, at higher Weber numbers, the droplet may fragment through bubbly, fingering, or Leidenfrost boiling regimes depending on the wall temperature. Negeed, Takata, and co-workers [36], [37] presented a dimensionless group ($K_d = We^{0.5} Re^{0.25}$) and found that K_d is influential in determining spreading/fragmentation characteristics of a impacting droplet. – with lower values of K_d causing spreading and $K_d > 50.2$ causes fragmentation. Staat et al. [34], [35] found that low wall temperatures (< *150°C* for ethanol) and low Weber numbers (We < 300) lead to droplet deposition; whereas, higher wall temperatures and/or Weber numbers may lead to droplet bouncing, contact-splash, and film-splash regimes. Breitenbach et al. [2] classified the hydrodynamic outcomes of water droplet ($D_0 = 2.2$ *mm*) impinging a hot

surface into four categories (shown in fig. 2.2) – droplet deposition and spreading, droplet dancing, thermal atomization, and droplet rebounding. The corresponding drop impact outcomes were mapped in fig. 2.3 for different impact velocities and surface temperatures studied.

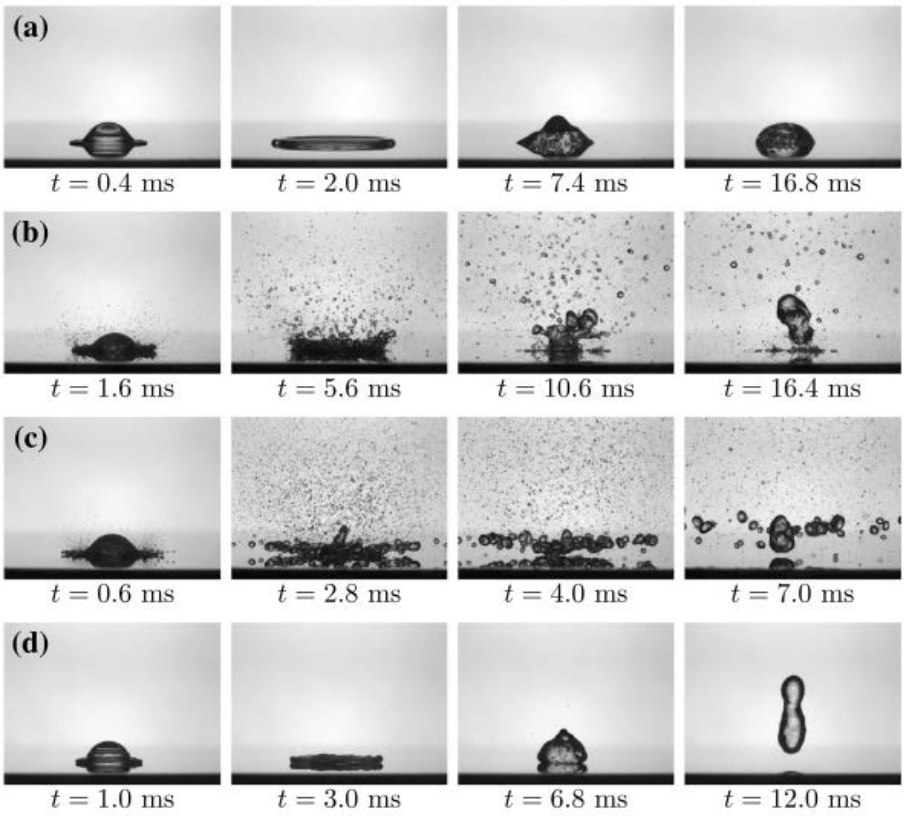

Fig. 2.2 Water drop impact onto a hot substrate: (a) drop deposition and spreading (T_{w0} = 120 ºC , U_0 = 1.5 m/s, D_0 = 2.2 mm), (b) drop dancing (T_{w0} = 170 ºC , U_0 = 0.7 m/s, D_0 = 2.2 mm), (c) thermal atomization (T_{w0} = 260 ºC , U_0 = 1.7 m/s, D_0 = 2.2 mm), and (d) drop rebound (T_{w0} = 280 ºC , U_0 = 0.7 m/s, D_0 = 2.2 mm) [2]

Hence, for achieving high heat transfer rates, it is preferable to operate at low Weber numbers to assist droplet adhesion and spreading to form a thin liquid film with thicknesses less than $10\,\mu m$. However, typically high velocities are required to produce small droplets, making low Weber numbers non-trivial to attain. These results also imply that there may be a tradeoff between droplet velocity and diameter for the reduction in droplet bouncing. Despite the understanding of single-droplet impact phenomena, there is no clear path

forward to extrapolate the heat transfer in such canonical situations to the complex process of spray cooling, in which the droplet distribution is a function of time and space [38].

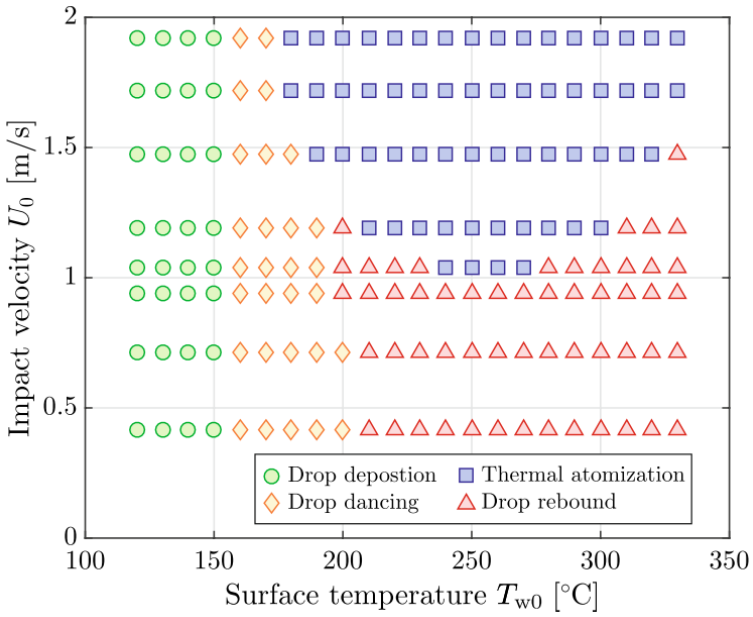

Fig. 2.3 Map categorizing the hydrodynamic outcomes of a single sessile droplet (D_0 = 2.2 mm) approaching the heated surface (@ Temperature, T_{w0}) at different impact velocities [2].

As a result, spray cooling research data continue to be presented in terms of dimensional quantities such as the applied heat flux and the surface temperature. Like pool boiling, data from spray cooling experiments are plotted between the applied heat flux and wall temperature to obtain a resulting curve known as the cooling curve (see fig. 2.4). The cooling curve comprises three important regimes – *(a) single-phase regime, (b) two-phase regime, (c) CHF and film boiling regime*. In the single-phase regime, forced convection through droplet impingement, turbulent fluctuations, and surface-laden flow removes the heat from the surface. Hence, within this regime, the heat transfer coefficient remains roughly constant and does not depend on the applied heat flux. As the surface temperature approaches the saturation point, the cooling curve deviates from its linear behavior, marking the onset of the two-phase regime via phase change. In the two-phase regime, the

liquid film deposited on the hot surface through droplet impingement can absorb a large amount of heat energy via latent heat of vaporization. Due to less thermal resistance, most liquid-vapor phase change (or evaporation) occurs at the three-phase contact line regions where the solid, liquid, and vapor phases meet.

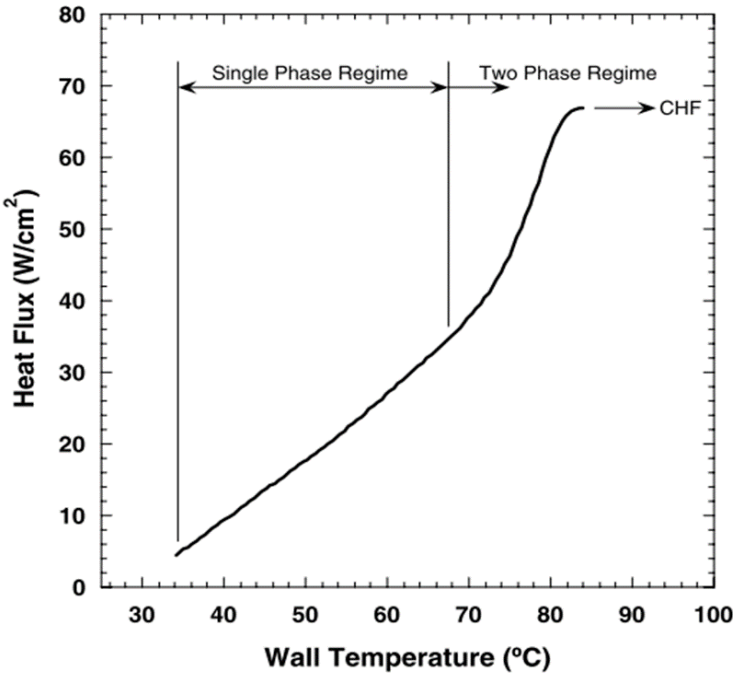

Fig. 2.4 Typical spray cooling curve showing three heat transfer regimes – single-phase, two-phase, and CHF
(FC-72, *93 ml/min, 1.0 bar, T_{sat} = 57°C, ΔT_{sub} = 28°C, 2 cm^2* copper heater) [3]

In spray cooling, the liquid-vapor phase change may occur in two ways – liquid-vapor evaporation at the free-surface of the liquid film and nucleation boiling within the film at the solid-liquid interface. However, bubble nucleation is mostly observed and reported in situations where the heater surface is flooded. When the surface temperature is above the saturation temperature, isolated bubbles form on the solid-liquid interface at preferred locations called nucleation sites. For a vapor bubble of radius R to grow, the minimum amount of superheat required is given by [39]

$$\Delta T = T_g - T_{sat} \approx -\frac{2\sigma T_{sat} v_g}{R h_{fg}} \quad (2.2)$$

where T_g is the temperature inside the vapor bubble, T_{sat} is the saturation temperature of the liquid, σ is the surface tension of the liquid, R is the vapor bubble radius, $h_{fg}$is the specific latent heat of the liquid, v_g is the vapor pressure inside the bubble. In spray cooling, most of the bubbles formed at the solid-liquid interface are washed away by incoming liquid spray through forced convection; rarely, bubbles leave the free surface through buoyancy. At higher superheat, more nucleation sites are activated. As a result, more bubbles are formed and depart the surface rapidly, leading to very high heat transfer rates. Almost all the nucleation sites are active at very high superheats, leading to overcrowding of bubbles at the heater surface. Eventually, interference and coalescence between nearby bubbles may create intermittent dry-out spots leading to a drastic reduction in local heat transfer rate. Any further rise in the superheat would enable the dry-out region to grow and cover more significant fractions of the heater surface.

Consequently, the heat transferred through phase change ceases to increase further. At this point, heat energy removed from the heater surface matches the maximum heat removal capability of the liquid. This critical limit in heat flux is famously known as the critical heat flux (CHF). In spray cooling, CHF is often associated with an abrupt rise in surface temperature and a sudden drop-in the heat transfer rate while causing severe damage to the structural integrity of the heater. Among the numerous spray cooling performance parameters, the following are critical.

1. *Critical Heat Flux (CHF)* – CHF represents the thermal limit of the spray cooling phenomenon. Beyond CHF, the heat transfer performance reduces considerably, leading to

overheating of the surface. Hence, a comprehensive understanding of the CHF phenomenon is essential and plays a significant role in the design of the heater surface.

2. *Heat Transfer Coefficient (HTC)* – HTC is a proportionality constant between the heat flux and the wall superheat (i.e., $\Delta T = T_s - T_i$). For the spray cooling process, the heat transfer coefficient is generally defined as

$$h = \frac{q"}{T_s - T_i} \tag{2.3}$$

where $q"$ is the heat flux value, T_s is the surface temperature, T_i is the liquid temperature.

3. *Spray cooling efficiency (η)* – The spray cooling efficiency is defined as the ratio of the applied heat flux to the overall heat transfer capability (including both sensible heat and latent heat) of the liquid [3].

$$\eta = \frac{q''}{\dot{m}" \left[\left(c_{p,l}(T_s - T_i)\right) + h_{fg}\right]} \tag{2.4}$$

Unlike CHF and HTC, the expression for spray cooling efficiency interlinks both the fluid properties and the heat transfer parameters. Thus, spray cooling efficiency can also be useful in comparing the heat transfer characteristics of two dissimilar surfaces.

2.2 Heat transfer mechanism in the single-phase regime

In the single-phase regime, flow agitation due to droplet impingement and thin-film convection is the dominant heat transfer mechanisms. Pautsch and Shedd [40], [41] developed a heat transfer model based on the superposition of two heat transfer mechanisms - convection in the droplet impact region and thin-film boiling outside the droplet impact region. Experiments were conducted using FC-72 liquid sprays generated by single and multiple swirl-atomizing full-cone nozzle arrays to validate this model. The

experimental results were consistent with the empirical model proposed. However, the spray characteristics of the nozzle were not presented in detail. Since the spray characteristics play a crucial role in the heat transfer process, more studies are required to check the universal validity of the model.

Shedd [4] hypothesized that the heat transfer performance of spray cooling largely depends on the behavior of the thin liquid film. He proposed that the thin film can be modeled as a two-layered turbulent liquid layer - thin viscous sublayer (δ_v) and highly turbulent liquid layer (refer fig. 2.5). The viscous sublayer starts at the wall and extends to the region where there is limited or no flow disturbance due to droplet impingement. At the same time, the turbulent layer lies above the viscous sublayer. Flow inside the turbulent liquid layer is primarily driven by shear force induced by the impinging droplets on the free surface of the thin film.

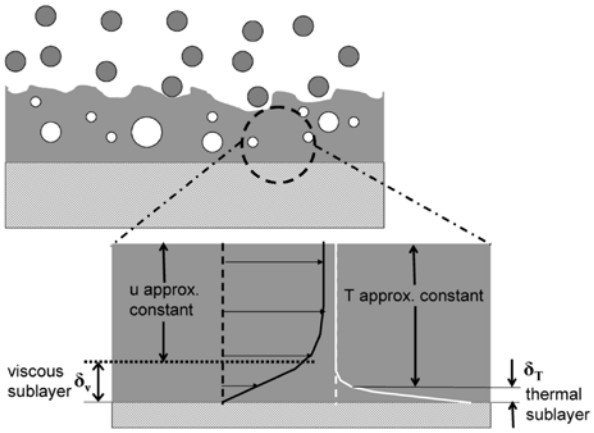

Fig. 2.5 Illustration of the flow field within the thin liquid film as per the heat transfer model proposed by Shedd et. al [4]

For $Pr > 1$, the conduction sublayer (δ_T) is within the viscous sublayer. Hence, the heat transfer coefficient in the conduction sublayer can be modeled (assuming, $\delta_T = \delta_v Pr^{-n}$) as a function of average volumetric flow rate (Q'') as:

$$h = C\ \rho\ c_p\ Q''^{0.5} Pr^{-0.5} \tag{2.5}$$

where the heat transfer coefficient (h) is defined as:

$$h = \frac{k}{\delta_T} = \frac{k}{\delta_v} Pr^n \tag{2.6}$$

and C is a dimensional parameter (units = $m^{0.5}s^{-0.5}$). The value of C is a function of spray system geometry and is determined empirically. For a single nozzle conical spray, C was found to be 0.149 $m^{0.5}s^{-0.5}$ and for four nozzle sprays, C was given by 0.129 $m^{0.5}s^{-0.5}$. Although the empirical data was correlated with an average error of less than 5%, the generality of this model is questionable.

Estes and Mudawar [42] studied the effects of nozzle-to-surface distance on the CHF using FC-72 and FC-87 as coolants. Rybicki et al. [43] extended their work by investigating the cooling characteristics of pressure sprays with PF-5052 as a coolant. The researchers used three different upward-oriented full-cone nozzles to study the effects of flow rate and subcooling. Experimental data from the previous experiments were pooled with the data obtained from the following experiments to obtain an empirical correlation (eqn. 2.7) for the single-phase regime.

$$Nu = 4.7\ Re^{0.61} Pr^{-0.32} \tag{2.7}$$

Here, the Nusselt number and Reynolds number are defined as follows:

$$Nu = \frac{q''}{T_s - T_i} \frac{d_{32}}{k} \tag{2.8}$$

$$Re = \frac{\rho Q'' d_{32}}{\mu} \tag{2.9}$$

where q'' is the heat flux, T_s is the surface temperature, T_i is the liquid temperature, d_{32} is the Sauter mean diameter (SMD), and μ is the dynamic viscosity of the liquid.

Zhao et al. [44] broadly categorized the heat transfer mechanisms into five categories - film formation, thin-film convection, bubble nucleation, droplet-bubble

interaction, bulk convection, and radiation. The authors devised a numerical model based on these five heat transfer mechanisms to simulate the spray-cooling phenomena. To verify their model, both numerical and experimental studies were conducted. The results show that droplet impingement (~ *53%* of total heat transfer) and thin-film convection (~ *38%* of total heat transfer) are the dominant heat transfer mechanisms in the single-phase regime of spray cooling.

2.3 Heat transfer mechanism in the two-phase regime

Spray cooling process is a complex multi-scale phenomenon [2] that depends on various critical factors such as a) spray properties, such as droplet diameter distribution, velocity and number density, b) Macroscale geometry, specified by nozzle-surface spacing, spray cone angle, inclination of spray axis with respect to the surface, and c) near-surface liquid-vapor transport phenomena, such as capillary suction, contact angle, surface roughness morphology and length scales, surface tension and Marangoni effects, as well as bubble nucleation, growth and collapse. Due to additional complexities associated with phase change, dynamic wetting, and temperature gradients, heat transfer mechanisms in the two-phase regime are not entirely understood. However, the following heat transfer mechanisms are successfully identified through empirical studies: *Thin-film evaporation at the contact line, solid-liquid interface nucleation, and secondary nucleation*.

Horacek et al. [5] measured the time and space resolved heat transfer distributions in a spray-cooled surface to study the effects of gas subcooling and thermal subcooling on CHF. Heat transfer measurements were done using an array of individually controlled micro heaters, while the flow visualization to measure the three-phase Contact Line Length (CLL), was made using a Total Internal Reflectance (TIR) based technique. Figure 2.4

shows the variation of CLL per unit area (or CLL density) with the wall superheat and heat flux. The CLL (fig. 2.6a) increases with wall superheat and reaches a maximum at a superheat where CHF occurs. Beyond CHF, CLL decreases as the wall dries out. In addition, fig. 2.6b supports the argument that the CHF happens at the point where CLL density is highest. The authors speculated that the variation in CLL density with the surface temperature might be due to the influence of contact-line heat transfer. However, advanced flow visualization experiments and data-processing algorithms are needed to accurately measure the static and the dynamic wetting parameters and confirm this conjecture.

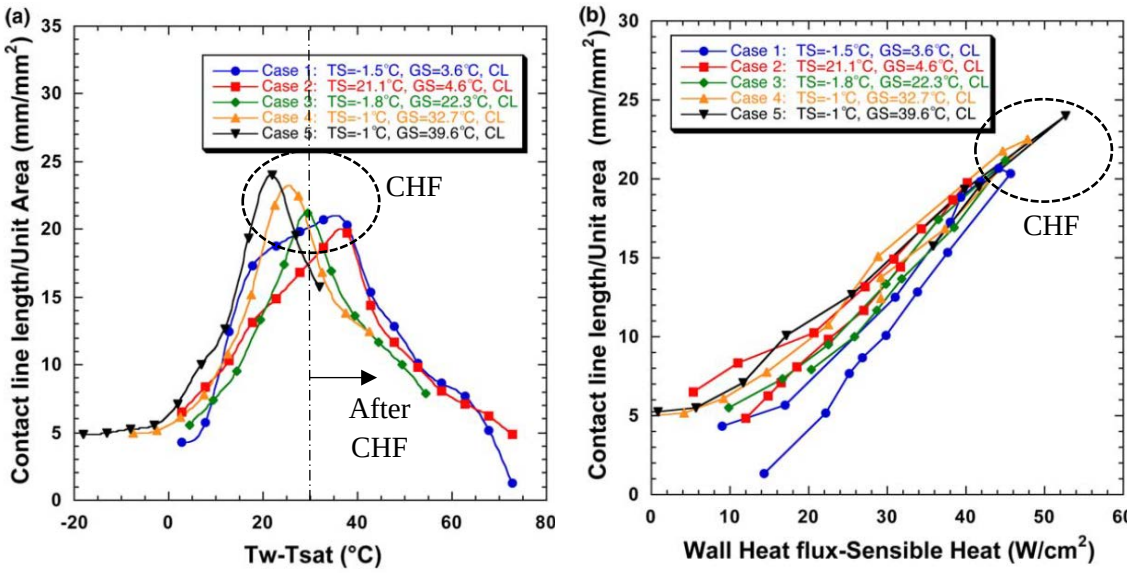

Fig. 2.6 Variation of three-phase contact line length per unit area with (a) wall superheat (left) and (b) wall heat flux minus the sensible heat (right) [5]

Cheng et al. [24] classified bubble nucleation into two types – (a) surface nucleation, which occurs on the heated surface, and (b) secondary nucleation, which occurs on droplet surfaces. When heat is applied, residual gases or vapors trapped inside surface deformities expand and form a bubble. This process is known as surface nucleation. On the other hand, liquid droplets ejected out of the spray nozzle tend to adsorb vapor/gas molecules on their surfaces due to van der Waals's forces of attraction. On impacting the

free surface of the liquid film, the gas molecules carried along by these droplets become tiny bubbles. Consequently, these tiny bubbles tend to act as secondary nuclei and grow as they move closer to the heater surface. This nucleation mechanism is called secondary nucleation.

Rini et al. [45] used FC-72 to perform spray cooling experiments on a semi-transparent synthetic diamond heater. They studied the bubble growth and droplet impact on the bubble behavior by direct visualization using a long-distance microscope. High-speed images of the liquid film were obtained and processed to calculate the bubble size and the bubble lifetime. The authors reported that both surface nucleation and secondary nucleation influence the characteristics of the spray-cooling heat transfer in the two-phase regime. They also claimed that the nucleation site density is higher in spray cooling (*~1000 – 4044 /cm^2* with bubble diameter about *174 – 282 μm*) than in pool boiling (~900 */cm^2*). The growth cycle of surface nucleation was observed to be the same as that in pool boiling, meaning that the present heat transfer models for pool boiling are applicable to spray cooling as well. Hence, they argued that the difference in the nucleation site density between spray cooling and pool boiling is due to secondary nucleation in spray cooling. Their results indicate that the phase change process due to surface nucleation accounts for only *38 – 49%* of the total heat transfer, and the rest is due to secondary nucleation. However, details about the image processing technique used for counting the nucleation site density are not available in their paper.

Formulating an empirical correlation in the two-phase regime is an arduous task due to the complex processes involved in phase change cooling experiments. Only a few such correlations exist in the spray cooling literature. Based on the empirical data, Hsieh

et al. [46], [47] proposed the following heat transfer correlation for spray cooling with water and R134a in the two-phase regime.

$$\text{R134a:} \quad Bo_m = 2.1\, We^{0.66} Ja^{1.51} \tag{2.10}$$

$$\text{Water:} \quad Bo_m = 15.6\, We^{0.59} Ja^{1.68} \tag{2.11}$$

Here, the modified boiling number(Bo_m), Weber number(We), and Jacob number (Ja) are given by

$$Bo_m = \frac{qx}{\mu_l h_{fg}} \tag{2.12}$$

$$We = \frac{\rho_l u_d^2 d_{32}}{\sigma} \tag{2.13}$$

$$Ja = \frac{c_p \Delta T}{h_{fg}} \tag{2.14}$$

where q is the heat flux, x is the characteristic length scale, μ_l is the dynamic viscosity of the liquid, h_{fg} is the latent heat of vaporization, ρ_f is the density of the liquid, u_d is the droplet velocity normal to the surface, σ is the surface tension, c_p is the specific heat, and ΔT is the wall superheat. The above heat transfer correlations have made initial contributions to the field of spray cooling. However, more such correlations are needed for predicting the heat transfer rates over surfaces with different physical and chemical properties.

2.4 Critical heat flux

Critical heat flux is a heat transfer limit representing the maximum heat flux that can be removed from the surface with a given set of spray properties and surface geometry. Mechanisms causing CHF is a widely debated topic in the spray-cooling literature, and currently, numerous models are available. Numerous heat transfer investigators on spray

cooling in the literature designed their experiments to document the values of CHF for different spray systems and experimental conditions. Lin [48] developed a closed-loop, multi-nozzle configuration to study the heat transfer characteristics of spray cooling using different liquids. Maximum CHF of 500 W/cm^2 is obtained with water (Volumetric flux, *Q" = 0.025 m/s, Δp = 2.41 bar*) while the fluorocarbon liquids (FC-87/FC-72) showed a peak flux of *90 W/cm^2* (Volumetric flux, *Q" = 0.020 m/s, Δp = 2.41 bar*). Visaria and Mudawar [49], [50] obtained an empirical correlation (eqn. 2.15) to predict CHF using the experimental data acquired by varying various control parameters, including nozzle type, volume flow rate, spray angle, the degree of subcooling, and inclination angles.

$$\frac{q"}{\rho_g h_{fg} Q"} = 2.3\left(\frac{\rho_f}{\rho_g}\right)^{0.3}\left(\frac{\rho_f Q"^2 d_{32}}{\sigma}\right)^{-0.35}\left(1 + 0.0019\frac{\rho_f c_p \Delta T_{sub}}{\rho_g h_{fg}}\right) \qquad (2.15)$$

Where *Q"* is the volumetric flux, *q"* is the applied heat flux, ρ_f is the density of the liquid, ρ_g is the density of the vapor, c_p is the specific heat of the liquid, ΔT_{sub} is the degree of subcooling, σ is the surface tension and h_{fg} is the latent heat of vaporization. Nevertheless, the validity of the above correlation remains equivocal as it fails to include critical properties such as surface roughness.

2.3.1 Effects of surface texturing

Heat transfer mechanisms such as evaporation and bubble nucleation are common to pool boiling and spray cooling. For pool boiling, Honda and Wei [51] summarized two key research findings on the effects of surface roughness.

- Surface roughness of any kind enhances nucleation boiling
- Micro-pin fins most effectively increase CHF by stabilizing the bubble nucleation sites through faster bubble departure rates.

In spray cooling, both the evaporation at the liquid-vapor interface and the bubble nucleation at the solid-liquid interface is equally important. Notably, at high heat fluxes, the contribution of the contact-line evaporation to the overall heat transfer rate is found to be dominant [5], [52].

Section 2 highlighted that the evaporation rate is highest at the contact-line region due to minimal thermal resistance. Liquid-vapor phase change at the microscale contact-line region governs the heat transfer rate at the system scale. For a plain wetting surface, the characteristic length of the transition region is microscopic, ranging from a few hundreds of nanometers to few microns [1]. Thus, a tiny increment in this characteristic length of this microscale region would provide a larger area for evaporation to occur at the system scale. For a given liquid, the macroscopic contact angle (θ_Y) at the liquid-solid contact line is given by Young's equation (Eqn. 3.1).

$$\sigma_s = \sigma_{sl} + \sigma_l \cos\theta_Y \tag{3.1}$$

Wenzel [53] proposed a theoretical relation between the apparent contact angle (θ_a), the macroscopic contact angle (θ_Y), and the roughness factor of the solid surface (r), which is given by

$$\cos\theta_a = r\cos\theta_Y \tag{3.2}$$

Where,

$$r = \frac{Actual\ Surface\ Area}{Geometric\ Area} \tag{3.3}$$

According to Wenzel's theory, for a wetting surface ($\theta_Y < 90°$), the apparent contact angle can be reduced by increasing the surface roughness of the solid surface. Thus, by introducing surface roughness, the contact angle at the liquid-vapor interface reduces,

resulting in an extended transition region by decreasing film thickness, as shown in fig. 2.7.

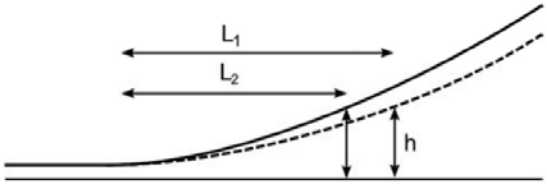

Fig. 2.7 An illustration demonstrating the increase in the wettability (decrease in contact angle) results in the elongation of the transition region; thus, promoting evaporation rate. [1]

Table 2.1 shows a compiled list of operating parameters and experimental results such as maximum CHF, spray cooling efficiency, etc., obtained by various researchers through surface enhancements. Pais et al. [54] showed that high heat transfer rates could be achieved through direct evaporation of the liquid film using ultra-smooth surfaces with micro-/nano-scale roughness. Ultra-smooth surfaces of different roughness were obtained by polishing the surface using emery paper of grit sizes ranging from *0.3 – 22 μm*. For a surface roughness value of *0.3 μm*, the authors reported the highest CHF value of *~1200 W/cm^2* with a water flow rate of *85 ml/min* corresponding to a spray efficiency of *~34%*. The authors reported that bubble nucleation and boiling played a dominant role in heat transfer for surfaces with roughness values greater than *1 μm*. When roughness values are less than *0.5 μm*, ultra-low liquid film thicknesses (*~ 0.1 μm*) can be achieved during the spray-cooling process. The authors observed that very thin liquid films promoted the early departure of the nucleated bubbles from the surface. Faster bubble departure enabled the surface to let go large amounts of heat energy through interfacial solid-liquid heat conduction and liquid film evaporation while bypassing the issue of bubble crowding and interference. However, considering the length scales of the roughness used in this

experiments, contact-line evaporation through enhanced capillary suction could be a primary element for superior heat transfer performance.

Initial studies focused on increasing the thermal performance by experimenting with surfaces enhanced containing millimeter-scale features. Silk et al. [55] conducted experiments with enhanced surfaces containing millimeter-scale straight fins, cubic fins, and pyramids. Results reveal that straight fins show slightly better heat transfer performance in terms of cooling efficiency and CHF (*30%* increments in CHF) compared to flat surfaces, followed by cubic pin fins and pyramid structures. Sodtke and Stephan [52] performed spray cooling experiments with degassed water (flow rate, $Q \sim 270$ *ml/min*) on plain surfaces and surfaces covered with micro-pyramids with different widths ($W = 150, 300,$ *and* $450\ \mu m$) and heights ($H = 75, 150,$ *and* $225\ \mu m$). They also measured the contact line length using high-speed infrared imaging with thermochromic liquid crystals on the backside of the heater. Surfaces with micro-pyramids showed a significant increase in the heat transfer performance as compared to the plain surface. This effect is attributed to the increase in three-phase contact line length due to enhanced capillary suction and re-wetting at the surfaces of the microscale structures.

Table 2.1 Experimental Details of spray cooling parameters collected from various literatures [54], [56], [65]–[69], [57]–[64]**.**

Feature type	Investigator/year	Feature Size (μm)	Nozzle type	Fluid(s)	Liquid flow rate (l/min)	Gas flow rate (l/min)	Droplet SMD (μm)	Droplet velocity (m/s)	Max. CHF (W/cm^2)	Spray Efficiency (%)
Roughness /Grits	Pais et al. (1992)	0.3 to 22	Gas-Assisted	DI Water/Air	0.0167 - 0.083	6 - 24	7 - 28	7 - 50	1200	33.57
	Kang et al. (1998)	0.45 to 4.47	Gas-Assisted	DI Water/Air	0.05 - 0.45	NA	15 - 100	2.8 - 3.4	NA	-
	Ortiz et al. (1999)	NA	Gas-Assisted	DI Water/Air	0.025 - 0.0485	NA	85 - 100	NA	375	22.03
	Galvan et al. (2013)	0.04 - 0.56	Full Cone	R134a	0.17 - 0.50	-	58.2 - 120.8	13.1 - 22.1	190	10.14
Straight /Cubic pin fins	Hsieh & Yao (2006)	160 - 480	Full Cone	Water	0.024 - 0.0892	-	75, 100	31.9	NA	-
	Coursey (2005)	500	Full Cone	PF-5060	0.069 - 0.123	-	NA	NA	131	21.5
	Liu (2011)	100 - 400	Full Cone	Water	0.044 – 0.053	-	107.7 – 112.3	19.7 – 23.9	360	15.77
	Li (2015)	300	Full Cone	R134a	1.02 – 2.15	-	NA	NA	326	36.4
	Zhang et al. (2015)	100 - 700	Full Cone	Water	0.039 – 0.305	-	65 – 122.1	37.2 – 39.9	350	1.45
	Thiagarajan et al. (2014)	0.33	Full Cone	HFE-7100	0.066 – 0.95	-	102 – 460	NA	189.0	6.27
	Zhou et al. (2019)	0.7 – 3	Full Cone	R410a	NA	-	-	NA	330.0	44.77
	Bostanci et al. (2014)	500	Gas-Assisted	Ammonia	96	828	NA	NA	1090	60.20
	de-Souza et al. (2012)	0.54, 0.108	Full Cone	R134a	11.765	-	NA	NA	40.0	69.71
	Chien et al. (2011)	0.23	Full Cone	FC-72	22.5 – 99.1	-	NA	NA	89.0	37.60
	Amon et al. (2005)	120 - 480	Full Cone	HFE-7200	5.53	-	50 - 100	NA	45.0	21.93
	Yang et al. (2013)	260 – 480	Full Cone	Ammonia	16.2	-	32	42	388.0	20.77
	Xie et al. (2014)	0.5 - 3	Full Cone	R134a	8.2	-	172 - 189	18.1 – 24.6	270.7	28.11
	Wang et al. (2016)	10 - 23	Full Cone	Ammonia	0.0272 – 0.0367	-	28.3 – 30.5	34 - 40	350.0	26.57
	Wang et al. (2018)	160	Full Cone	Water	0.08 – 0.35	-	219 – 276	NA	470.9	7.09

Martínez-Galvan et al. [58], [70] investigated the effects of surface roughness, volumetric flow rate, and nozzle type on the spray cooling performance. For a smooth surface, the CHF value remains unchanged for increased flow rates; however, CHF increased with increasing flow rates for a given rough surface (Max. CHF ~ $190\ W/cm^2$). On flat surfaces, the onset of surface nucleation is found to be delayed due to low nucleation site density, and immediate activation of nucleation sites triggers CHF at lower superheats and lower heat fluxes. Zhang and co-workers [71]–[74] have obtained CHF values of ~ $808\ W/cm^2$ at wall superheats of $90\ K$ using water on surfaces with $200\ \mu m$ features. Several studies have documented increases in heat transfer coefficient and CHF by modifying the surface chemistry or roughness using carbon nanotubes [61], graphene layers [75], silicon and copper nano- and micro-structures [76], and microporous diamond coatings [77]. These studies have all demonstrated the significant potential of surface geometry and chemistry in enhancing heat transfer performance.

Empirical evidence [54], [56]–[61] suggests the heat transfer performance of the spray cooling process can be enhanced by tailoring the surface topography. However, the current research findings are not extensive enough to develop a predictive model to understand the reason for heat transfer enhancement. Further, several authors tested surfaces with millimeter protrusions while the others used surfaces with micro-and nano-scale grits. This non-uniformity in the type of surface topographies poses a difficulty in developing a universal heat transfer model for textured surfaces.

The surface roughness enhances CHF and improves the spray cooling performance due to individual/combinatory effects of the following factors – (a) surface area enhancement, (b) reduction in contact angle, and (c) in-plane stretching of the contact-line through

capillary suction. The above factors are simultaneously varied or remain uncontrolled in most of the studies discussed in this section.

2.5 Spray cooling systems

Most of the spray cooling experiments conducted in research labs have a target surface area of less than *2 cm^2*. However, in practical applications, high-power electronic systems are often larger (~ *20 cm^2*). For efficient cooling of large-scale electronic systems, the liquid coolant must be distributed uniformly over a large surface, and the used coolant must be drained efficiently from the system. To ensure uniform liquid distribution, a cooling system with multiple spray nozzles is preferred instead of a single-nozzle system. Pautsch and Shedd [41] performed a parametric study to investigate the influence of spray nozzle parameters such as nozzle-nozzle distance and the number of nozzles. Although different nozzle assemblies showed different behavior regarding heat transfer performance, some of the performance aspects were universal. For instance, multi-nozzle arrays showed increased CHF values. Despite all design considerations, the liquid distribution was found to be non-uniform during the experiments due to spray-spray interactions.

Lin and Ponnappan [78] built a closed, two-phase loop spray system containing 48 nozzles to cool a surface with an area of *19.3 cm^2*. FC-72 and water were used as working fluids in the experiments. Recent results were compared with their previous data obtained for a *2 cm^2* surface area [48]. The authors observed a *30%* and *34%* reduction in the maximum heat transfer coefficient and CHF, respectively, for large-area spray cooling (A = *19.3 cm^2*). The reduction in heat transfer performance is a direct consequence of spray-spray interactions before/after impact. Xie et al. [67] used a closed-loop spray system containing fifty-four nozzles with an in-line array of 9 × 6 to cool a large heated surface

($12.3 \times 15.5\ cm^2$). R134a was used as a working fluid for all the experiments. The authors reported a maximum heat transfer rate of 16 kW with an average surface temperature of $26.5\ °C$ while obtaining heat transfer coefficients up to $2.8 \times 10^4\ W/m^2K$. The authors also observed the local surface temperatures as a strong function of the distance from the nearest drainage outlets, while dependence on the spray-spray interactions was weak.

2.6 Research objectives

Based on the critical observations made from the literature review, the objectives of this thesis are two-fold and described below.

(i) The physical length scale of the spray cooling process varies from nanoscale to mesoscale, indicating surface roughness can play a major role in enhancing the thermal performance. A thin liquid film is prone to dry-out at high heat fluxes, due to long-wave instabilities. Surface enhancements shall potentially play a role in stabilizing the liquid film by promoting in-plane capillary flows towards incipient dry spots, and, therefore, to delay the onset of CHF. On hindsight, empirical evidence from pool boiling data [79] shows a CHF enhancement maximum when the micropillar diameter and spacing is of the order of $10\ \mu m$. Since the underlying heat transfer mechanisms are the same for both spray cooling and pool boiling, surfaces with micropillars must then show maximum performance only in a certain parametric range in spray cooling. However, in the currently available literature, no systematic study is available to evidently show that such a length scale exists.

(ii) Recent research [5] shows that heat transfer from the surface due to an evaporating meniscus primarily depends on the liquid-vapor interfacial area and not the liquid-solid contact area. Also, interfacial evaporative phenomena at the nano-/micro-scale can influence heat transfer parameters to a large extent. Hence, an in-situ visualization of the

solid/liquid/vapor interface is necessary to identify possible relations between the contact-line parameters like wetted area fraction, and contact-line perimeter, and the heat transfer characteristics like CHF, heat transfer coefficient, and efficiency. Contact-line curves plotted between integral interfacial quantities (i.e., the wetted-area fraction and contact-line perimeter) and the wall superheat or heat flux would demonstrate the role of surface characteristics on global heat transfer characteristics.

Chapter 3

Materials and methods

3.1 Introduction

The previous chapter discusses the process of spray cooling and its advantages over the other cooling techniques. Spray cooling mechanisms (both in the single-phase and two-phase regimes) were discussed briefly. Until now, there has been no consensus among the research community about the mechanisms causing CHF. Nevertheless, CHF enhancements can be obtained through surface texturing, flow control, and altering the spray characteristics. The primary objective of this research is to investigate the role of surface roughness on spray cooling performance. The following sections discuss the heater surface (referred to as “sample” here) design and the steps involved in sample fabrication at the Minnesota Nano Center. In addition, details about spray characterization, spray cooling test rig, the experimental procedure for performing the heat transfer experiments are enumerated.

3.2 Sample Design and Fabrication

3.2.1 Parametric range

Roughness geometry and length scales were chosen such that the following expectations are met:

(a) ensure maximum cooling performance through contact-line pinning and promoting intense evaporation near the contact-line zone.

(b) maximize the in-plane surface rewetting flow through enhanced capillary action, decreased contact angle, and reduced hydraulic drag.

Plawsky et al. [27] reviewed the importance of the disjoining pressure [28] in enhancing flow towards the contact-line region. The intermediate region between the bulk film ($> 100\ \mu m$) and the adsorbed liquid layer ($< 10\ nm$) [29], of thickness $\sim 100\ nm$, exhibits the highest evaporative mass flux as well as the lowest thermal resistance. Morris [30], [31] pointed out the importance of the length of the stretched meniscus region near the contact-line region, where the overall conduction resistance is low. This in-plane stretching action of the menisci favors a low contact angle. In addition, at elevated temperatures, most of the liquids tend to decrease their viscosity with an increase in temperature, which further helps the capillary forces to spread out the liquid film []. In the context of rewetting of hot/dry spots on a heater surface in pool boiling, Dhillon et al. [79] pointed out that the hydraulic drag experienced by the capillary forces were minimal when spacing/height is one and observed a CHF maximum at this aspect ratio for arrays of pin fins with a diameter of $10\ \mu m$. Keeping the above criteria and expectations in mind, we chose to increase the roughness by populating the surfaces with a structured array of pin fins of square cross-section.

We systematically decrease the roughness scales from $50\ \mu m$ to $0.8\ \mu m$ while keeping the porosity constant ($\phi = 0.75$). Additionally, we expect the height of these micropillars to influence wicking characteristics and the extent to which the contact line can be stretched through in-plane capillary suction. Hence, for all micropillar configurations specified by

diameter D and spacing P (in this study, P = D, see fig. 3.1), the pillar height is chosen to be around *80 nm* to tens of micrometers.

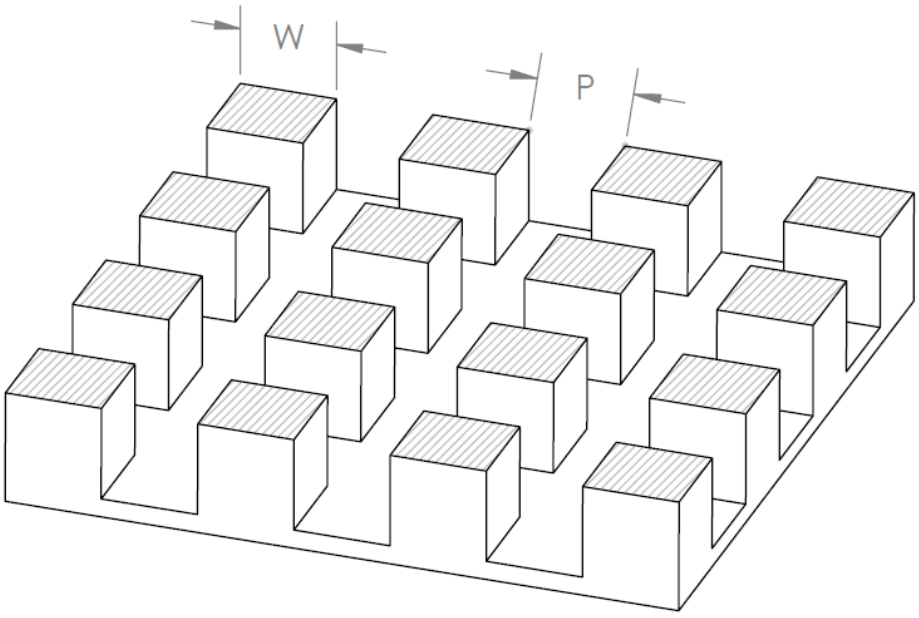

Fig. 3.1 Zoomed view of the schematic of a micropillar array

The effect of pillar spacing on thermal performance is yet to be studied for spray cooling. Surfaces with pillar diameters *5 μm* and *10 μm* were tested to study this effect. Keeping the pillar height and diameter constant, the porosity is varied by altering the spacing between the pillars. A total of 36 diameter/height and 8 pitch/height combinations were tested, as shown in the test matrix in Table 1.

Table 1. List of pillar-array surfaces tested

Pillar diameter, D (μm)	Pitch, P (μm)	Height, H (μm)
Height Variation		
50	50	0.08, 0.14, 0.46, 5.13, 12.37, 24.83, 35.71, 57.73
20	20	0.10, 0.22, 0.54, 4.26, 8.23, 19.62, 47.00
10	10	0.43, 0.81, 5.26, 8.28, 23.40, 47.78
5	5	0.18, 0.85, 2.70, 4.60, 12.05, 19.88
2	2	0.22, 1.1, 1.6, 2.6, 3.95, 6.7
0.8	0.8	0.48, 0.61, 1.2
Spacing Variation		
5	1, 2.5, 5, 7.5, 10	9.06, 8.31, 8.66, 9.06
10	2, 5, 10, 15, 20	8.58, 9.27, 8.56, 8.58

3.2.2 Sample fabrication

Figure 3.2 shows the fabrication process flow-chart used to create the micropillar geometries with height-to-spacing ratio less than or equal to one.

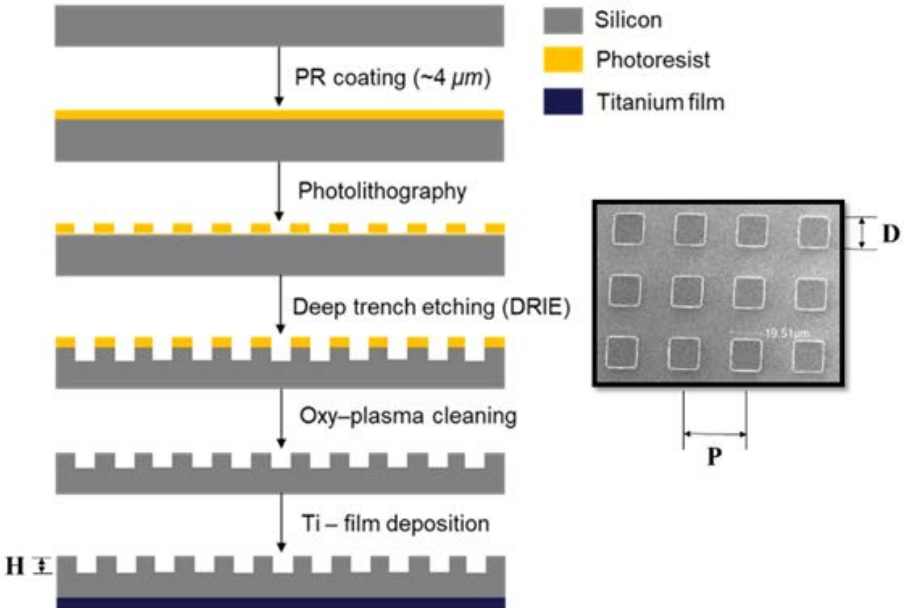

Fig. 3.2 Process flowchart detailing the fabrication sequence used to create low-aspect-ratio pillar arrays (left). An SEM image (right) featuring the surface topography of the 20-μm micropillar configuration.

Before starting the fabrication process, the double-side polished silicon wafer (*100 mm* diameter, *525 μm* thick) was cleaned using the Piranha (H_2SO_4/H_2O_2) solution. The cleaned wafer was then heated to *150 °C* for 3 minutes and exposed to HMDS vapor for 3 minutes to promote adhesion between the silicon wafer and photoresist layer. A standard photolithography procedure was followed to create feature sizes *2 μm - 50 μm* using a positive photoresist (MicroChemicals GmbH AZ 1512) using a mask aligner (Karl Suss). However, for fabricating *0.8 μm* samples, an advanced lithography procedure using Canon wafer stepper was followed (Photoresist: Dow ULTRA-i 123) to obtain high-resolution microlithography. Details of the standard and advanced photolithography process are provided in the following paragraphs.

- *Standard lithography* - The pre-processed wafer was spin-coated with a positive photoresist (AZ 1512) at *3000 rpm* for 30 seconds and pre-baked at *100°C* for a minute. The pre-baked wafer is then exposed to UV light to transfer the micropillar array pattern from the chrome mask to the photosensitive layer (i.e., the spin-coated photoresist layer) and post-baked at *95°C* for a minute. The post-baked wafer was then developed using an aqueous solution with the AZ 340 developer (1:5 H_2O by volume).

- *Advanced Photolithography using Canon Stepper* - The positive photoresist (AZ 1512) and related photolithography procedure mentioned in the previous paragraph works very well for features sizes down to *2 μm.* However, for features sizes smaller than *2 μm, i.e.,* for *0.8 μm* samples, an advanced photoresist (ULTRA-i 123) was used to obtain high-resolution microlithography. The spin-coated wafer is soft-baked at 90°C for 90 seconds, and a Canon Stepper tool (printing wavelength ~ 365 nm) was used to expose the soft-baked photoresist. After exposure, the wafer was baked at *120 °C* for 120 seconds. Subsequently, a CD-26 developer was used to develop the photoresist. The rest of the fabrication process is the same as mentioned in the previous paragraph.

After the lithography, a deep reactive ion etching process was used to etch the wafer to desired heights. The remaining photoresist was then removed using acetone and then spin-rinse-dried using deionized water and nitrogen.

Figure 3.3 shows the fabrication process flowchart used to create the micropillar geometries with a height-to-spacing ratio greater than one. A thin layer of Alumina was deposited on top of the piranha-cleaned wafer using the Atomic-layer deposition technique.

A standard photolithography procedure (Photoresist - AZ 1512) mentioned above was administered to create the desired feature size. Next, the alumina layer was selectively etched using a reactive ion etcher (RIE) combination of C_4F_8, CHF_3, and Ar gases. The leftover photoresist layer was removed using oxy-plasma cleaning. The resultant alumina hard mask provides a higher selectivity ratio while being etched for long durations. The uncovered silicon regions were etched in a deep-trench etcher (DRIE) using a high-aspect-ratio plasma etching process (also known as the Bosch process). The Bosch process is a two-step process – (i) SF_6 plasma cycle etches silicon, and (ii) the C_4F_8 plasma creates a protective layer to prevent the trench sidewalls from being etched. After silicon etching, the hard alumina mask is removed using a Buffered Oxide (BOE) solution.

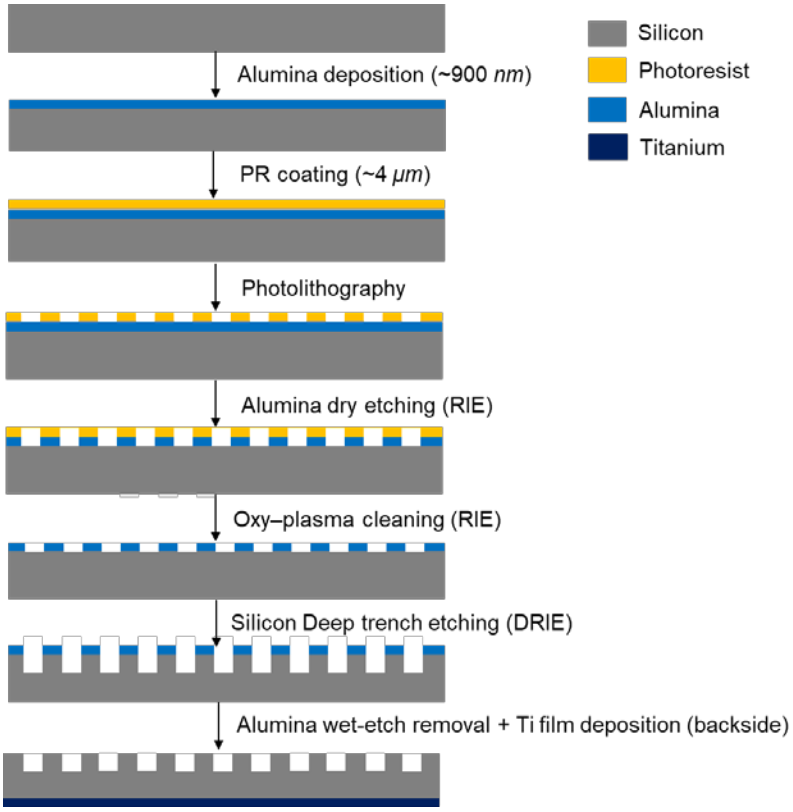

Fig. 3.3 Process flowchart detailing the fabrication sequence used to create high-aspect-ratio pillar arrays

An e-beam deposition process was used to deposit titanium film (R ~ 55 Ω) of thickness *~280 nm* on the backside of the wafer before dicing it into a rectangular chip (*13 × 10 mm*^{2}). Pillar heights and widths were measured using a scanning electron microscope (see fig. 3.2). The samples were rinsed using standard solvents such as acetone, isopropyl alcohol, and deionized water at least three times, followed by a plasma-cleaned in an Oxygen atmosphere for 3 minutes in a reactive ion etcher (RIE) before proceeding to the post-processing step.

3.2.2 Post-processing and assembly

The pre-cleaned chip was fixed on top of a glass slide (*3" × 2"*) with a *5 × 5 mm*^{2} square hole at its center using silver epoxy (Chemtronics® CW2460) and copper tapes. Through the square hole, three calibrated T-type thermocouples (*uncertainty ~ 0.03 K*) were attached upon the backside of the silicon chip using a thermal epoxy resin (EPO-TEK® T905BN-3). A 6-mm thick block made of Sylgard™ 184 Silicone elastomer (*k ~ 0.27 W/m.K*) is attached using low thermal conductivity Kapton tapes (*k ~ 0.46 W/m.K*) to prevent natural convection heat loss from the backside. A pair of shielded wires were soldered to the copper tapes, and this entire assembly was fixed on top of an ABS plastic stage using Kapton™ tapes (see Figure 3.4). The resultant resistance of the heater assembly was found to be less than *~1%* of the titanium film resistance. The shielded wires were then connected to a programmable power supply (Keysight N5771A). To measure temperatures, the thermocouples were connected to a differential multiplexer module (Keithley 7702 40-channel) via a reference junction ice-bath. The 7702 module is then latched into a data acquisition system (Keithley Model 2750 Ethernet Multimeter).

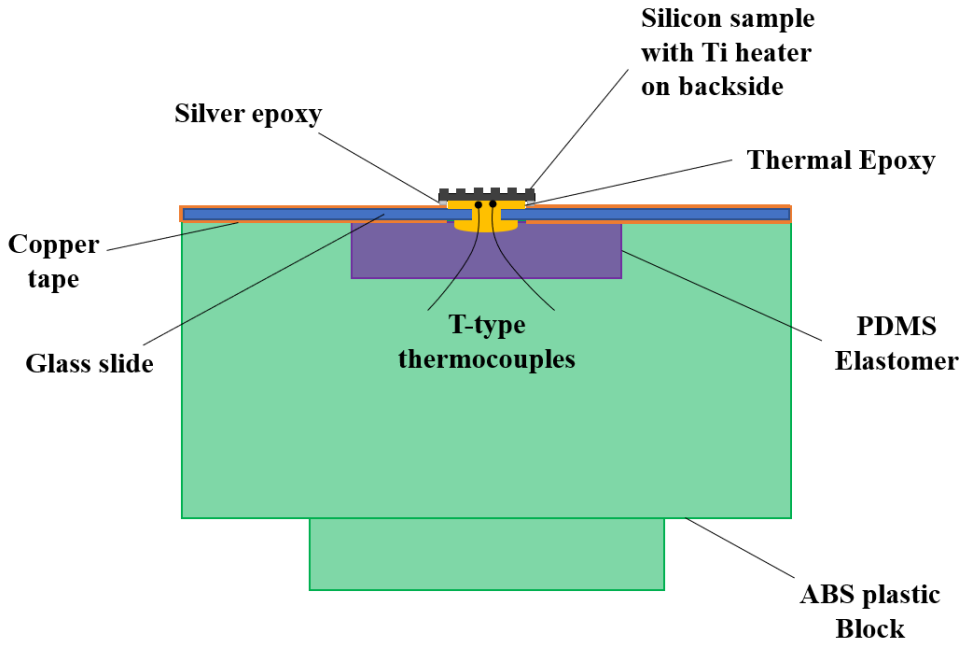

Fig. 3.4 Schematic of the testbed assembly

3.3 Experimental Methods

3.3.1 Spray characterization

The droplet distribution impinging on the test surface was measured independently in a separate facility, using a shadowgraphy technique. A Canon T2i digital camera was connected to a long working distance microscope (Infinity USA Model K2 Distamax^{TM}) and operated at 2.5 frames per second, with a shutter speed of *1/15 s*. Illumination was provided by a pulsed laser operating at *15 flashes/second* (Beamtech® Vlite 200), delivering *200 mJ/pulse*. The magnification achieved was 0.83 μm/pixel, which allowed for the identification of droplets as small as *3 μm* in diameter; however, a cutoff of *6 μm* was imposed, with droplets smaller than this value ignored for data reduction. At least 1000 images were taken for each location and yielded more than 20,000 droplets, which were enough to assure statistical convergence of the distribution and an uncertainty in d_{32} less than *1 μm* (refer to fig. 3.5).

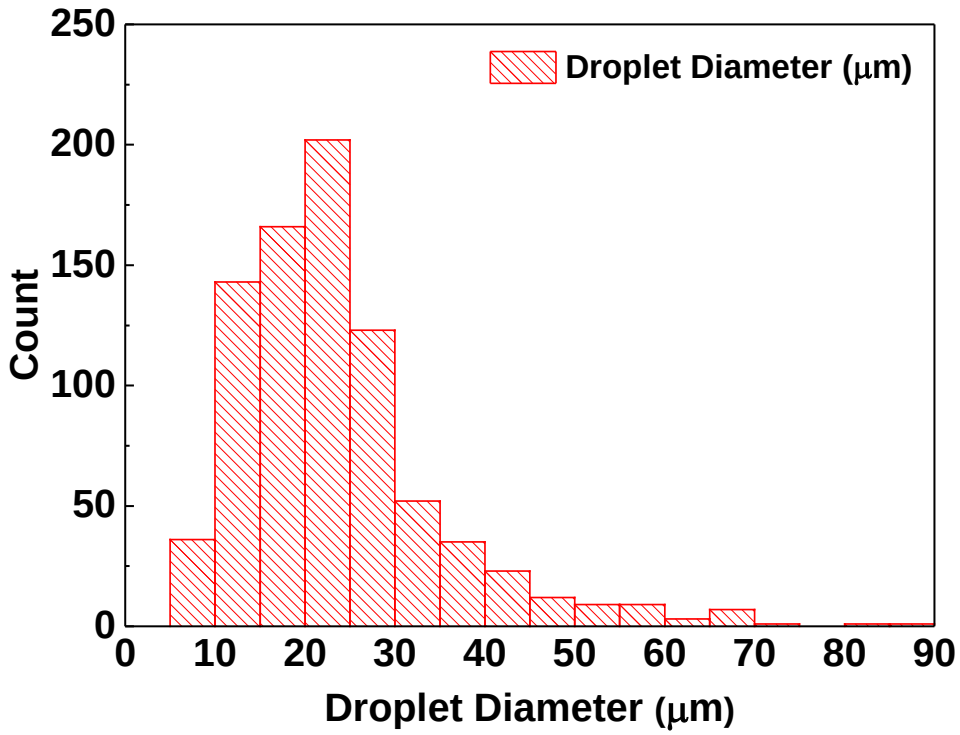

Fig. 3.5 Histogram showing the droplet diameter distribution for the liquid spray generated using the counterflow nozzle
($\dot{Q}_w = 30\ ml/min$; $\dot{Q}_a = 13.7\ l/min$; $P_a = 3\ bar$)

The surface roughness variation experiments were conducted with a *30 ml/min* water flow rate and a *13.7 l/min* air flow rate supplied at *3 bar* pressure. For this flow setting, the mean droplet diameter of the atomized spray was measured to be around *~32 μm*, with most of the droplet sizes ranging from *10 – 45 μm*.

3.3.2 Thermocouple calibration

A Standard Platinum Resistance Thermometer (SPRT, Rosemount 162CE) was initially calibrated to an uncertainty of *5 mK* with the fixed point on the ITS-90 temperature scale (the triple-point of water, *273.16 K*) as reference. The hydration/dehydration temperature of Sodium sulfate decahydrate (*305.524 K*) was chosen to be the second reference temperature. Thermocouples were calibrated using the calibrated SPRT as a reference in a precision isothermal bath containing silicone oil and yielded an uncertainty

of *0.03 K*. More details on the thermocouple and SPRT calibration is provided in Appendix A.

3.3.3 Spray cooling rig

A schematic of the spray cooling setup is shown in fig. 3.6. A magnetically driven precision-geared pump (Micropump L21834) delivers water at *20 °C* to a counterflow nozzle. The counterflow nozzle is an internal mixing nozzle recently developed at the University of Minnesota [33], [34] . Its chief feature is its ability to produce fine droplets *~20 μm* at relatively low air supply pressures. The spray from the nozzle impinges on the test surface, which is located within a test chamber maintained at atmospheric pressure. Most of the experiments were performed while operating the counterflow nozzle at a *30 ml/min* water flow rate and an airflow rate of *13.7 standard liters per minute (slpm)* at a nozzle-to-surface distance of *40 mm*. The heat transfer experiments were performed by continuously increasing power input in steps of *10 W*. For each power setting, once steady-state conditions have reached a set of 50 temperature readings was acquired over *240 s*. The critical heat flux was assigned to the heat flux value characterized by a sudden, significant increase in temperature or chip failure.

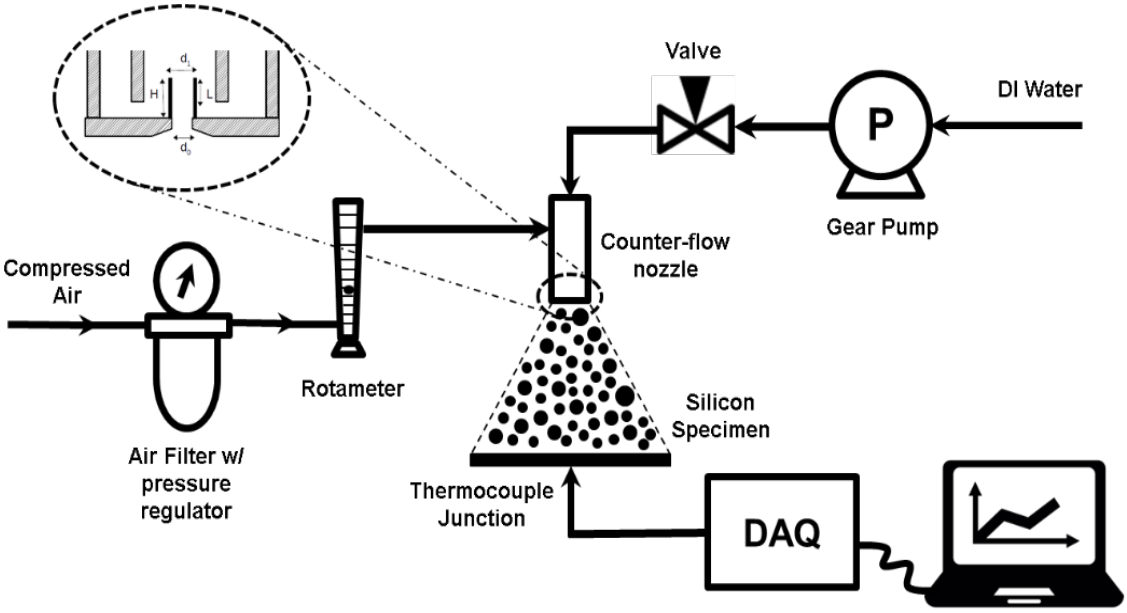

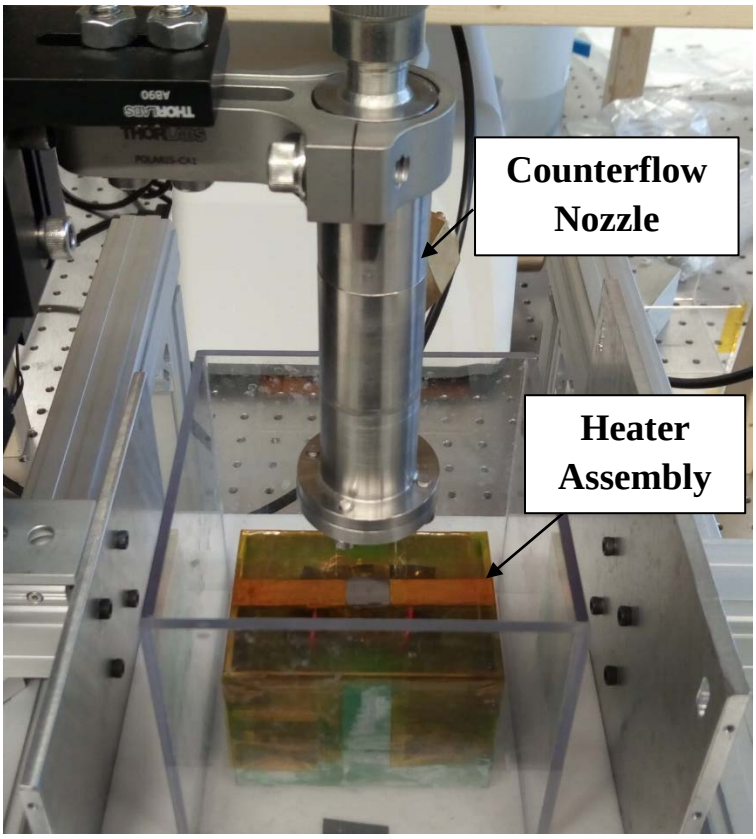

Fig. 3.6 Schematic of the spray cooling test rig (top) feature the counterflow nozzle and the heater assembly (bottom).

3.3.4 Experimental procedure

The liquid spray is started before applying the power to the chip. The spray-to-surface distance is accurately set using a vertical micrometer translation stage with an accuracy of *0.1 mm*. Two horizontal translation stages were used to align the spray with respect to the middle center of the chip surface (accuracy ~ *0.5 mm*). In the single-phase regime, the input power was incremented by *30 W*. Upon attaining saturation temperature, *10 W* increments were done to precisely capture the non-linear trends in the two-phase regime. For each power setting, a set of thirty temperature samples were acquired from each thermocouple over two hundred seconds after reaching a steady state. Steady state is assumed when the standard deviation in temperature is within ~ *0.15°C*. Critical heat flux (CHF) was assigned to the heat flux value at which the surface temperature spikes up drastically; often, marked by the sample substrate glowing red-hot (as seen in Fig. 3.7) followed by structural damage of the substrate. To ensure repeatability, spray cooling experiments were conducted using two identical samples for a given micropillar configuration.

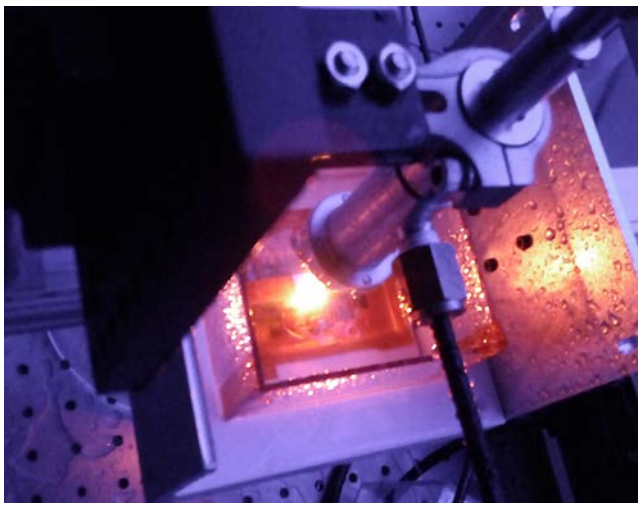

Fig. 3.7 Photograph taken at CHF showing the sample glowing red-hot due to drastic increase in the surface temperature.

3.3.5 Surface temperature estimation

Assuming 1-D heat conduction across the thin silicon chip, the average temperature (T_s) at the surface was found by estimating the temperature drop across the thickness (t_{chip}) of the test chip with thermal conductivity (k) using the following equation.

$$T_s = T_m - \frac{Q_{net}.t_{chip}}{k.A_{chip}} \quad (1)$$

where T_m is the temperature measured at the bottom side of the chip, A_{chip} is the cross-sectional area of the chip (*13 mm* × *10 mm*), and Q_{net} is the power applied to the chip.

3.3.6 Measurement Uncertainty

A data acquisition system was used to record the induced emf (in volts) generated by the thermocouples. In the range of interest, this device has a resolution of *0.1 °C*. T-type thermocouples are calibrated against a standard platinum resistance thermometer, and the temperature uncertainty is found to be *0.03 °C*. Reaching steady state, the temperature fluctuations in the thermocouples were within *0.15 °C*.

The electric power supply has a programming accuracy of *0.1%* and a measurement accuracy of *0.1%*. The uncertainty of the chip surface area is about *0.02 mm*^{2}. The uncertainty in heat flux measurement is around *0.02 W* at *225 W/cm*^{2} which is the smallest CHF data obtained in the present set of experiments. In this case, the uncertainty in temperature measurements is estimated within *0.15 °C*. The highest CHF recorded was around *484 W/cm*^{2} at *30 ml/min* water flow rate with an estimated measurement uncertainty of *0.16 ºC*. The effect of the temperature gradient across the thermocouple beads embedded in the chip is not considered in the uncertainty analysis. The uncertainty of DI water temperature stored in the reservoir tank was estimated within *0.2 °C*. The gear pump drive

along with the pump head was calibrated for DI water. In the operating range, the uncertainty of the flow rate is less than 2% of the reading.

Chapter 4

Effect of pillar geometry

4.1 Introduction

The literature survey discussed in Chapter 2 reveals that a certain amount of work has been conducted to understand the role of surface roughness on the spray cooling thermal performance. However, the absence of a systematic study calls for an in-depth experimental investigation of the roughness parameters. To examine this aspect, heat transfer experiments were performed using various surfaces with micropillar arrays of varying pillar diameter and pillar height while keeping the porosity constant ($\phi = 0.75$). For all results discussed in this section, the spray nozzle was operated at a *30 ml/min* liquid flow rate and an ALR of 0.57 at a nozzle-to-surface height of *40 mm*. CHF values and other performance parameters were enumerated. Moreover, the possible reason for the superior performance of the microtextured surfaces is discussed.

4.2 Experimental results

4.2.1 Droplet size distribution

High-speed images obtained using the shadowgraphy technique were processed using ImageJ – an image-processing software that identifies droplets converts pixel area into droplet diameter using known magnification. Images were taken along the spray axis and at radial locations of *3, 5, and 7 mm*. For the set of thermal experiments discussed in

this chapter, the water flow rate is set to *30 ml/min* with an Air-Liquid Ratio (ALR) of 0.57 (mass basis). The Sauter Mean Diameter d_{32} is measured close to the centerline is *~32 μm*.

Figure 4.1 shows the cumulative volume fraction corresponding to this droplet distribution. This figure shows that *50%* of the droplets are under *32 μm*, and *90%* are under *84 μm*. Figure 4.2 shows the radial distribution of the Sauter Mean Diameter and demonstrates that the entire test surface receives droplets of size in the range *22 – 42 μm*. Velocities were not measured but are estimated to be less than *2 m/s*. Assuming a much larger velocity of *10 m/s* leads to upper bound estimates of Weber number that are no greater than 60, droplet Reynolds numbers less than 350, and values of the dimensional quantity proposed by Negeed et al. [37], [80], K_d less than 40, which is sufficiently low to prevent droplet bouncing and promote adhesion and spreading.

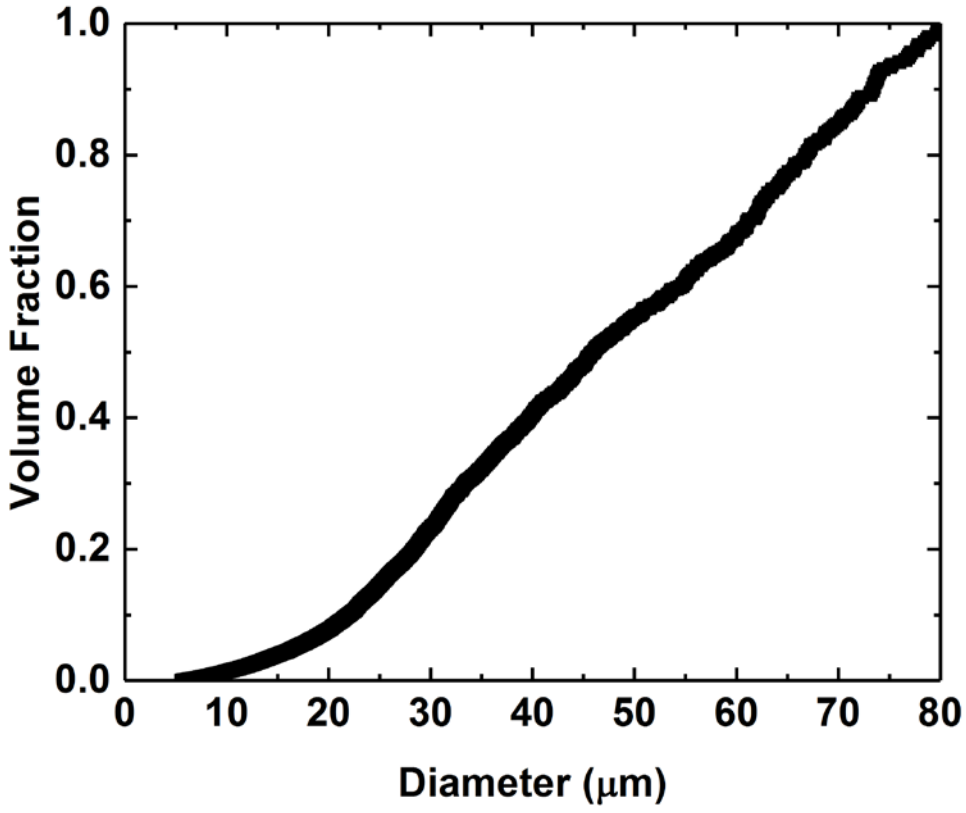

Fig. 4.1 Cumulative volume fraction for the liquid spray corresponding to a water flow rate of *30 ml/min* and *ALR = 0.57*

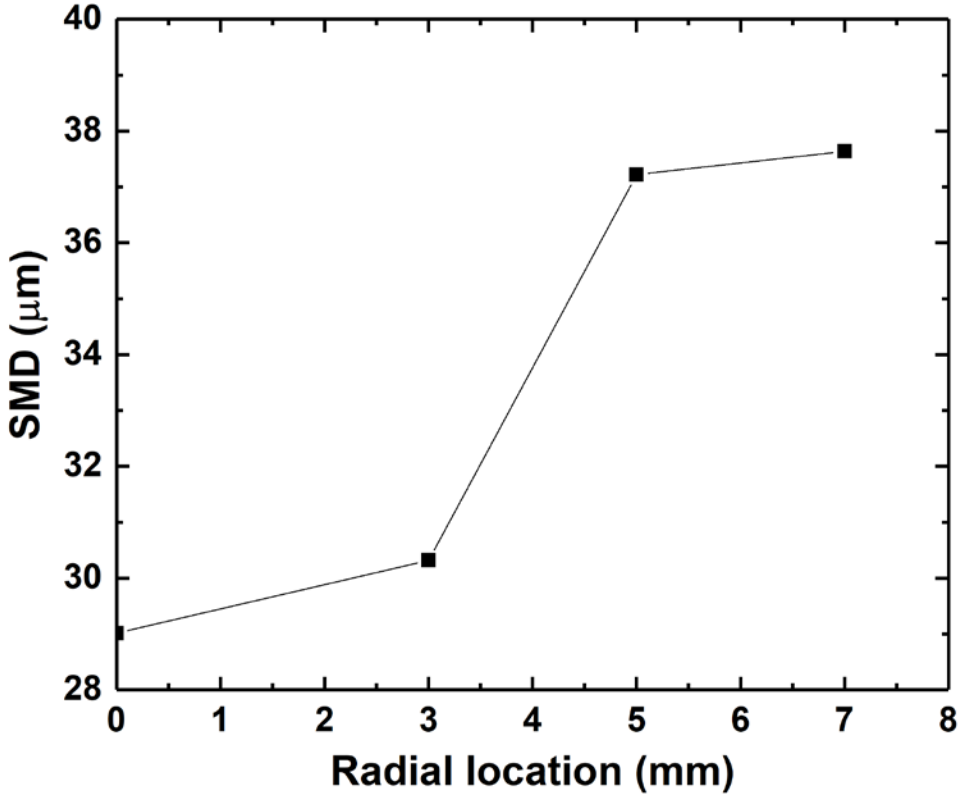

Fig. 4.2 Variation of Sauter Mean Diameter (SMD) across the radial direction of the liquid spray. This data corresponds to a water flow rate of *30 ml/min* and *ALR = 0.5*

4.2.2 Spray Cooling Curves

Figures 4.3 – 4.8 show cooling curves for the plain surface and the various microtextured surfaces tested. These cooling curves clearly show the single-phase regime and the onset of a regime in which phase change phenomena are dominant, as evinced by the sharp change in the slope of the curve. Heat transfer curves corresponding to microtextured surfaces also show a noticeable change in the slope of the curve at surface temperatures less than the saturation temperature, i.e., 100 °C. This phenomenon was repeatable in the experiments and probing into the literature indicates that other investigators observed similar behavior when air-assist nozzles were used [15]. Increasing or decreasing the applied power during the experiments did not introduce any observable hysteresis in the measured temperatures for a given sample. The values of Critical Heat

Flux for each of these geometries were found to be repeatable to within ± 6%. Differences of up to *10 K* were observed across samples for the temperature at which the CHF occurred. This discrepancy might be due to minor differences in thermocouple location along with the spatial variations in temperature which are not measured.

The flat silicon surface displays a CHF of *238 W/cm*^{2}, while surfaces covered with *50-μm* pillars show a CHF of *407 W/cm*^{2}. A continuous increase in the CHF value is observed as the pillar diameter is decreased, reaching a value of *484 W/cm*^{2} for the length scales of *5 μm* investigated. Below *5 μm*, i.e., for surfaces with *2 μm* pillar arrays, the CHF values were depleting ($q"_{CHF}$ ~ *323 W/cm*^{2}). Surfaces with *0.8 μm* pillar arrays recorded the lowest value of CHF ($q"_{CHF}$ ~ *185 W/cm*^{2}) which is lower than the flat surface CHF.

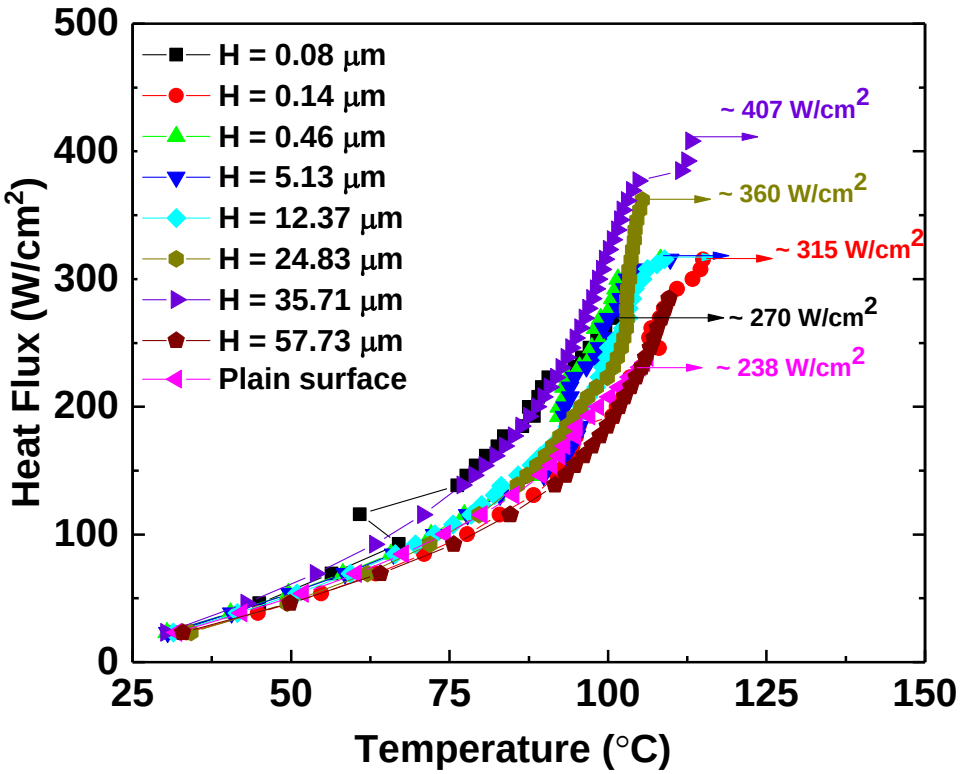

Fig. 4.3 Spray cooling curves corresponding to surfaces with pillar diameter of *50 μm*, pillar spacing of *50 μm* and various heights as shown in the legend.

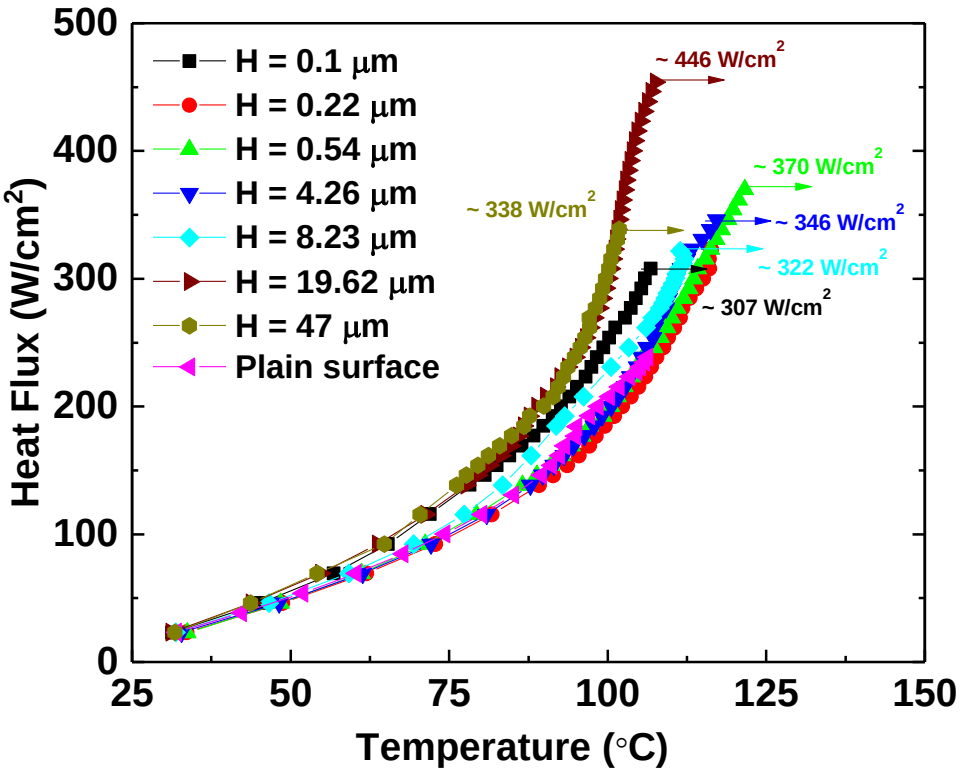

Fig. 4.4 Spray cooling curves corresponding to surfaces with pillar diameter of *20 μm*, pillar spacing of *20 μm* and various heights as shown in the legend.

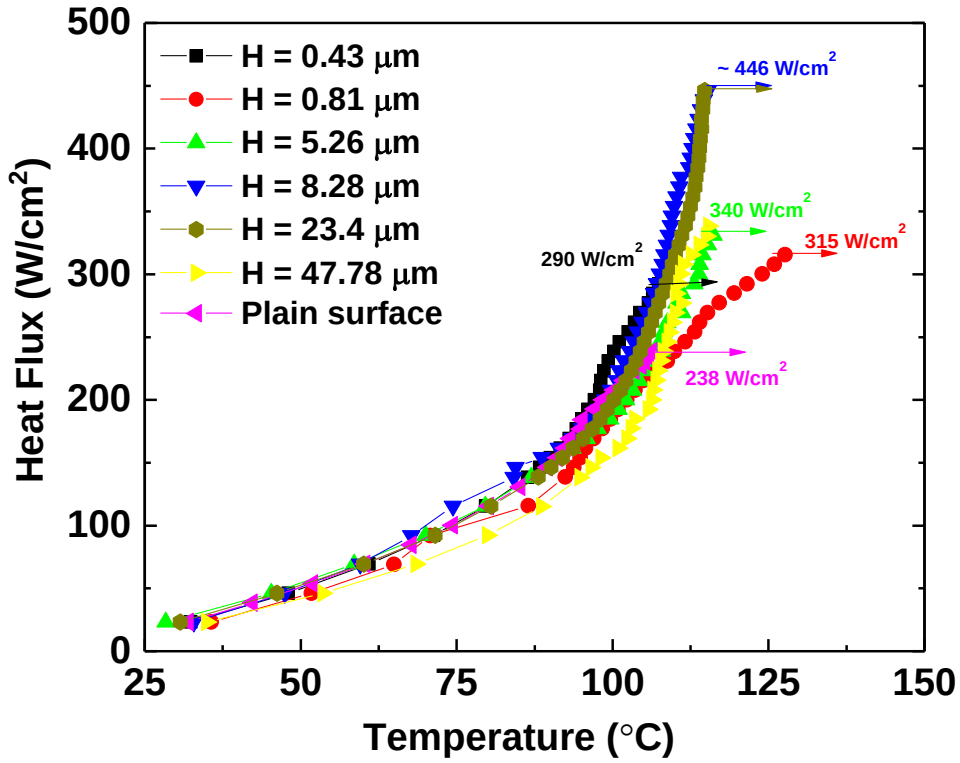

Fig. 4.5 Spray cooling curves corresponding to surfaces with pillar diameter of *10 μm*, pillar spacing of *10 μm* and various heights as shown in the legend.

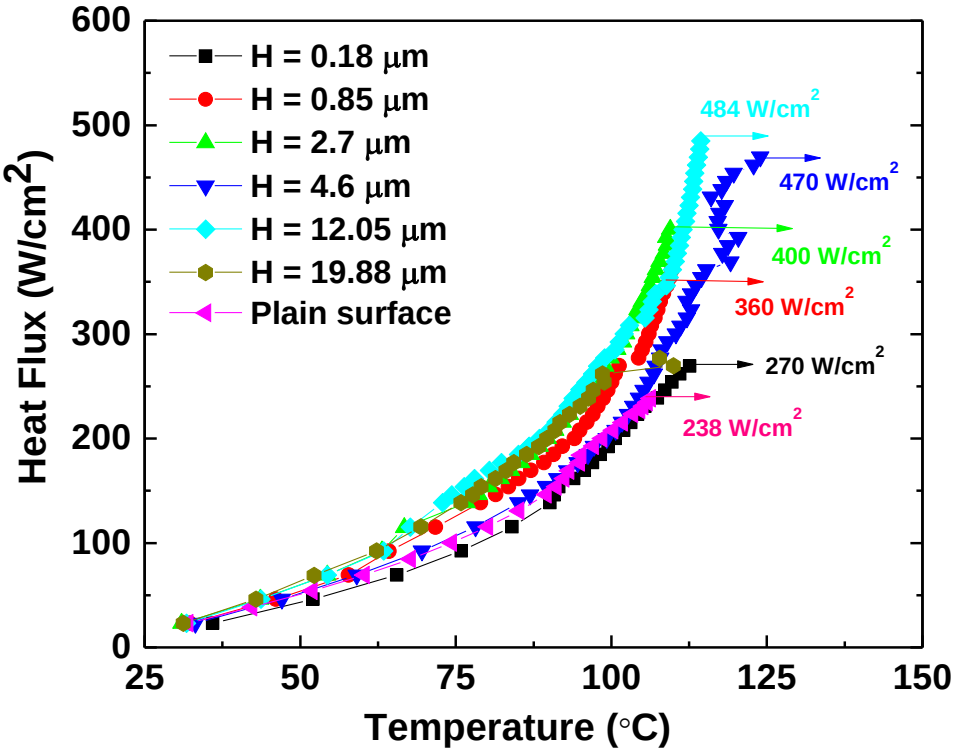

Fig. 4.6 Spray cooling curves corresponding to surfaces with pillar diameter of *5 μm*, pillar spacing of *5 μm* and various heights as shown in the legend.

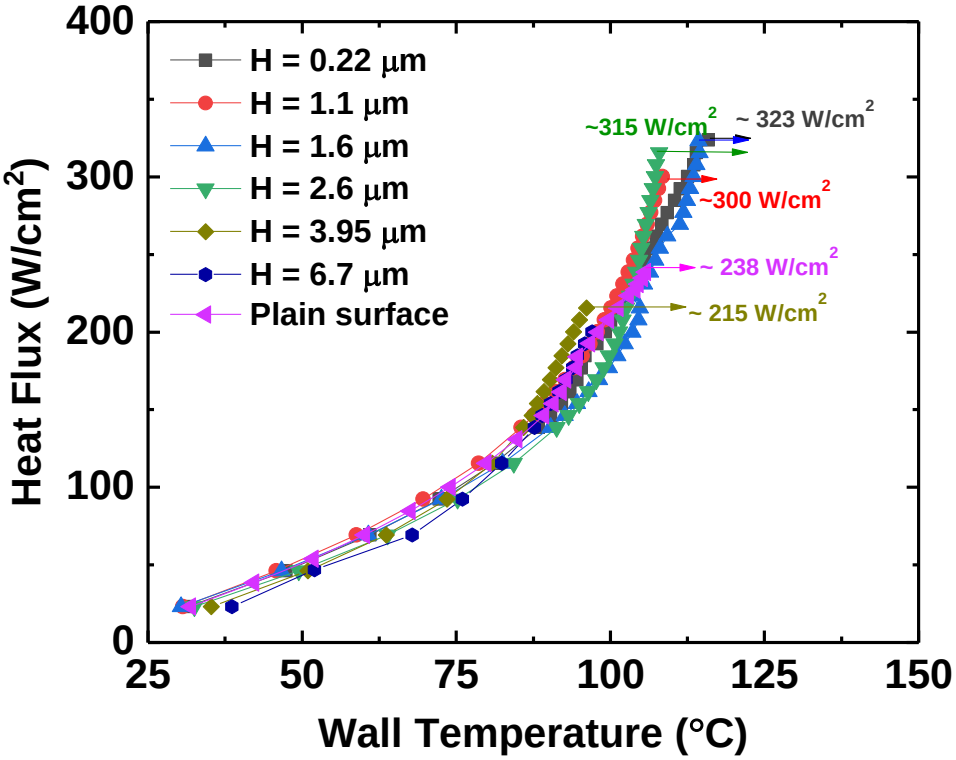

Fig. 4.7 Spray cooling curves corresponding to surfaces with pillar diameter of *2 μm*, pillar spacing of *2 μm* and various heights as shown in the legend.

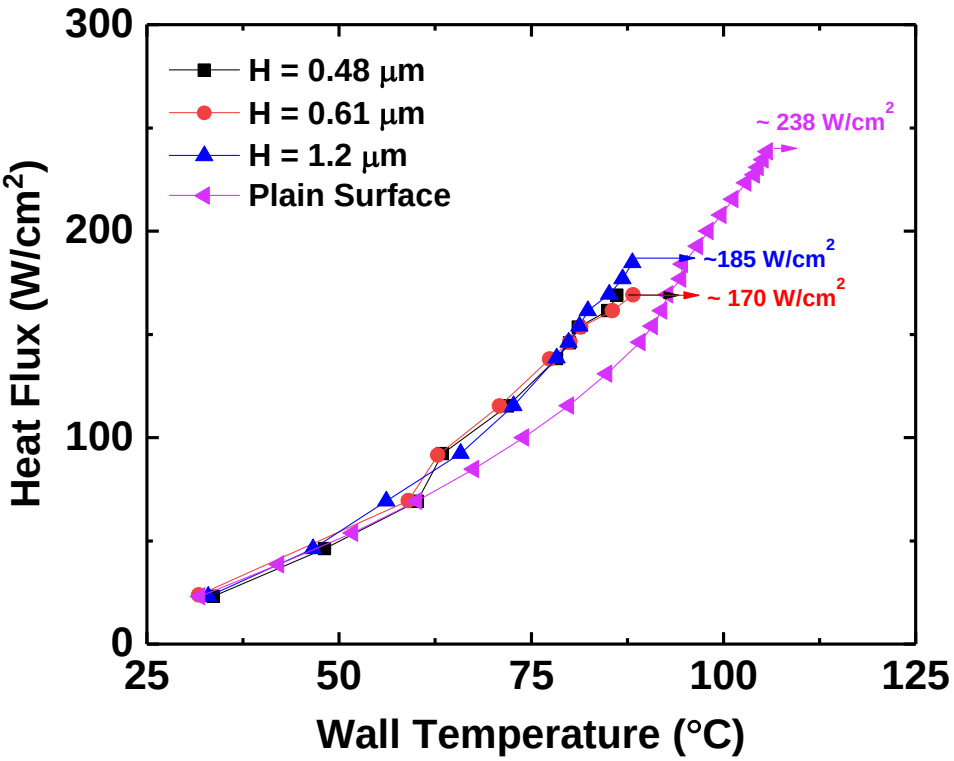

Fig. 4.8 Spray cooling curves corresponding to surfaces with pillar diameter of *0.8 μm*, pillar spacing of *0.8 μm* and various heights as shown in the legend.

4.2.3 Effect of pillar density

This section discusses the effects of shrinking the pillar size and spacing from *50 μm* to *0.8 μm* [81]. These results are in accordance with the conjecture of Hsieh and Yao [19] that an optimum pore-scale should exist whose value is determined by the competing effects of viscous drag on thin-film flow and the surface area enhancement. Highest CHFs were observed for surfaces with optimum length scale of *5 – 10 μm*. We find that the spray cooling performance increased as the density of pillars per unit area increases due to a reduction in pillar diameter, i.e., the *5-μm* pillar configuration shows better performance than the *50-μm* pillar configuration. Multiple factors contribute to this continuous increase in CHF. First, the effective surface area over which heat transfer occurs increases as the pillar diameter is reduced, with enhancement ratios listed in Table 1. The second reason, related to the first, is the increased contact line length as diameter decreases, roughly as the

inverse square of the pillar diameter for a fixed porosity. Lastly, reducing the pore-scale increases surface tension-driven capillary suction, promoting wicking flow through the micropillar array and delaying dry out.

Decreasing the pillar diameter to *2 μm* and *0.8 μm* showed poor heat transfer performance as compared to the *5-μm* samples. The performance parameters monotonically decreased when the pillar diameter was reduced from *5 μm* to *0.8 μm*. To gain deeper insight into this non-monotonic CHF trend, we present a plot featuring area-normalized CHF versus the H/P ratio, i.e., pillar height-to-spacing ratio (see fig. 4.11). The area-normalized CHF was calculated by dividing the applied power by the total surface area, including the pillar surface areas. Surfaces with *0.8 μm* pillar arrays recorded the lowest CHF values (less than plain surface's CHF). From figs. 4.9 and 4.10, there exists an optimum porosity and diameter for which the CHF and associated heat transfer performance values are maximum. In this case, some of the maximum performance values were obtained for pillar arrays with a diameter of *5 – 10 μm*.

4.2.4 Effect of pillar height

To understand the relative contribution of surface area enhancement, contact line length, and near-surface wicking flow, experiments were conducted with multiple heights for each micropillar diameter array. Figure 6 displays CHF data for all 36 configurations tested against the pillar height H. For each pillar diameter, the behavior of CHF with height follows a similar trend. At low height values, the CHF is low, increasing to a maximum value at a certain height before a sharp reduction. The height at which a particular micropillar configuration exhibits a maximum value of CHF is diameter-dependent, i.e., *50-μm* pillar configuration has a maximum CHF at *$H \sim 35\ \mu m$*.

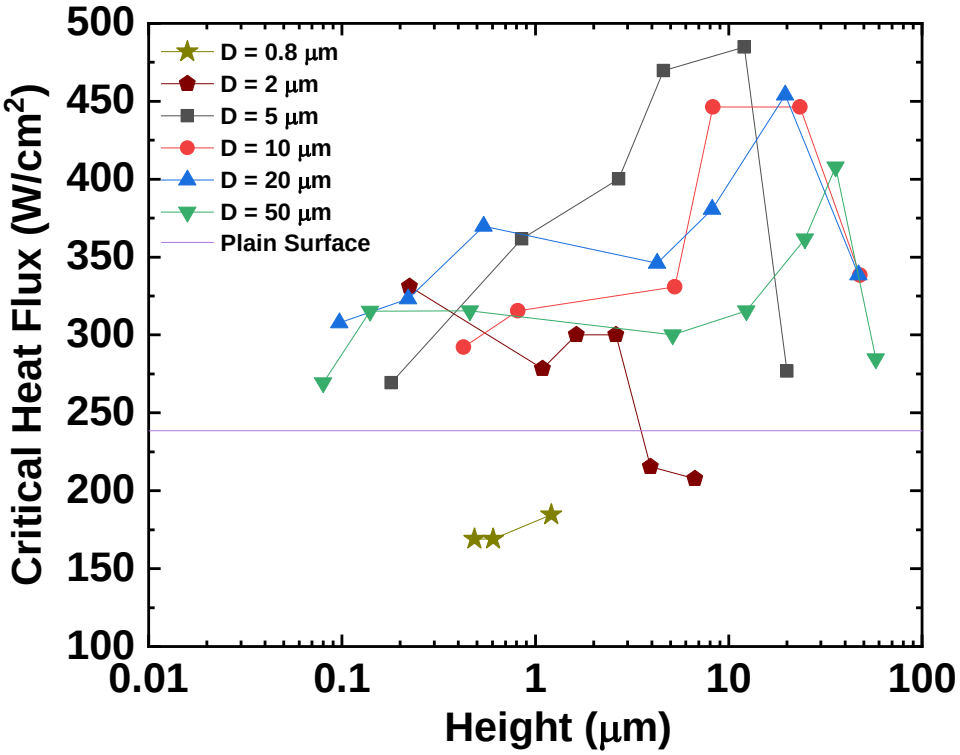

Fig. 4.9 CHF curves obtained for various pillared-array surfaces. The purple line corresponds to the CHF of the plain surface (q''_{CHF} = *238 W/cm²*). Note that the some of the maximum CHFs are recorded for surfaces with *5 μm* pillar diameter.

In contrast, the *5-μm* pillar configuration reaches a maximum value at $H \sim 12\ \mu m$. At extremely low height values (< *100 nm*), the CHF appears to revert towards the CHF of a flat surface. We now explore the reasons for such behavior.

4.2.5 Effect of area enhancement

To understand the role of area enhancement, the CHF data from fig. 4.9 are adjusted by determining an effective heat flux based on the enhanced area listed in Table 1 for various pillar diameter/height combinations. These area-normalized CHF data are plotted in fig. 4.10 as a function of pillar height.

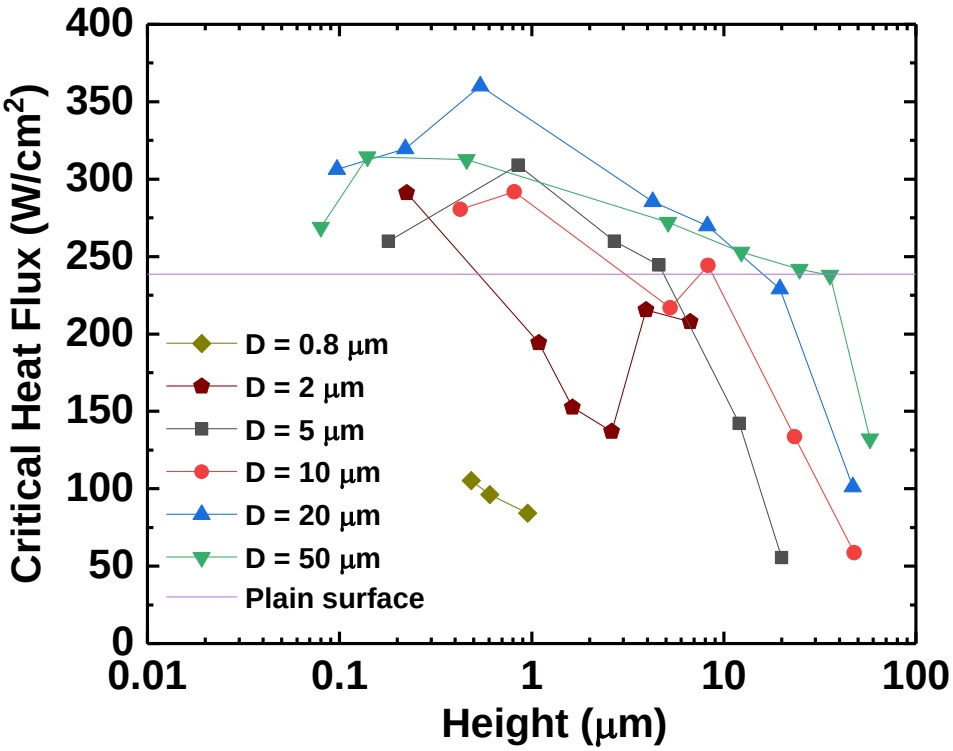

Fig. 4.10 CHF values based on enhanced area (list in Table 1) plotted against the micropillar height for various surfaces tested. The purple line corresponds to the CHF of the plain surface (q''_{CHF} = 238 W/cm²).

The curves for all pillar diameters continue to show a similar trend, reaching a maximum at an intermediate height between *0.2 μm* and *1 μm* in all cases. Beyond this height, area enhancement due to increased pillar height does not contribute to CHF. The area-normalized CHF falls below the plain surface, implying that the increases in CHF with increased height are less than the increases in the area. It is also clear that the significant increases in CHF with the reduction in pillar diameter cannot be explained based on area enhancement alone since the peak value of the area-normalized CHF is *25%* greater than that of the plain surface.

A closer look at figure 4.10 suggests that the height at which the area-normalized CHF falls below that of the plain surface scales with the pillar diameter (pore-scale). Accordingly, in figure 4.11, we replot the fig. 4.10 by scaling the height with the pore scale,

H/P. The resulting plot nearly collapses all the data into a single curve, suggesting that the mechanisms responsible for enhancing CHF are related to the value of aspect ratio *H/P*.

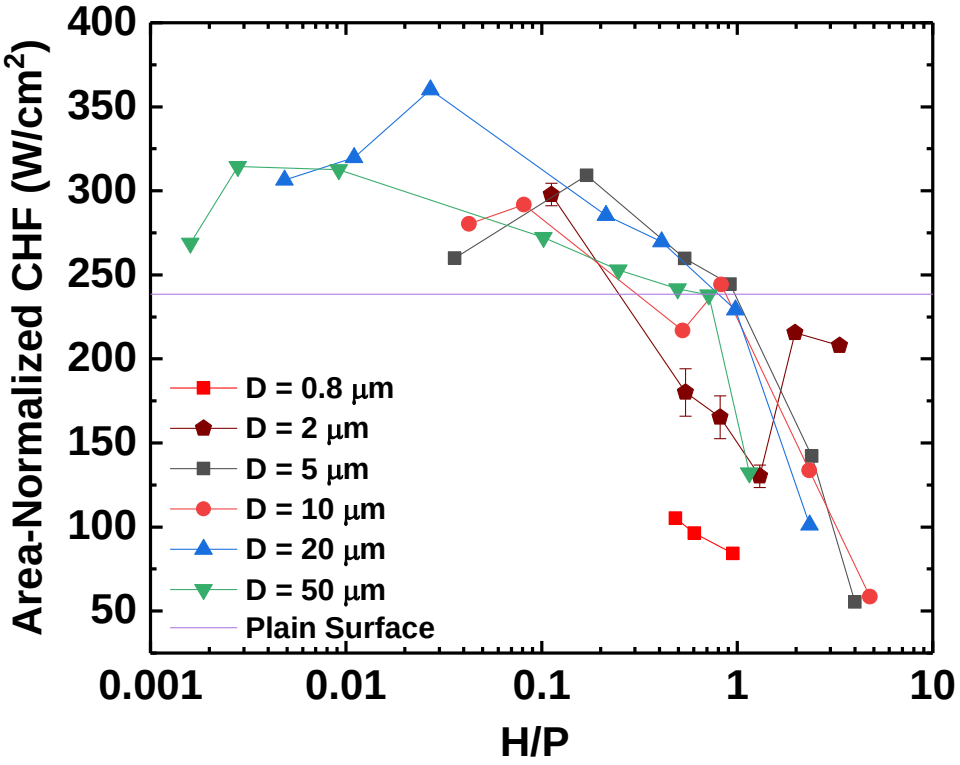

Fig. 4.11 Area-normalized CHF values as a function of the pillar aspect ratio. The purple line corresponds to the CHF of the plain surface (q''_{CHF} = *238 W/cm²*).

Contact-line evaporation driven by menisci capillary suction is the most plausible mechanism to produce sustained increases in heat flux due to surface area enhancement. We consider the behavior of the liquid meniscus in a pore along the heat transfer curve for three regimes corresponding to short (*H/P < 1*), moderate (*H/P ~ 1*), and large aspect ratios (*H/P > 1*). We assume that at moderately high heat fluxes within the two-phase regime, the liquid menisci are located at the top of the micro-pillars, with the contact line pinned at the top. Initially, the menisci curvature may be very low, leading to a nearly flat film. As the evaporative mass flux increases with increased applied heat flux, any region that is not supplied by droplet impingement on an instantaneous basis must maintain equilibrium through in-plane capillary flow. As meniscus curvature increases to drive the required mass

flow rate, the region of the thin liquid film extends down the side of the micropillar, increasing the effective heat transfer coefficient. If $H/P << 1$, the cross-sectional area for liquid flow is not large, the meniscus may touch the base area, and dry out may be reached before the liquid film on the side of the pillar becomes thin. This would be expected to lead to a low value of *CHF* as well as *HTC*. For all values of $H/P < 1$, the extent of the thin film region is independent of the height and solely dependent on contact line length around the pillars, resulting in a constant heat transfer coefficient. When $H/P \sim 1$, the lowest point of the meniscus at maximum curvature is very close to the base area, forming an additional region of the thin liquid film and enhancing evaporative mass flux (see fig. 4.12).

For $H/P > 1$, a reduction in heat transfer coefficient is expected. Tall micropillars ensure that the meniscus remains far away from the base, unlike the situation of $H/P \sim 1$. Additionally, for large values of *H/P*, fluid flowing towards a meniscus experiences more significant viscous drag due to the increased surface area of the micropillars. It is possible that at sufficiently large heights, the meniscus curvature cannot supply the required capillary pressure, leading to an overall reduction in mass flow. This may lead to contact-line depinning from the top of the micropillar at relatively low heat fluxes on the cooling curve. Eventually, the contact-line recedes towards the micropillar base triggers *CHF*.

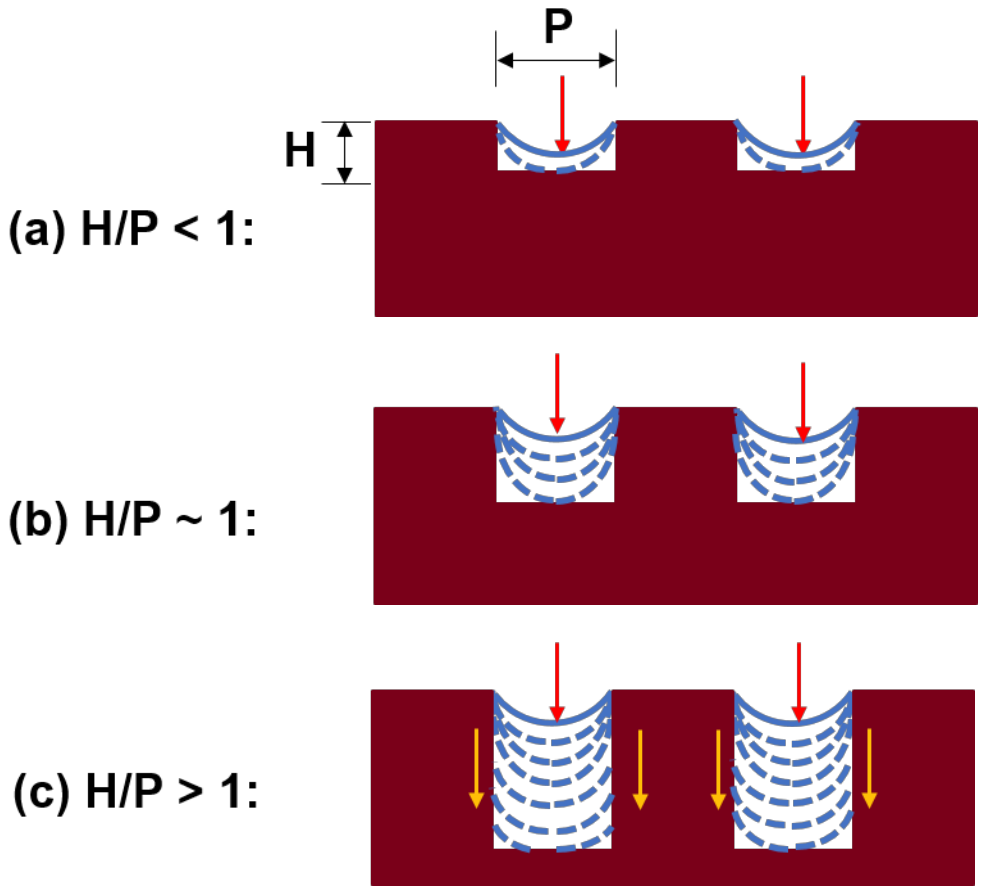

Fig. 4.12 (a) When *H/P < 1*, low CHF values due to premature dryout at the base, (b) When *H/P ~ 1*, liquid menisci anchored to the top of the micropillars at maximum curvature, enhancing thin film area and evaporative mass flux (c) *H/P > 1*, liquid menisci curvature cannot balance the increased drag, and may recede downwards, reducing CHF.

Considering the above picture, we re-examine the *CHF* data and the heat transfer coefficients at CHF in figures 4.13 and 4.14, now using *H/P* as the indicative parameter. The curves exhibit three zones of behavior:

(i) Thin-film evaporation on pillars (*H/P < 0.2*),

(ii) Extended evaporation zone (*H/P ~ 1*) and

(iii) Dry-out (*H/P > 1*).

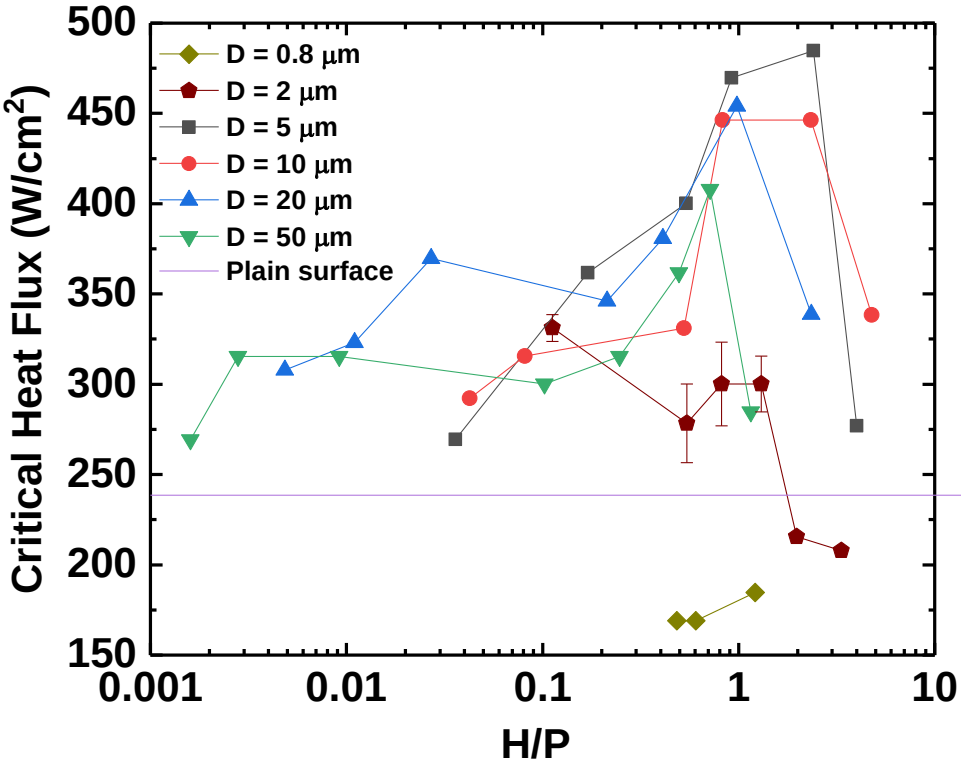

Fig. 4.13 *CHF* variation with height-to- spacing ratio, *H/P*, for various surfaces tested. The purple line corresponds to the *CHF* of the plain surface (q''_{CHF} = 238 W/cm²).

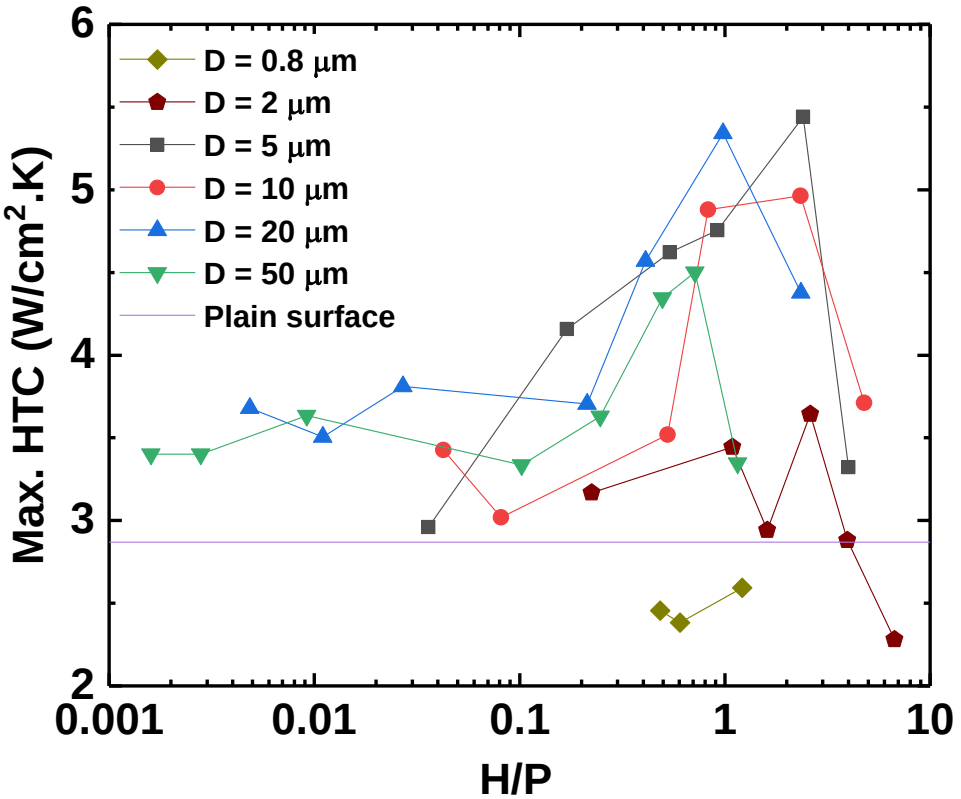

Fig. 4.14 Variation of the peak heat transfer coefficient with height-to-spacing ratio, *H/P*, for various surfaces tested.

We see that *CHF* values are low (fig. 4.13) due to the reduced cross-section area. Heat transfer coefficients are independent of height (fig. 4.14) since the thin film region is restricted to the pillars. The *CHF* values reach a maximum for surfaces with *H/P ~ 1*, consistent with the idea that the meniscus is at its maximum curvature, driving the maximum possible flow rate through the micropillar array. Simultaneously, there is a peak in the heat transfer coefficient (fig. 4.14), consistent with the flow configuration sketched in fig. 4.12, with an additional area of thin liquid film near the base of the pillar. Lastly, in the dry-out zone corresponding to *H/P > 1* (fig. 4.12c), the rapid decrease of the *CHF* values for large height suggests that the surface area of the micropillar array has increased such that the mass flow rate is reduced below the values at *H/P = 1*. The thin-film region remains confined to the micropillars and does not extend to the base, resulting in a drop in the heat transfer coefficient. Even at these significant heights, the actual *CHF* (without area normalization) remains more prominent than the *CHF* for the smooth surface, i.e., the *CHF* enhancement is lower than the area enhancement at large values of height.

4.2.6 Local Heat Transfer Coefficients (HTC) and apparent film thickness

Previous sections show the *CHF* enhancements can be achieved through minuscule change in the surface roughness and some microtextured surfaces show superior thermal performance as compared to others. Besides *CHF*, performance parameters like heat transfer coefficient in two-phase regime, liquid film thickness play in key role in deciding the spray cooling characteristics. To estimate heat transfer coefficient in two-phase regime, we assumed the sensible heat as the applied flux that produces a surface temperature of *100 °C*, i.e., the saturation temperature of deionized water. Further, it was assumed that all

heat flux values above this level as the two-phase heat flux caused by evaporation. Then, the heat transfer coefficient in the two-phase regime is calculated as follows:

$$h = \frac{q"act - q"sens}{T_s - T_{sat}} \tag{4.1}$$

The *HTC* values were plotted for all the heights tested for various heater surfaces (see figs. 4.15 – 4.19). Overall, *50-μm* and *20-μm* pillar-array surfaces show better performance in terms of *HTC* with values up to *20 W/cm^{2}K* – the highest HTC value reported in spray cooling literature. The surfaces with relatively lower pillar diameters (i.e., *10-μm, 5-μm, and 2-μm*) recorded local *HTC* values of around *15 – 17 W/cm^{2}K*. Note that the plain surfaces yield an *HTC* value of *~ 5 W/cm^{2}K*. Interestingly, the *0.8-μm* samples attained *CHF* before reaching the saturation temperature. Hence, the associated *HTC* values were not reported.

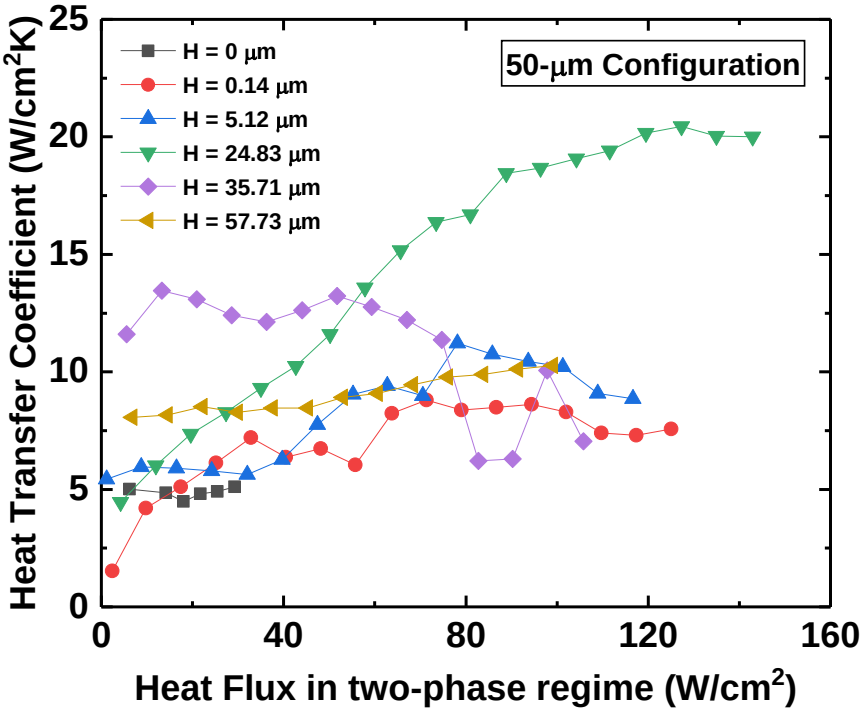

Fig. 4.15 Local heat transfer coefficients (HTC) obtained for various heights corresponding to 50 μm pillar diameters. Here, the maximum HTC ~ 20 W/cm^{2}K.

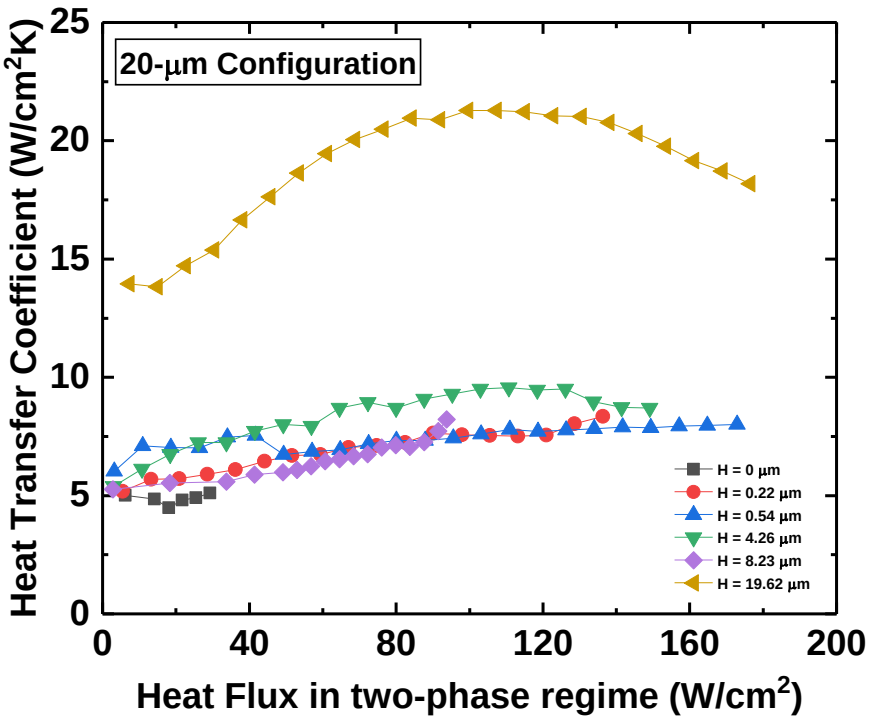

Fig. 4.16 Local heat transfer coefficients (*HTC*) obtained for various heights corresponding to *20 μm* pillar diameters. Here, the maximum HTC ~ *23 W/cm²K*.

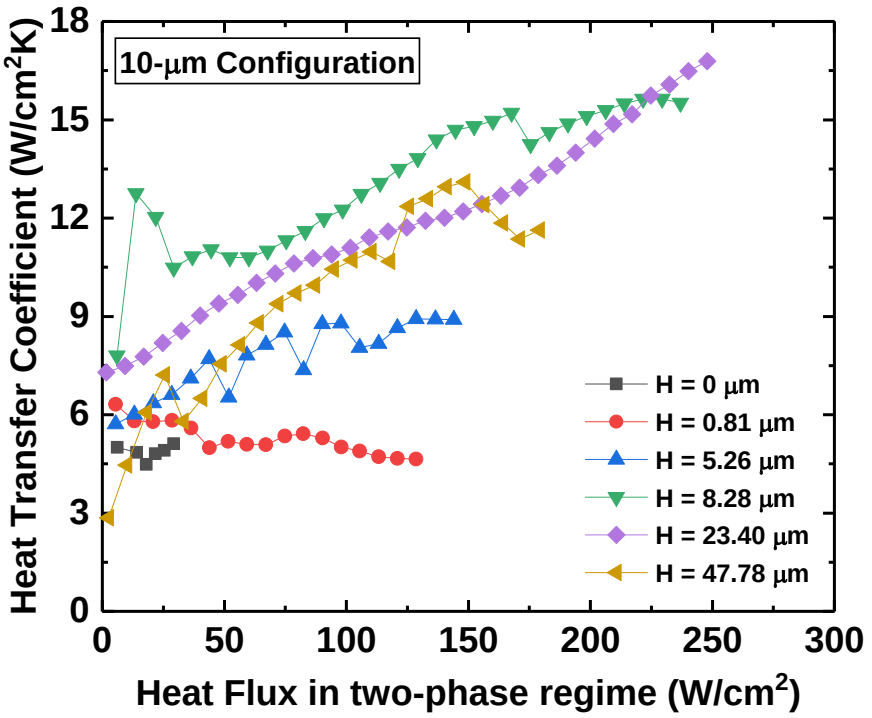

Fig. 4.17 Local heat transfer coefficients (*HTC*) obtained for various heights corresponding to *10 μm* pillar diameters. Here, the maximum HTC ~ *17 W/cm²K*.

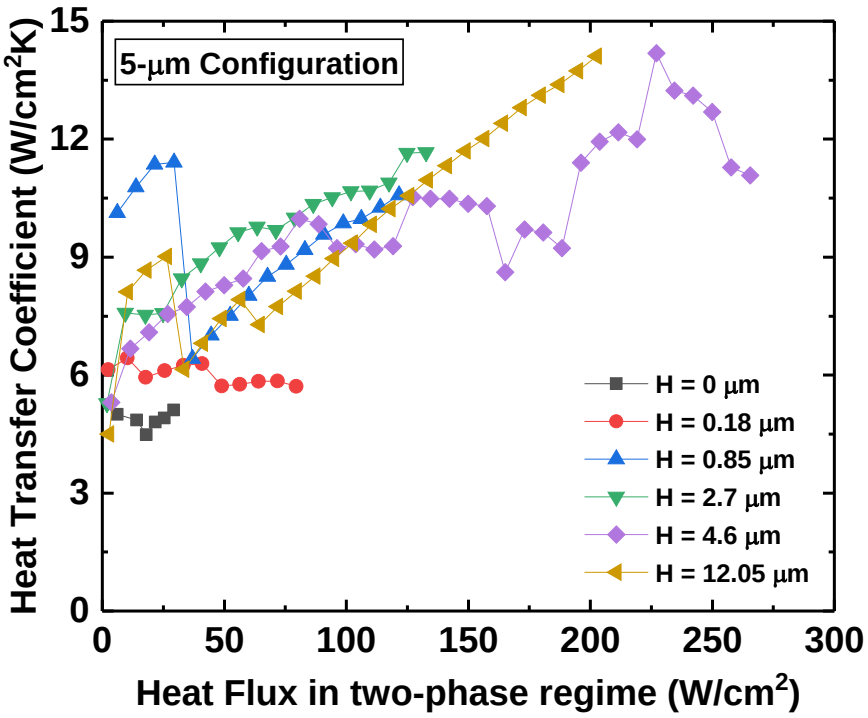

Fig. 4.18 Local heat transfer coefficients (*HTC*) obtained for various heights corresponding to *5 μm* pillar diameters. Here, the maximum *HTC ~ 14 W/cm²K*.

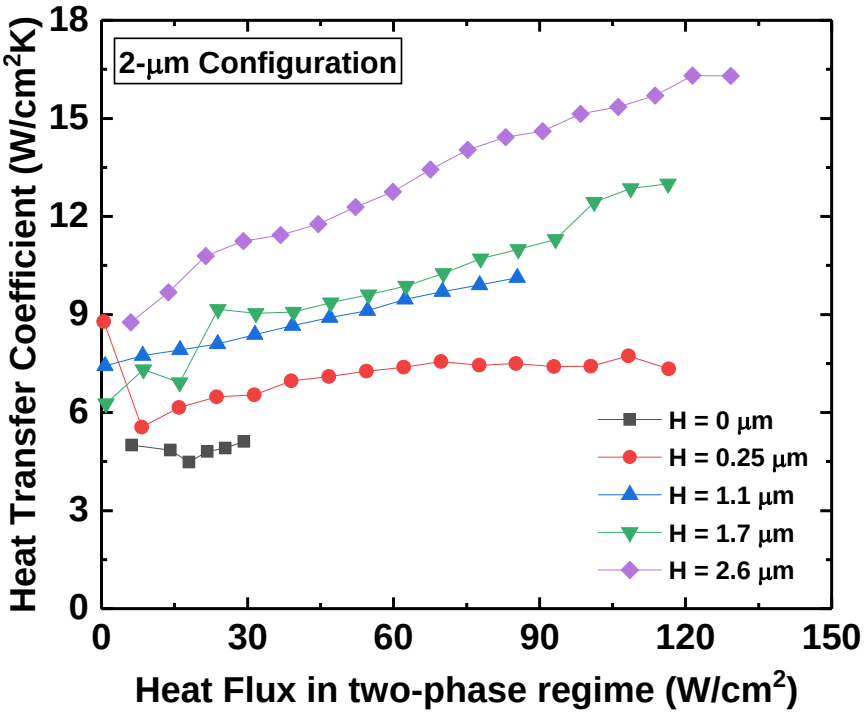

Fig. 4.19 Local heat transfer coefficients (*HTC*) obtained for various heights corresponding to *2 μm* pillar diameters. Here, the maximum *HTC ~ 16 W/cm²K*.

Although the *10-μm* and *5-μm* samples show improved heat transfer performance in terms of *CHF*, the *HTC* values are relatively low compared to *50-μm* and *20-μm* samples (see fig. 4.15 and 4.16). Following the theory proposed by Hsieh & Yao [59], the *50 μm* and *20 μm* samples could potentially offer more floor area for the evolving menisci to spread and enhance the evaporative mass flux at the liquid-vapor interface.

Typical features of spray cooling include high CHF and heat transfer coefficient with small film thickness values. This paper estimates the apparent film thickness values from the heat transfer coefficients obtained in the two-phase regime. The apparent liquid film thickness values at the CHF point (based on the heater area) were calculated using eqn. 3 and its variation with the pillar height were plotted in fig. 4.20:

$$t = \frac{k}{h} \tag{4.2}$$

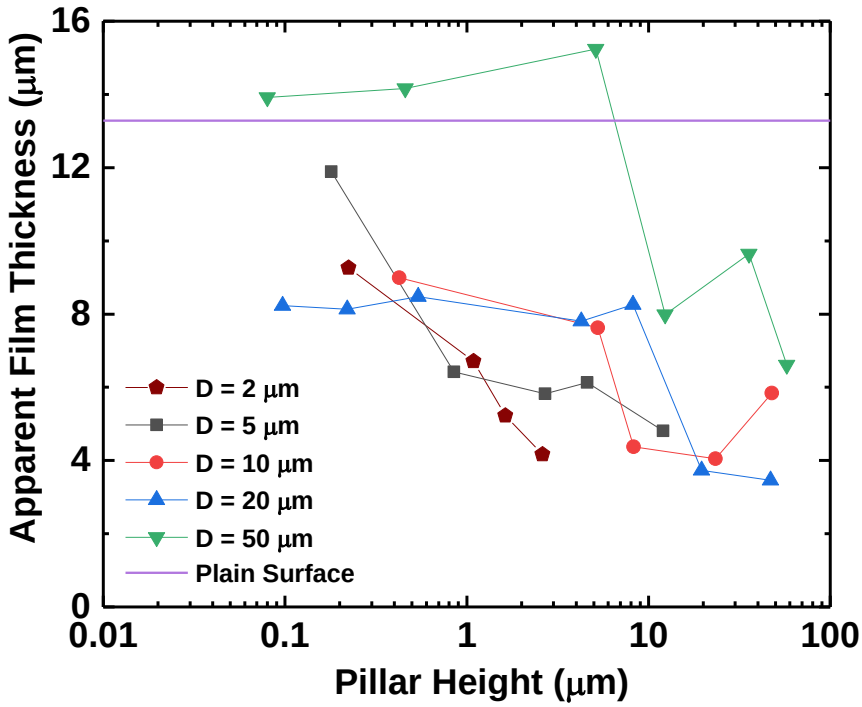

Fig. 4.20 Apparent liquid film thickness plotted against micropillar height for various surfaces tested.

The purple line indicates the apparent liquid film thickness of the plain surface. The apparent film thickness value reduces monotonically with height due to area enhancement for a given micropillar configuration. The *50-μm* surfaces, especially those with lower pillar heights, tend to form relatively thicker liquid films compared to the plain surface. Consequently, the thicker films yield diminishing returns in the heat transfer coefficient (< *10 W/cm²K*). In addition, all the configurations could form film thickness values less than *10 μm*; thus, promoting more substantial evaporation through heat conduction.

4.2.7 Spray Cooling Efficiency

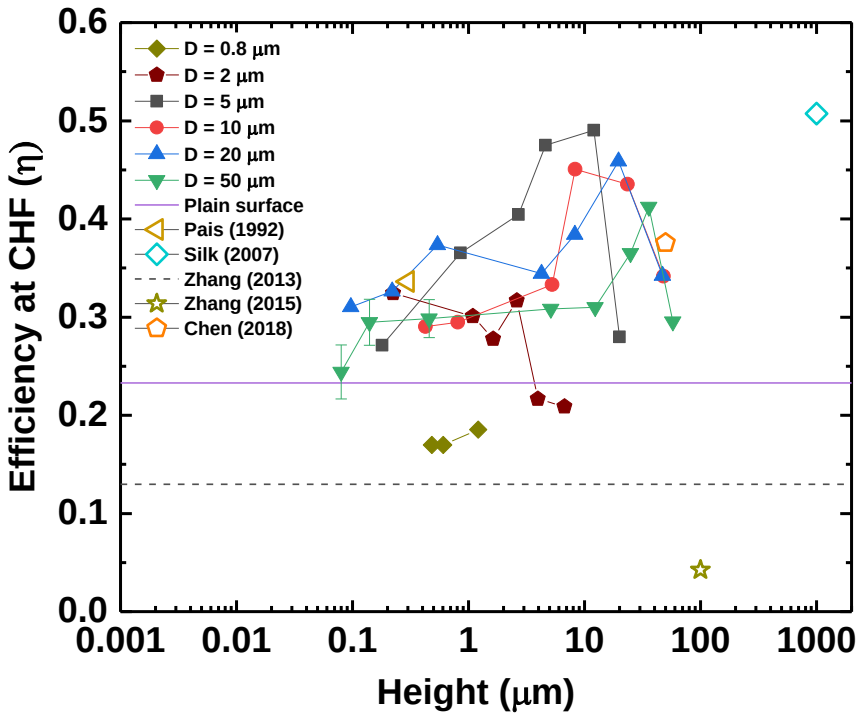

Fig. 4.21 Maximum cooling efficiency data plotted against micropillar height for various surfaces tested.

In figure 4.21, we present the cooling efficiency at *CHF* for all configurations studies. The peak efficiency reaches *48%* for the *5-μm* pillar configuration (*H ~ 12 μm*). Also shown are the values attained by other investigators, along with the roughness scale and maximum heat fluxes. Interestingly, Pais et al. [15] of *1250 W/cm²* using water attained the highest

heat fluxes, with efficiencies of *33.5 %*. Other studies that achieve higher efficiencies than in the present study (e.g., Silk et al. [21]) used wetting fluids such as refrigerants, with comparatively lower heat fluxes ~ $100\ W/cm^2$. The data presented suggest that surface roughness in the *5 - 50 μm* range may offer a route to high efficiency, high heat flux spray cooling.

4.3 Summary

The effects of roughness parameters on heat transfer performance were studied. Key outcomes of this study are outlined below.

1. CHF maxima exist for all the families of textured surfaces tested. Based on the results obtained and insights gained, surfaces with roughness such that pillar diameter (*D*) ≈ pillar spacing (*P*) ≈ pillar height (*H*) is preferred. It is shown that *5-μm* and *10-μm* pillar arrays exhibit maximum spray cooling performance with CHF around ~ $480\ W/cm^2$.
2. The transition from Cassie–Baxter state to Wenzel state is critical for liquid penetration into the forest of micropillar array elements. Surfaces with *2-μm* and *0.8-μm* pillar arrays exhibit inferior cooling performance due to low liquid penetration.
3. Surfaces with *50-μm* and *20-μm* micropillar arrays show the highest heat transfer coefficients (~$20\ W/cm^2K$). The availability of more floor area for menisci stretching during the wetting process and intense evaporation at the liquid-vapor interfacial area made these surfaces record higher *HTC* values.

Chapter 5

Effect of pillar spacing and flow rates

5.1 Introduction

The previous chapter examine the effect of varying pillar diameter and pillar height on CHF and other performance parameters, while keeping the porosity constant ($\phi = 0.75$). In this chapter, the effects of pillar spacing (i.e., the porosity) is investigated. As mentioned in Chapter 3, pillar diameters ($5\ \mu m$ and $10\ \mu m$) that recorded best thermal performance were used for this study. CHF values and other performance parameters were enumerated.

5.2 Experimental results

5.2.1 Spray characteristics

A shadowgraph imaging system was used to obtain the droplet size distribution of the liquid spray. All the spray cooling experiments were performed with the liquid spray produced using the flow settings mentioned in the previous chapter (i.e., Water flow rate = *30 ml/min*; Air flow rate = *13.7 slpm*). Image visualization using shadowgraphy revealed the liquid spray in the given flow settings delivered droplet sizes around $22\ \mu m - 45\ \mu m$. To quantify the spray cooling performance, several macroscale heat transfer parameters like *CHF*, *HTC*, and film thickness values were calculated and reported in the following subsections.

5.2.2 Effect of pillar spacing on CHF

Figures 5.1 and 5.2 displays a plot containing the cooling curves obtained for the plain surface and the micro-textured surfaces listed in Table 1 [82]. Subcooled DI water *(~ 20 °C)* was used for the spray cooling experiments. Hence, the single-phase regime is distinctly visible in the graph. With the increase in the applied heat flux, heat transfer due to evaporation near the contact-line region becomes dominant. This transition to a two-phase regime removes large amounts of heat flux through latent heat with relatively low surface temperature changes. Beyond a point, the heat transfer capability of the liquid spray saturates, and the sample reaches the *CHF* zone.

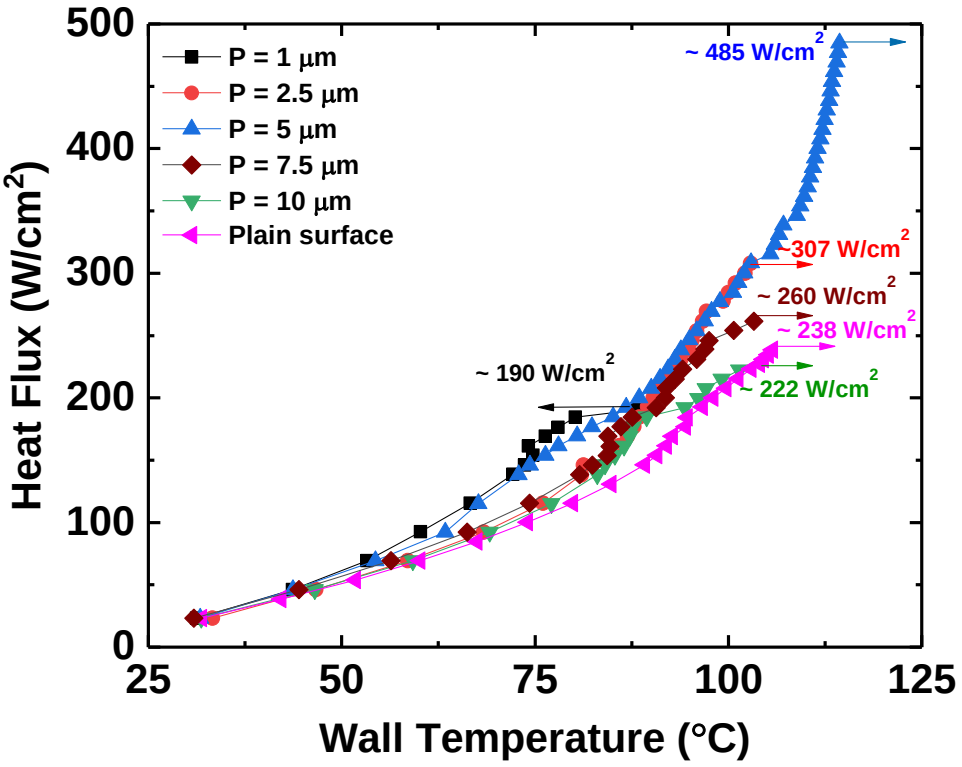

Fig. 5.1 Spray cooling curves corresponding to surfaces with pillar diameter of *5 μm*, heights around ~9 *μm* and various pillar spacing.

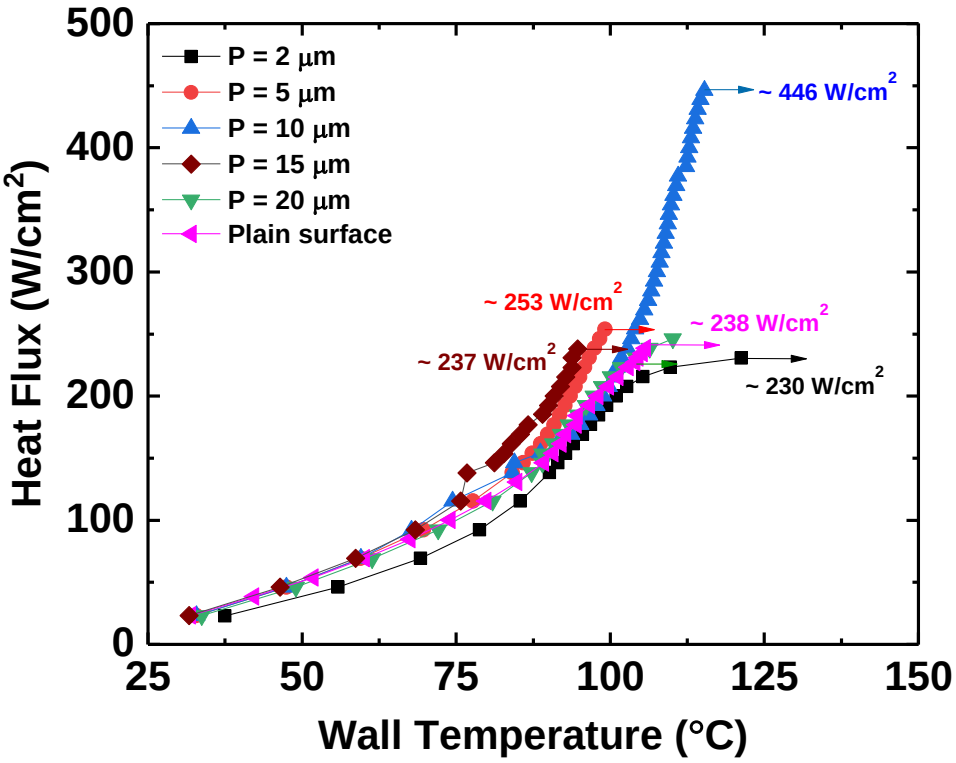

Fig. 5.2 Spray cooling curves corresponding to surfaces with pillar diameter of *10 μm*, heights around ~9 *μm* and various pillar spacing.

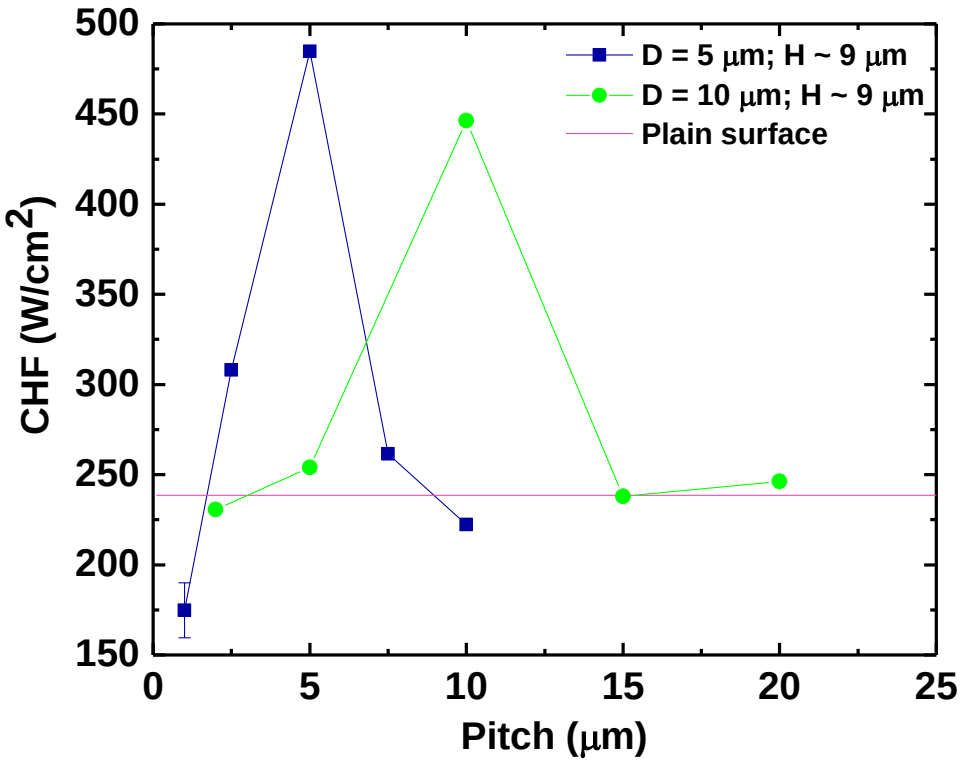

Fig. 5.3 CHF data plotted against the pitch. Distinct peaks can be seen at spacing values of *5 μm* and *10 μm* for *5-μm* and *10-μm* configuration, respectively.

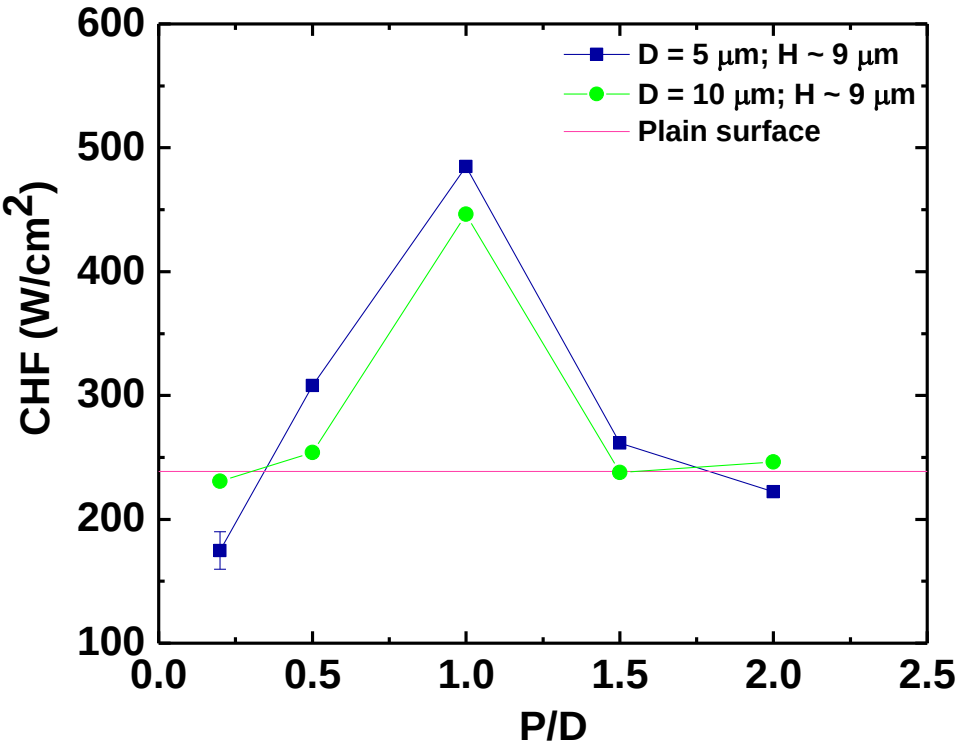

Fig. 5.4 CHF data plotted against the spacing to diameter ratio. Distinct peaks at *P/D = 1* show

To investigate the effect of porosity variation, the spacing between the pillar arrays was varied while keeping the pillar diameter and height to be constant. Since surfaces with *5-μm* and *10-μm* pillar arrays yielded better performance results, the pillar diameter was chosen to be *5-μm* and *10-μm* for the porosity variation study. The surfaces with a pillar diameter-to-spacing ratio of one show maximum CHF values, as seen in the fig. 5.4. These results directly contradict the theory proposed by Hsieh & Yao [59]. The authors reported high *CHF* values for pillar-arrayed surfaces with larger spacing (i.e., *P>D*). They claimed that a large floor area (i.e., solid-liquid interfacial area) should contribute to more evaporation. However, Horacek et al. [5] and Plawsky et al. [1] surmised that the liquid-vapor interfacial area contributes and promotes more substantial evaporation at the contact-line region.

5.2.3 Effect of water/air flow rates on CHF

In this section, we discuss the effects of variation in air and liquid flow rates, keeping the nozzle-surface distance at the same fixed value of *40 mm*. Figure 5.5 shows the effects of varying air flow rate from *6.7 liters/min* (*ALR = 0.27*) to *26.7 liters/min* (*ALR = 1.11*) for a constant liquid flow rate of *30 ml/min*, and a test surface with *20 μm* pillars of height *~19.42 μm*. The values of *SMD* for the three air-flow rates are around *35, 42, and 44 μm*, respectively. It is seen that the effect of increasing *ALR* is to increase the *CHF* up to some extent (*ALR = 0.57*), above which the *CHF* decreases. Thus, there is an optimum value of *ALR* for each liquid flow rate at which the *CHF* is maximum.

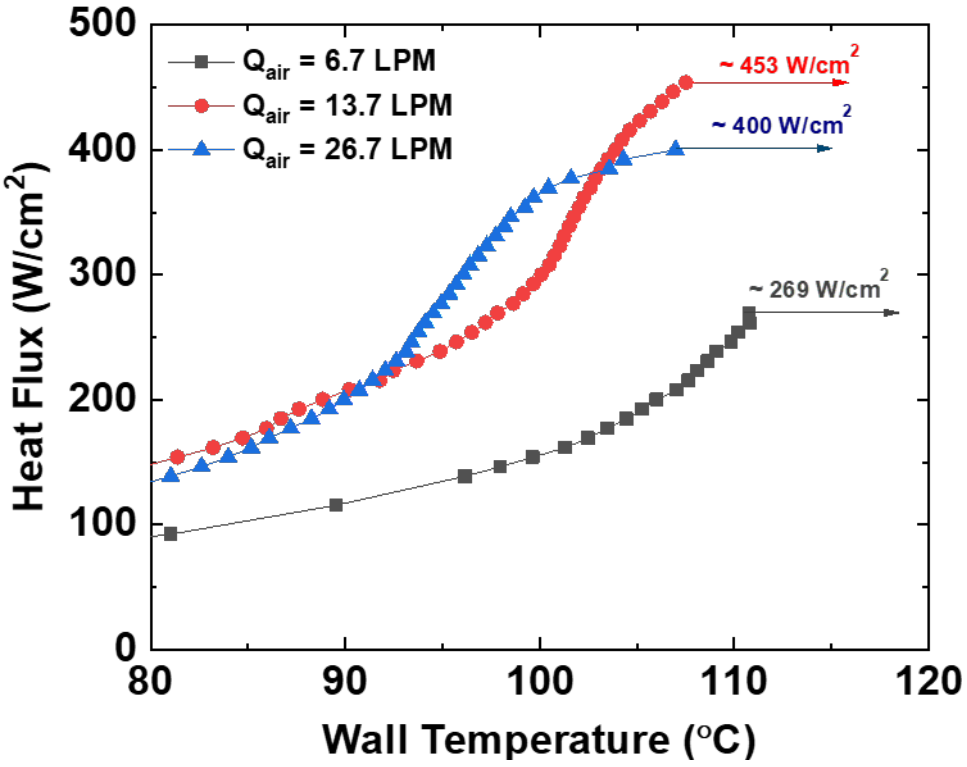

Fig. 5.5 Cooling curves obtained for various air flow rates. For all the three experiments, the water flow rate was kept constant at *30 ml/min*. Maximum *CHF ~ 453 W/cm²* recorded for the air flow rate of *13.7 slpm*.

Lastly, we fix the air flow rate at an optimum value of *13.7 liters/min* and consider the effects of varying liquid flow rate, for a surface with a micropillar array of size *20 μm* and

height *19.42 μm*. As the liquid flow rate is increased from *30 to 60 ml/min*, the *CHF* value increases from *452 W/cm²* to *723 W/cm²* (see fig. 5.6); however, a further increase in flow rate to *82 ml/min* yields a smaller increase (*CHF ~ 830 W/cm²*). We observed that at the highest flow rate, the small orifice diameter of the nozzle (*0.8 mm*) produced poor jetting atomization, accompanied by a very non-uniform distribution in the volumetric flux. This led to observable flooding in the central part of the test surface and scarcity of coolant on the edges, likely causing the apparent nonlinear scaling of the *CHF* with liquid flow rate.

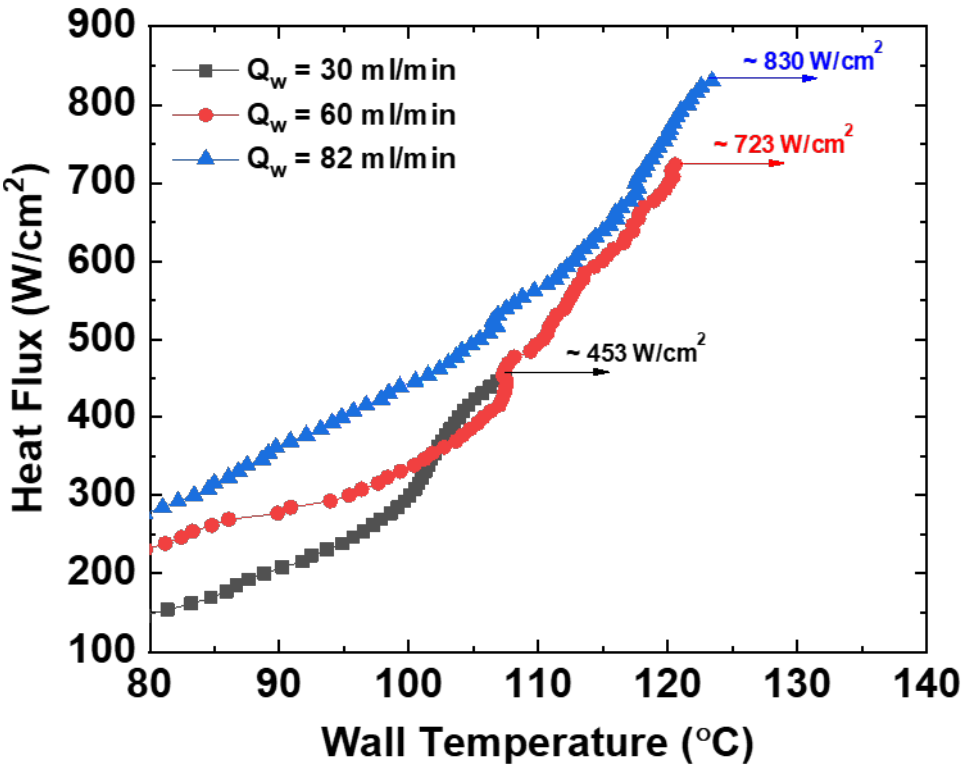

Fig. 5.6 Cooling curves obtained for various water flow rates. Highest *CHF ~ 830 W/cm²* recorded for the water flow rate of *82 ml/min.*

5.3 Discussion

In the two-phase regime, evaporative heat transfer occurs primarily in the areas where the conduction resistance of the liquid layer is lowest, i.e., near the triple-phase contact line. Direct evaporation through heat conduction is favored where the film thicknesses are

low; bubble nucleation is not favored since any bubble growing in the liquid film shall quickly encounter the liquid-vapor interface and collapse. High heat flux values promote intense evaporation at the contact-line regions, thereby removing large amounts of heat from the surface. High evaporation rates at the contact-line region cause the menisci to recede and increase the local curvature. This, in turn, increases the Laplace pressure and promotes the in-plane liquid flow through capillary action. This regular sequence of droplet impingement, spontaneous film formation through capillary action (or wetting phenomena), evaporation/de-wetting, and re-wetting enables sustainable two-phase cooling/quenching of the heated surface. CHF occurs when this two-phase cooling cycle collapses, possibly, due to enormous evaporation rates where re-wetting is hindered or due to abnormal expansion of hot-spot regions.

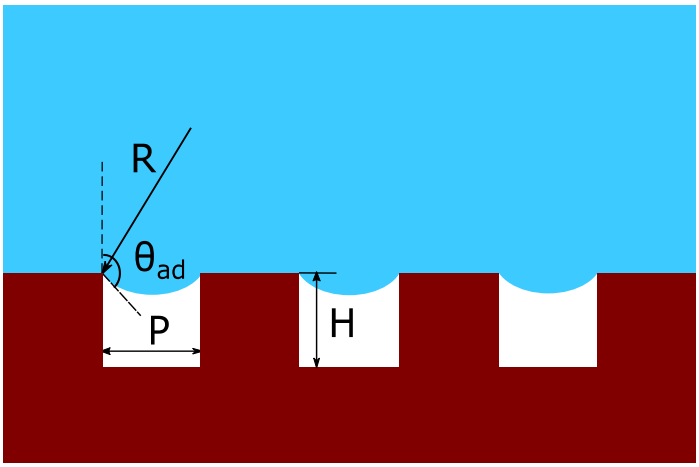

Fig. 5.7 Illustration of the sagging liquid menisci (in the Cassie−Baxter state) on the tightly packed pillar array.

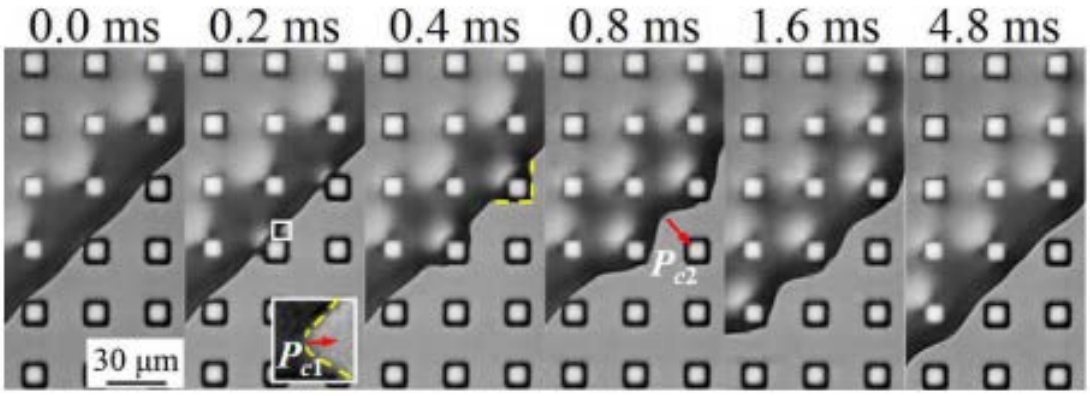

Fig. 5.8 Time series images of liquid (μ = 5 mPa.s) spreading on pillar-arrayed surfaces. P_{c1} and P_{c2} represent the local capillary pressures [83].

For low Weber numbers, Murakami et al. [84] investigated the wetting transition of water and other ionic droplets from the Cassie–Baxter state to the Wenzel state on adiabatic, textured surfaces. They reported that this transition was dominated by the competition between the energy barrier between the two incumbent states and the Laplace pressure. For a sagging liquid droplet in the Cassie–Baxter state (see fig. 5.7), the upward pressure preventing the droplet penetration is given by eqn. 5.1.

$$\Delta P_{EB} \sim \frac{H}{P^2}(\gamma_{SL} - \gamma_{SV}) \tag{5.1}$$

And the downward Laplace pressure favoring the droplet penetration is given by eqn. 5.2.

$$\Delta P_{lap} \sim \frac{\gamma}{R} \sim \frac{\gamma}{P} \tag{5.2}$$

From a hydrodynamic perspective with *We < 60*, due to comparatively low spacing between the pillars (for *2 μm* and *0.8 μm* surfaces), the Laplace pressures required to break the energy barrier have been reduced by a factor of *1/P*. Hence, reduced Laplace pressure causes the droplet to sag on the pillars, leaving the floor un-wetted. Therefore, these surfaces display inefficacy in forming a thin and continuous film, which is a prerequisite for spray cooling phenomena. The same theory explains why the *5-μm* and *10-μm* surfaces with low porosity values (i.e., *P/D < 1*) performed poorly. On the other extreme, surfaces

with high porosity values (i.e., *P/D < 1*) also exhibited relatively low CHF values. This diminishment in the performance can be explained using the dynamic spreading model proposed by Yuan et al. [83] for pillar-array surfaces. In-plane capillary wicking is primarily driven forward by two local Laplace pressures (refer to fig. 5.8) – (1) $\Delta P_{c1} \sim \gamma_{LV}/D$, acts along the corners of pillars and responsible for liquid encapsulation around the pillars, (2) $\Delta P_{c2} \sim \gamma_{LV}/P$, acts diagonally across the pillars along the direction of the moving contact line and is responsible for wetting the non-pillar areas. For a given pillar diameter, ΔP_{c1} stays constant; however, ΔP_{c2} varies inversely with the pillar spacing. Hence, surfaces with larger pillar spacing offer relatively low Laplace pressure for the menisci to overcome the viscous drag and spread across the empty region between the pillars. Very high curvature is one another effect that inhibits performance at small scales, which can cause significantly lower the Laplace pressure and inhibit evaporation, unless the liquid is strongly superheated (given by Schrage equation, eqn. 5.3). You should add this with the Schrage equation.

$$\dot{m}_{flux}(p_{interface}, T_{interface}) = \frac{2}{2-\sigma_{cond}} \sqrt{\frac{MW}{2\pi R_u}} \left(\sigma_{evap} \frac{p_{sat}(T_{liq})}{\sqrt{T_{liq}}} - \sigma_{cond} \frac{p_{vap}}{\sqrt{T_{vap}}} \right) \qquad (5.3)$$

5.4 Summary

The effects of roughness parameters on the heat transfer performance were studied. Key outcomes of this study are outlined below.

1. CHF maxima exist for pillar spacing as well, with micropillars of *P/D ~ 1* showing maximum heat transfer performance as compared to smaller and larger *P/D* ratios.
2. The transition from Cassie–Baxter state to Wenzel state is critical for liquid penetration into the forest of micropillars. In the previous chapter, we discussed

surfaces with *2-μm* and *0.8-μm* pillar arrays exhibit inferior cooling performance due to low liquid penetration. This theory stands valid for surfaces with small pillar spacing, i.e., $P/D < 1$. In-plane Laplace pressures become important to ensure complete wetting. Hence, pillar-arrayed surfaces with $P/D > 1$ show diminishing results.

Chapter 6

Contact-line measurement

6.1 Introduction

The systematic study discussed in Chapters 4 and 5 was limited to space-averaged thermal measurements. Aspects of the spray cooling phenomena such as the impact dynamics of the liquid spray on the heated surface, droplet interaction, liquid film stability, and their subsequent effect on the temperature distribution remain unknown. Visualization of the solid/liquid/vapor interface is necessary to characterize the spatial and temporal effects of these phenomena.

The purpose of this research is to determine the role of contact-line dynamics on the heat transfer performance and examine the ramifying effects that the local contact-line parameters have on the global heat transfer performance. A transparent heater fabricated with a Sapphire wafer was used to visually map the wetted regions on the heated surface using the total internal reflectance (TIR) technique.

6.2 Experimental technique

6.2.1 Total internal reflectance technique

Total internal reflection is an optical phenomenon. Light waves arriving at the interface from a denser medium to rarer medium, at an angle greater than the critical angle, tend to get reflected entirely to the first medium rather than refracting into the second medium. Here the angle is measured from the normal to the interface, meaning that shallow/grazing

angles nearly parallel to the interface are likely to undergo total internal reflection. This total internally reflected light carries valuable information about the structures at or nearby the interface. When light travels from a denser medium to a rarer medium, the ensuing optical phenomenon is shown schematically in Fig. 3. Total internal reflectance microscopy has been extensively used to study spray cooling [5], [85], pool boiling [86], [87], and cell biology [88].

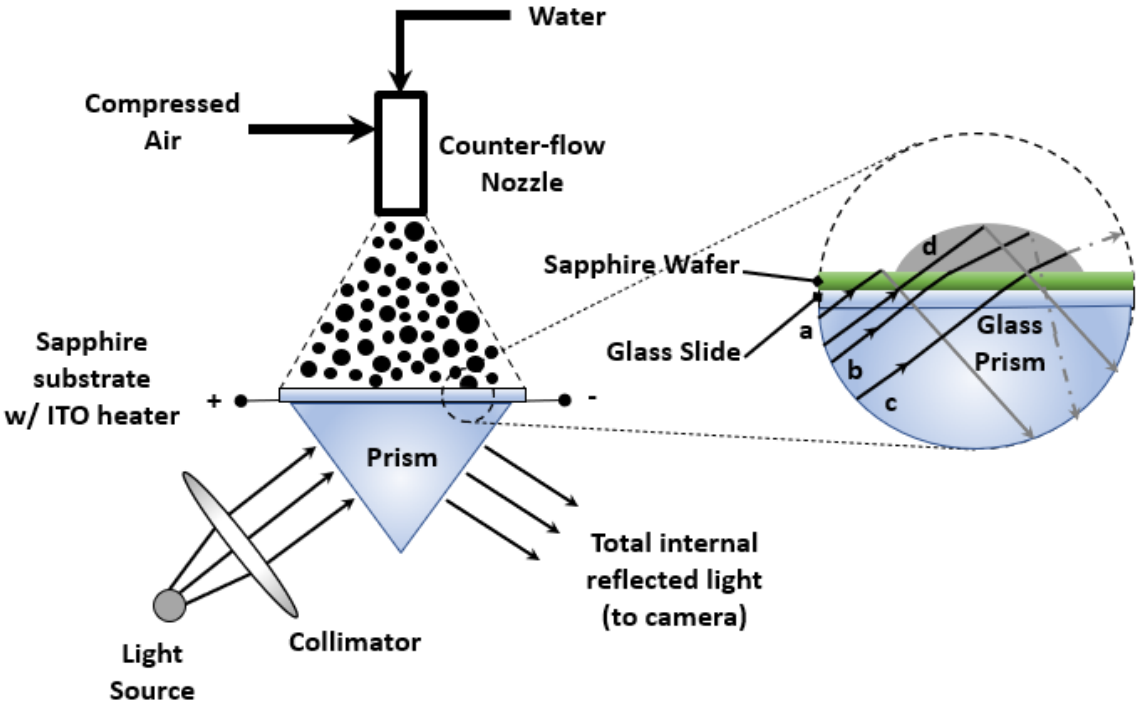

Fig. 6.1 Schematic of the total internal reflectance (TIR) microscopy.

A right-angled prism (Refractive index, $n \sim 1.517$) was placed in contact with the underside of the glass slide ($n \sim 1.52$) on which the sapphire substrate ($n \sim 1.78$) was mounted. The critical angle for total internal reflection from the sapphire substrate to air/water vapor ($n \sim 1.00$) is approximately $36°$. Hence, a right-angled glass prism was the right choice to direct the light into the sapphire substrate. An optical immersion oil was used to fill the air gap between the prism and the glass slide. Collimated light from a green

LED light source strikes the glass prism. It can potentially trace through the medium in the following pathways (See fig. 6.1): Light incident at the sapphire/vapor interface (Ray *a*) at an angle greater than the critical angle, gets reflected into the glass prism and is thus seen brighter the camera. On the other hand, light incident (Rays *b–d*) on the Sapphire/liquid interface is refracted, i.e.,

Ray *b* – transmitted into the liquid and reflected into the liquid medium at the curved liquid/vapor interface (seen darker by the camera),

Ray *c* – refracted into the vapor medium,

Ray *d* – internally reflected by the perfectly parallel liquid/vapor interface, occurs rarely but may have the same light intensity as Ray *a*.

Thus, mapping the darker/brighter regions shall accurately estimate the wetted area fraction and associated contact-line parameters.

6.2.2 Sample Design and fabrication

Previous experiments used Silicon as a substrate due to ease of fabrication in a cleanroom. The TIR experiments demand optical transparency to observe the structures at and near the solid/liquid interface. Samples were made from *2"* diameter sapphire wafers. With high thermal conductivity (equivalent to that of stainless steel) and optical transparency, sapphire wafers (Thickness ~ *430 μm*) address both the thermal and visual needs for conducting TIR experiments. Figure 6.2 shows the fabrication process flowchart used to create the micropillar geometries on the Sapphire surface.

The double-side polished silicon wafer (*100 mm* diameter, *525 μm* thick) was cleaned three times using the common solvents in the following order – Acetone, Isopropyl alcohol, and DI water. Piranha clean may potentially react with sapphire and destroy the polished

topography; hence, avoided. Sapphire wafers are hard to etch using the available wet-etch and dry-etch recipes. So, a thick layer of amorphous SiO_2 (~ *5 μm*) is deposited on top of sapphire using the Plasma-enhanced chemical vapor deposition (PECVD) process (refer to fig. 6.2 for the process flowchart). The SiO_2 layer is then dry etched to obtain micropillars. The deposition process was carried out at *150 °C* to obtain a film with a refractive index of about *~1.45*.

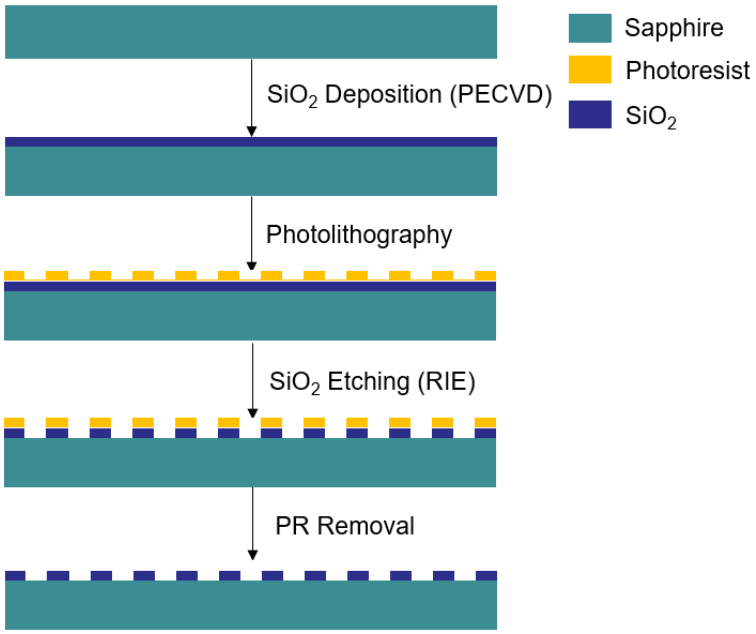

Fig. 6.2 Fabrication process flowchart used to create low-aspect-ratio pillar arrays on Sapphire wafers.

The deposition process was split into six layers to avoid the formation of pinholes within the SiO_2. Between each layer depositions, the PECVD chamber was vented, and the sample substrate was cleaned by blowing dry N_2 to obtain a good quality film.

The resulting wafer was then heated to *150 °C* for 6 minutes and exposed to HMDS vapor for 6 minutes to promote PR adhesion. Next, the pre-processed wafer was spin-coated with a positive photoresist (AZ 1512) at 3000 rpm for 30 seconds and pre-baked at

100°C for 2 minutes. The pre-baked wafer is then exposed to UV light to transfer the micropillar array pattern from the chrome mask to the photosensitive layer and post-baked at *95°C* for 2 minutes. The post-baked wafer is developed using an aqueous solution with the AZ 340 developer (1:5 H_2O by volume). After lithography, the SiO_2 layer is etched to the desired height using a deep reactive ion etching process (Oxford Etcher). The remaining photoresist was removed using acetone, and the wafer was spin-rinse-dried using deionized water and nitrogen.

An e-beam deposition process was used to deposit Indium Tin Oxide (ITO) film (Sheet Resistivity ~ *60 Ω*) of thickness *~130 nm* on the backside of the wafer before dicing it into a rectangular chip (*13 × 10 mm*^{2}). Samples were then characterized using a scanning electron microscope (see fig. 6.3). The samples were rinsed using standard solvents such as acetone, isopropyl alcohol, and deionized water at least three times before the post-processing step.

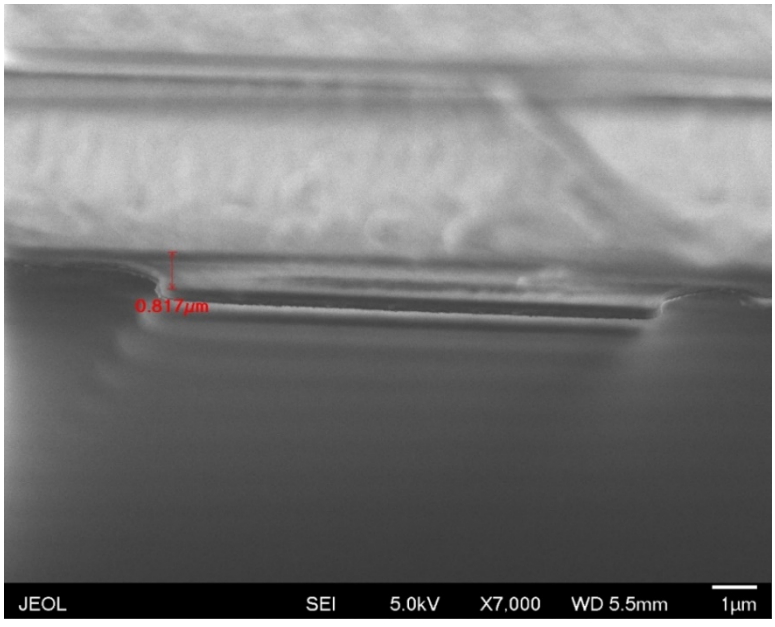

Fig. 6.3 A SEM image (right) featuring the surface topography (upside down) of the *10-µm* micropillar configuration.

6.2.3 Sample post-processing

The pre-cleaned chip was fixed on a *1 mm* thick glass slide using silver epoxy (Chemtronics® CW2460) and copper tapes. Before positioning the sapphire chip, a small quantity of immersion oil (Type 37) with a refractive index *~1.51* produced by Cargille Laboratories was carefully introduced between the glass slide and sapphire chip to avoid refraction air gap. The resulting configuration is heated to 150°C using resistive heating for 10 minutes to ensure the silver epoxy was cured. On the bright side, the curing process reduces the viscosity of the immersion oil (which is, otherwise, as vicious as Glycerin *~1250 cSt ± 10% @ 37°C*). It lets it spread evenly across the chip through capillary action. This curing process ensures that a thin and continuous film of immersion oil is spread out between the glass slide and sapphire chip and sustains optical transparency at high temperatures (*~ 100 - 150°C*). A pair of shielded wires were soldered to the copper tapes, and this entire assembly is mounted on the sample stage using Kapton^{TM} tapes. The resultant resistance of the heater assembly was found to be less than *~1%* of the ITO film resistance.

6.2.4 Testing procedure

Figure 6.4 shows the schematic of the spray cooling test rig with the optics necessary for the TIR microscopy.

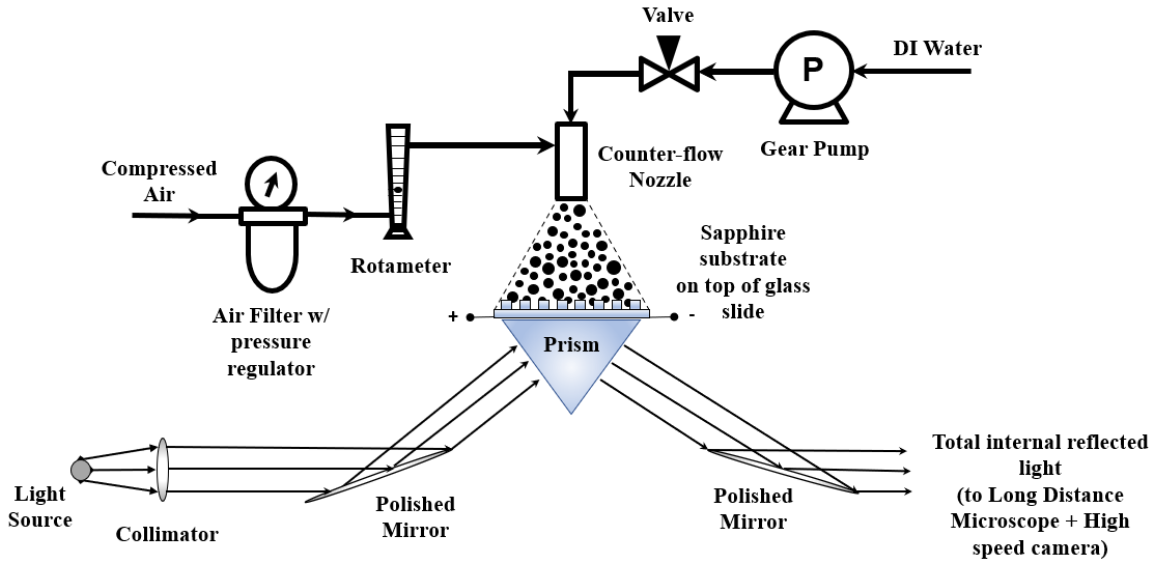

Fig. 6.4 Schematic of the spray cooling test rig featuring the optics used for total internal reflectance (TIR) microscopy.

The pneumatic- and hydro-mechanical systems of the experimental setup are the same as those used for the heat transfer experiments. The counterflow nozzle was operated at a water flow rate of *30 ml/min*, corresponding to an air-to-liquid ratio of *0.57*. Changes were needed to house the prism and hold it tightly to the underside of the glass slide containing the sapphire chip. Thus, the sample stage (refer to figs. 6.5 and 6.6) was remodeled and 3D-printed using high-quality ABS plastic for the TIR experiments. The glass prism is housed in the V-pocket, and a top cover was used to clamp down the glass slide and prism tightly. The shielded wires were then connected to a programmable power supply (Keysight N5771A) to supply power and measure the heat flux.

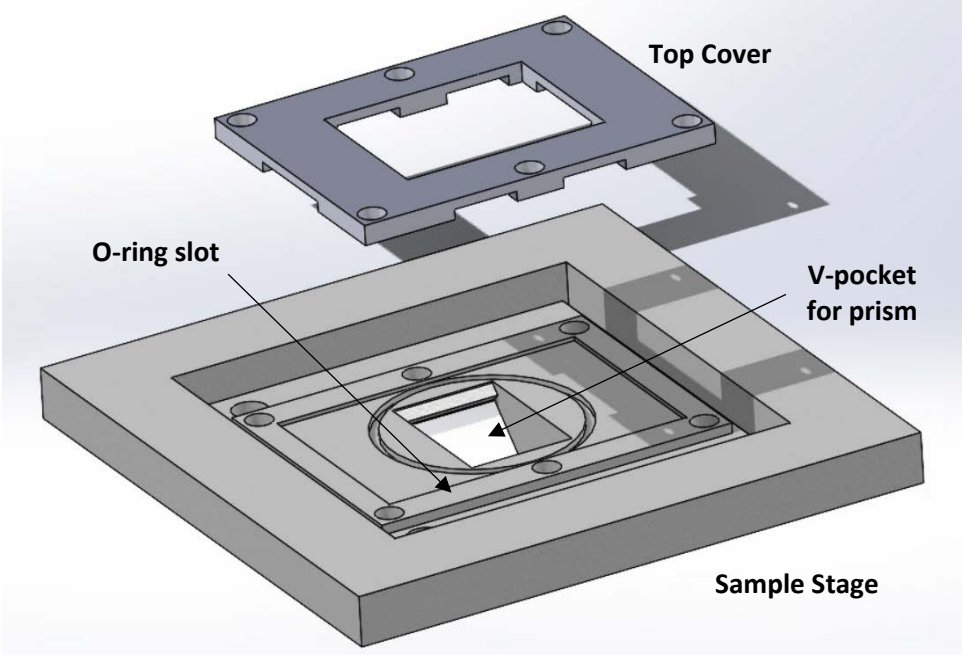

Fig. 6.5 A screenshot presenting an angled view (as seen from the top) of the CAD assembly model featuring a sample stage and a top cover. An O-ring is positioned in the slot shown to prevent water leakage into the prism surfaces.

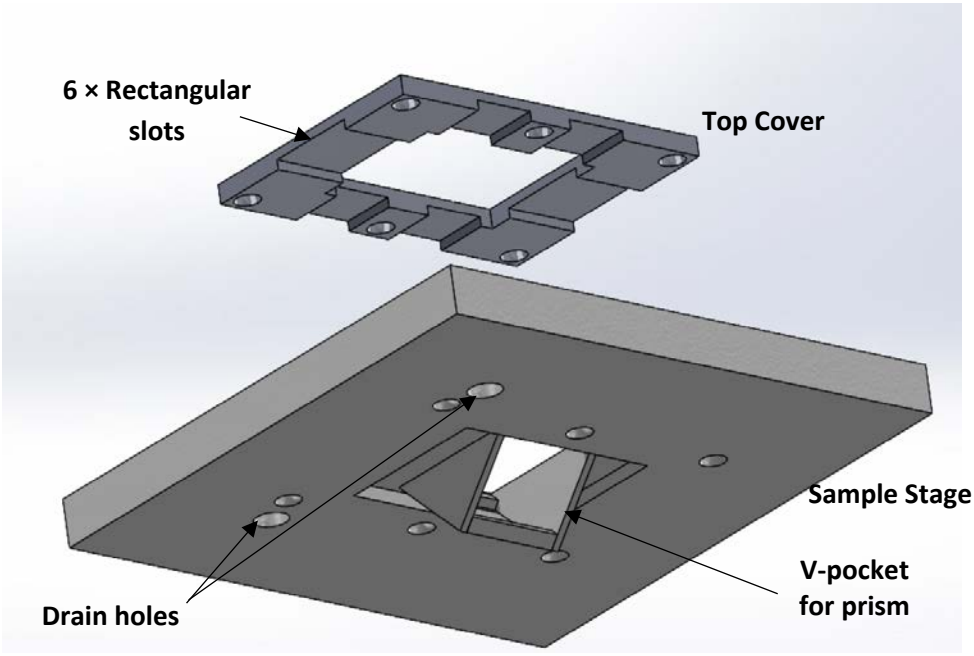

Fig. 6.6 A screenshot presenting an angled view (as seen from the bottom) of the CAD assembly model featuring a sample stage and a top cover. A V-shaped pocket is modeled and designed to house the glass prism fully. Drain holes (in the sample stage) and rectangular slots (in top cover) are provided to prevent water stagnation in the sample stage.

A polished mirror positioned at an inclination angle of *22.5º* reflects the collimated light from a LED light source (ILA GmBh 5150) to strike the glass prism. Another polished mirror (inclination angle ~ *157.5º*) directs the total internally reflected light rays from the prism towards a long working-distance microscope (K2 Distamax with CF2 objective lens) coupled to a high-speed digital camera (Photron Mini AX200). The high-speed camera operates at *4000 frames/sec* with a shutter speed of *1/20000 seconds* to capture *1024* × *1024 pixel* images.

6.3 Image Analysis

6.3.1 Calibration

A chrome mask fabricated in the Minnesota nano center was used as a benchmark for the calibration process. Image of the chrome mask (see fig. 6.7 (b)) was captured using a calibrated optical microscope, and the size of the microscale features were identified (Diameter, $D = 60\ \mu m$; Center-to-center distance, $P = 250\ \mu m$).

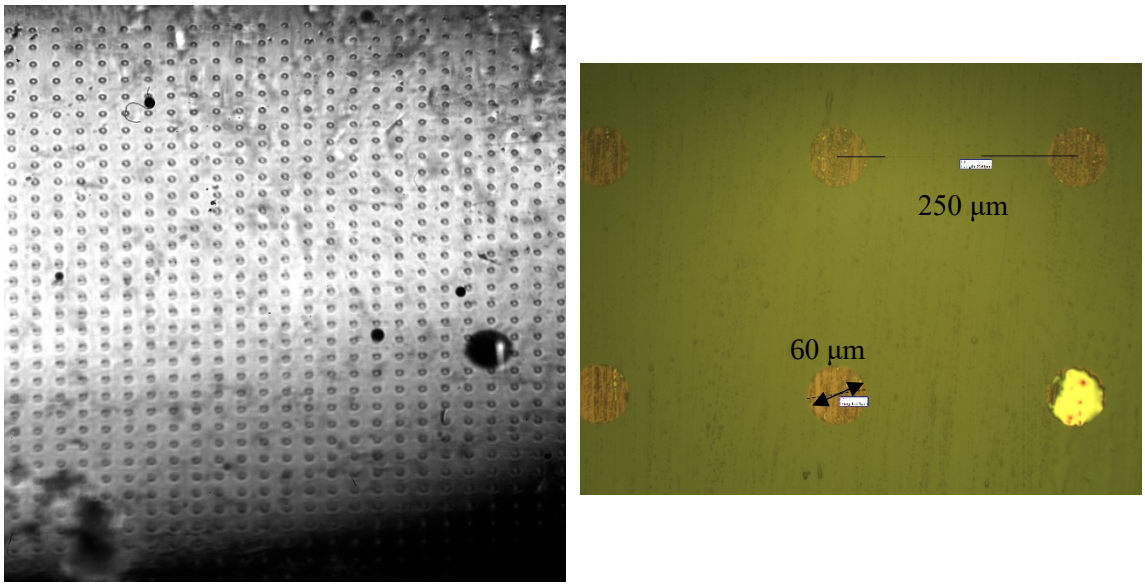

(a) *(b)*

Fig 6.7 Image of a chrome mask captured using – (a) the TIR setup (b) a calibrated optical microscope featuring microscale circular patterns with diameter, *D = 60 µm* and pitch, *P = 250 µm*

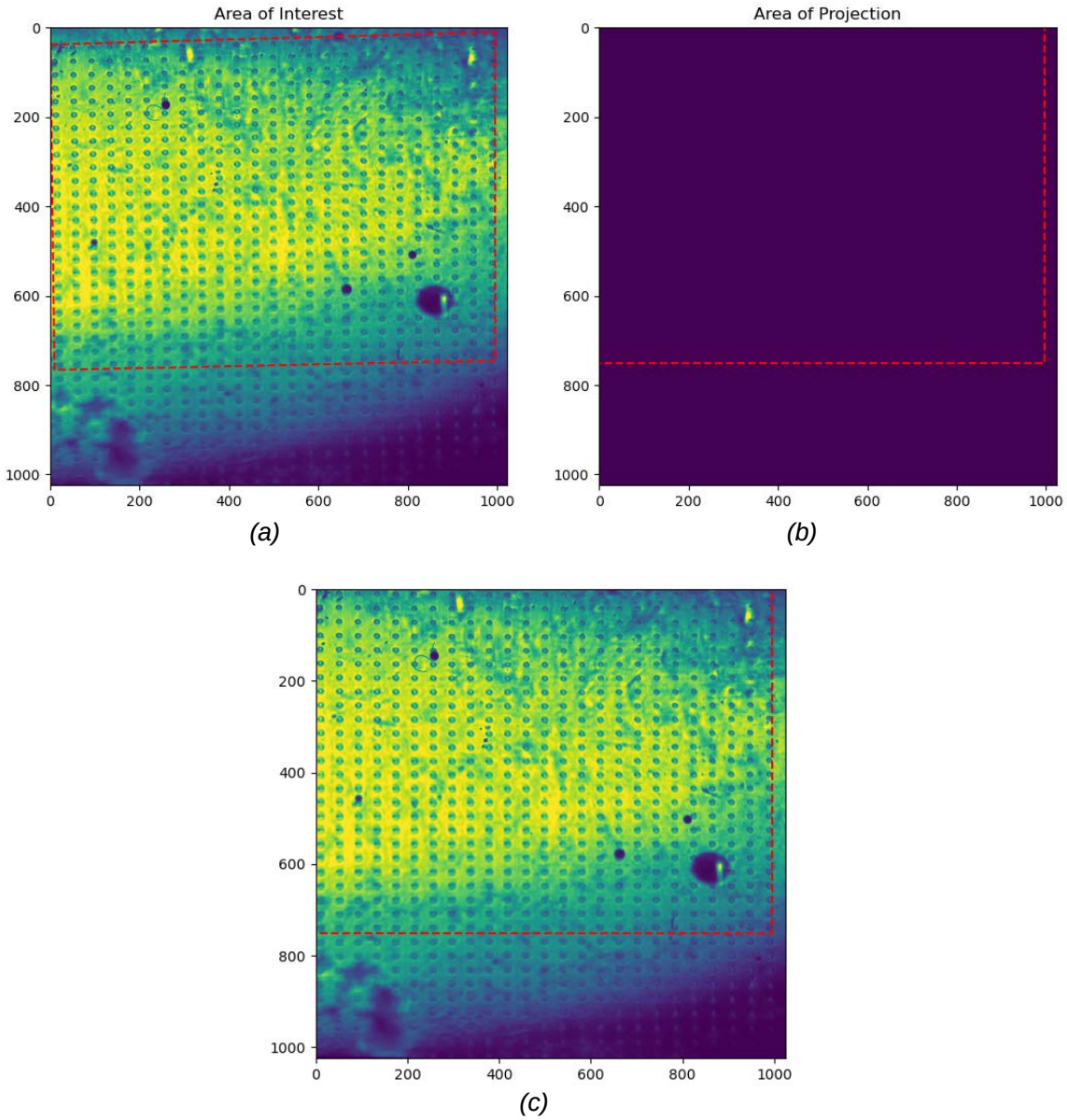

Fig 6.8 A perspective correction algorithm was used for image resurrection. (a) user-defined area of interest (b) the algorithm estimates the projected area and (c) maps the raw image into the final processed image.

Next, a grayscale image (see fig. 6.7 (a)) of the same chrome mask was taken using the long-distance microscope and high-speed camera combination. Clearly, the grayscale image looks distorted, and a perspective correction is needed to gauge the actual dimensions of the circular features. Thus, to correct for distortion, a Python program with a standard perspective correction algorithm was used to process and project the true image

(refer to fig. 6.8). After perspective correction, the aspect ratio of the circular objects was found to be within *0.97 – 1.0*.

6.3.2 Image processing using ImageJ

To extract quantitative information about the contact-line parameters, ImageJ software was used. ImageJ is a Java-based open-source image processing program used for processing and analyzing scientific images. High-speed grayscale images from the camera were batch-processed using an ImageJ macro written for this specific purpose. To distinguish and identify the region of interest (i.e., wetted area which looks darker in the captured images), a threshold must be set based on the image's grayscale value (i.e., *0 to 256*) such that wetted (darker) regions can be demarcated from the non-wetted regions (brighter). To implement this algorithm, the "AutoThreshold" function was used.

The automatic thresholding function is an iterative procedure based on the isodata algorithm. Briefly, the procedure extracts objects from its background by implementing threshold selection, provided the object has a different average gray level from that of its background. Consequently, the effect of thresholding will produce a black object with a white background or vice versa. Selecting an appropriate threshold is often challenging. The automatic thresholding function (available as the "AutoThreshold" function in ImageJ) is a technique whereby an optimum threshold may be chosen automatically due to an iterative process. In general, successive iterations provide cleaner extractions of the object region increasingly.

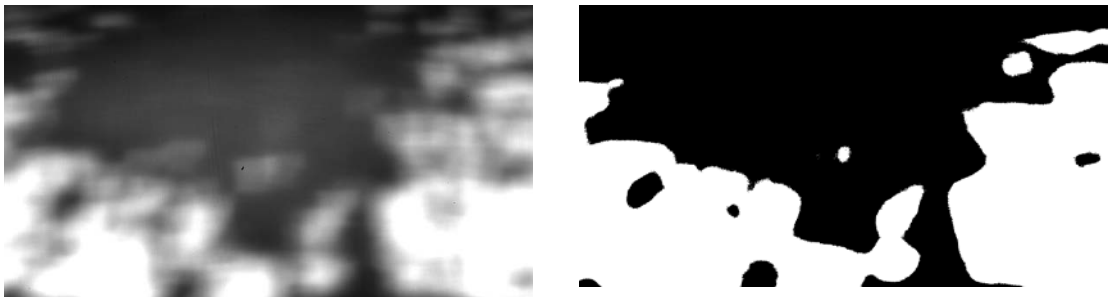

(a) *(b)*

Fig. 6.9 (a) Grayscale image obtained from the TIRM experiments for plain surface operating at applied power value of *210 W*. Here, the darker and brighter patches correspond to the wetted and non-wetted regions. (b) Black and white image after thresholding in ImageJ.

6.4 Results and Discussion

Results are obtained with the counterflow spray nozzle oriented normally to the sapphire substrate. The nozzle orifice was held at the height of *40 mm* from the surface such that the entire chip was covered by the spray. The water flow rate through the nozzle was set at *30 ml/min* operating at a pressure of *300 kPa*, and the corresponding *ALR* was *0.57*.

Sample images of the wetted surface using the TIRM technique are shown in Fig. 6.9. Similarly, images were obtained for two surfaces – Plain and rough (*10 μm*) while operated at various heat fluxes. The high-speed camera was set to record 4000 frames per second. However, due to immersion oil evaporation at high heat fluxes and data transfer from camera memory to a hard disk drive, only the first 1000 images were transferred and stored. These images were batch-processed using ImageJ, and the contact-line parameters such as wetted-area fraction and contact-line perimeter (CLP) per unit area were obtained for each image. The wetted-area fraction and the CLP per unit area are plotted against the applied heat flux in figures 6.10 and 6.11, respectively.

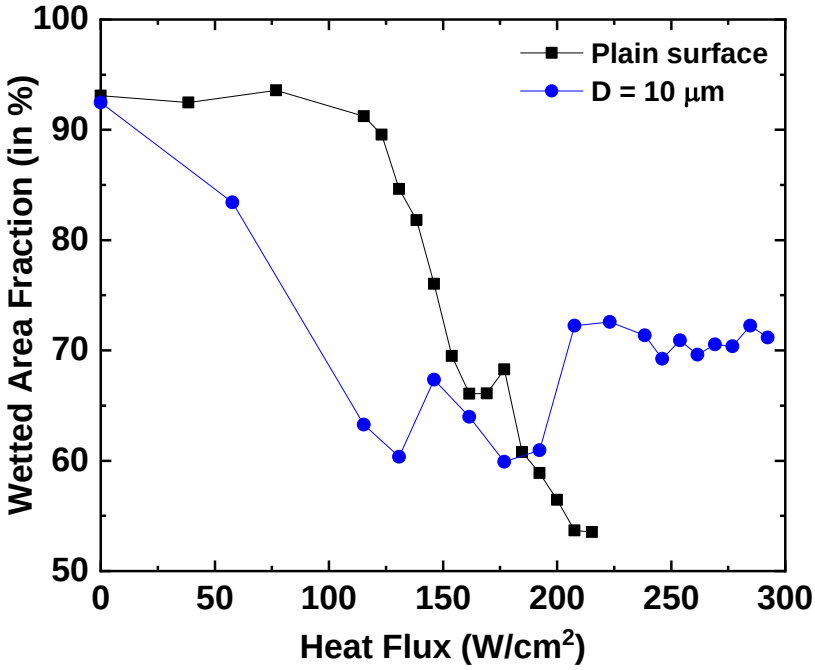

Fig. 6.10 Plot showing the variation of wetted-area fraction with increments in heat flux. The black squares line plot corresponds to the plain surface measurements and the blue dots line plot to the measurements done for *10 μm* pillar size.

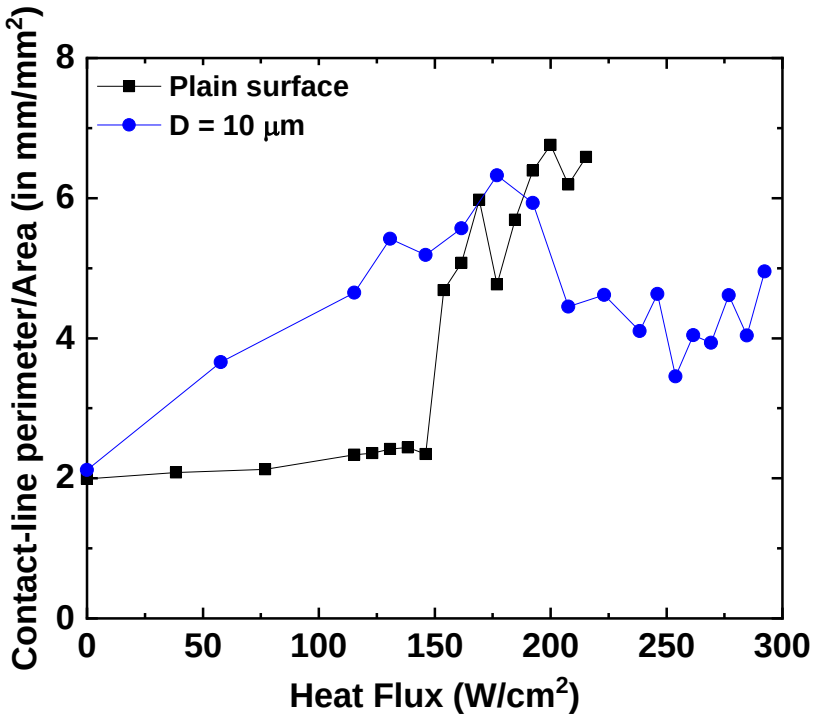

Fig. 6.11 Plot showing the variation of contact-line perimeter per unit area with increments in heat flux. Black squares line plot corresponds to the plain surface measurements and the blue dots line plot to the measurements done for *10 μm* pillar size.

The wetted-area fraction almost remains the flat for the plain surface until a heat flux value of *~125 W/cm^2*. Beyond that, there is a steep fall in the wetted area, marking the onset of a two-phase heat transfer regime. At *CHF*, the wetted-area fraction reaches close to 50%. Horacek et al. [5], [85] reported similar behavior for plain surfaces using TIR measurements.

On the other hand, for the *10-μm* surface, the wetted-area fraction plummets steeply at low heat fluxes. Increased wettability due to capillary action and instantaneous evaporation could be a possible reason for such behavior. Interestingly, starting from a heat flux value of *~200 W/cm^2*, the wetted area keeps fluctuating around an average value of *70%* and delays the *CHF* further as compared to the plain surface. This action clearly, showcases the ability of the textured surfaces to wet and re-wet the dry spots adequately and frequently enough such that intense evaporation is sustained at the microscale contact-line region; thereby, delaying the *CHF*.

At low heat fluxes, the *CLP* per unit area almost stays constant for plain surface and then, increases two-fold at *~150 W/cm^2* and proceed to increase non-linearly thereafter. Interestingly, the trend seen in the contact-line perimeter curves share a similar insight as that of a cooling curve. Meanwhile, the surfaces with *10 μm* show a linear trend in the single-phase regime with a steeper slope and decreases slightly at *~160 W/cm^2* and keeps fluctuating around an average *CLP* of *~4.75* until CHF. The difference in the *CLP* trends between plain surface and *10-μm* surface supports the enhancement of in-plane capillary suction flows (despite the pillar height being low) and bolsters the argument that contact-line evaporation plays a dominant role in the two-phase regime.

To comprehend this phenomenon further, the time-series data of the wetted area fraction obtained from the high-speed images were plotted for the plain surface (figs. 6.12 (a-p)) and the *10-μm* surface (figs. 6.13 (a-r)) for all the applied power values tested. At low heat fluxes, the surface was almost entirely wet by water. This physically signifies that the re-wetting time scale (which tends to re-wet the dry-spots) is much less compared to the heating/evaporation time scale (which creates dry-spots through phase change). Surface perturbation due to convective film instabilities caused by compressed air or impacting droplets might be a reason why dry spots were observed at low applied power. Nevertheless, these dry spots were typically re-wet in subsequent frames of the image set.

For the plain surface, as the system approaches two-phase regime (*P ~ 200 W*), the frequency of occurrence and the size of the dry spots were found to be increasing with increments in applied power. At *P = 280 W (@CHF*), the wetted area fraction undergoes a smooth periodic oscillation between 0% to 100%, meaning the evaporative time scales have reduced to an extent where it is equivalent to re-wetting time scale of the surface. A similar trend can be seen for the *10-μm* surface too until an applied power value of *250 W*. Beyond this value, the wetted area fraction oscillates between *40% and 100%* shifting the mean value from *50% - 60%* to more than *70%*. Such increments in the wetted area fraction can be only attributed to the activation of wicking capability of the micropillars; thereby, promoting more capillary suction flows to quench the incipient dry spots. This wicking action is persisting until the *CHF* (*@ P = 380 W*). Hence, from the comparison of the wetted-area time-series data obtained for plain and *10-μm* surface; we show that evaporation at the contact-lines is predominant in the two-phase regime. Enhanced

wicking/capillary action using *10-μm* surface showcases the significance of creating more contact-lines to promote evaporation and thus, more heat flux removal at the chip scale.

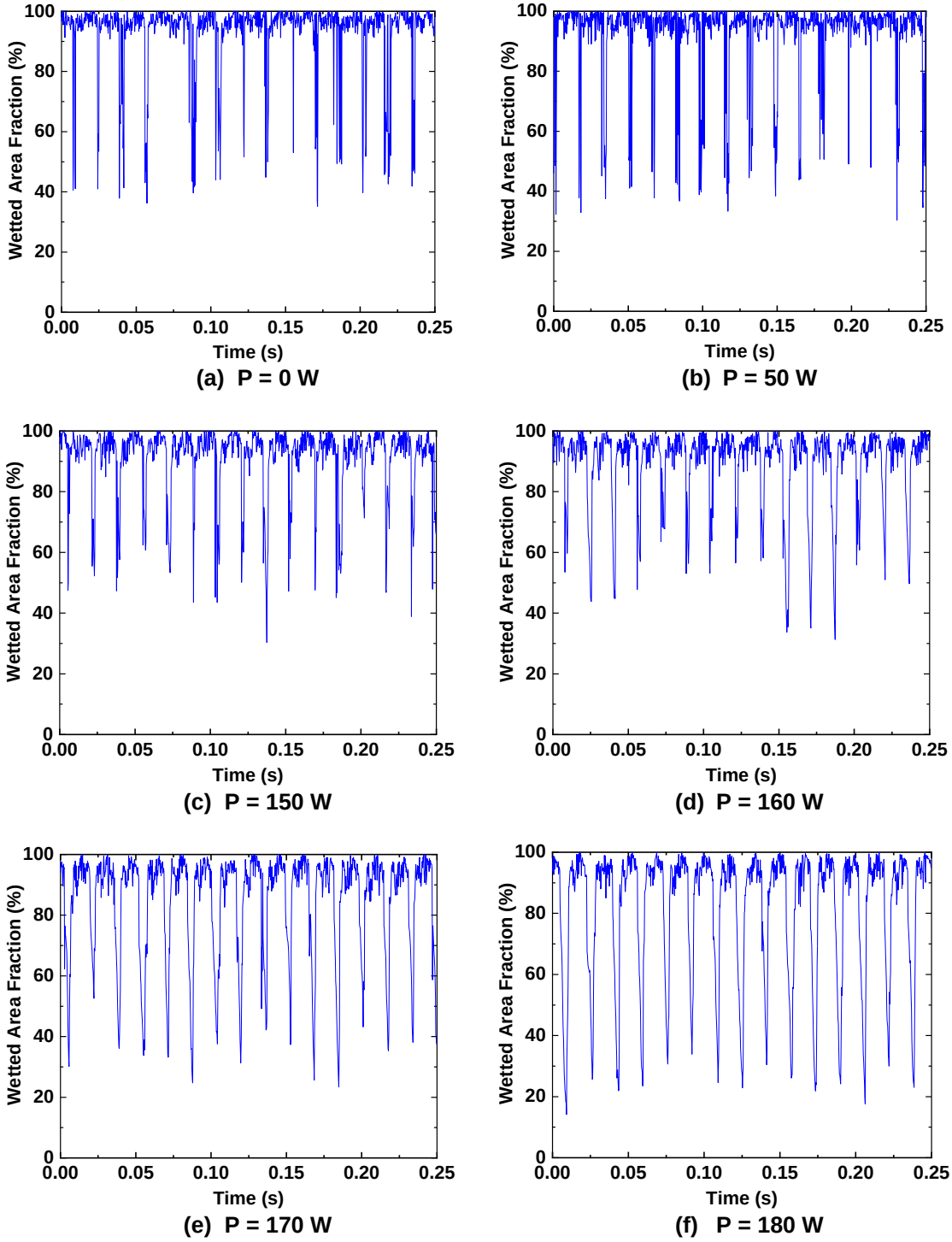

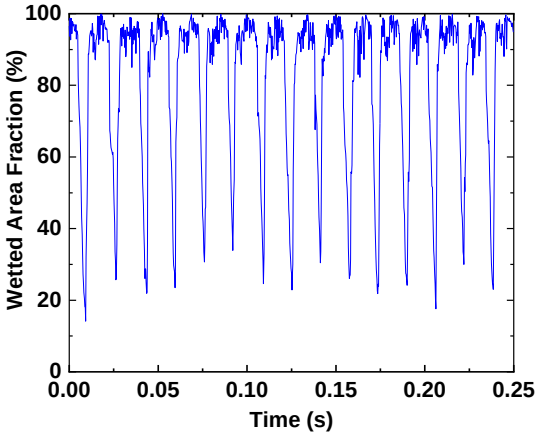

(g) P = 190 W

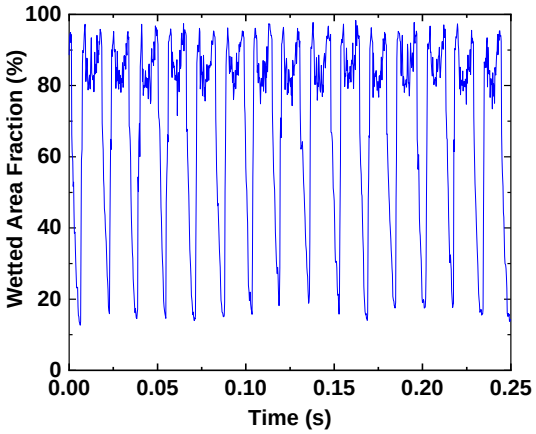

(h) P = 200 W

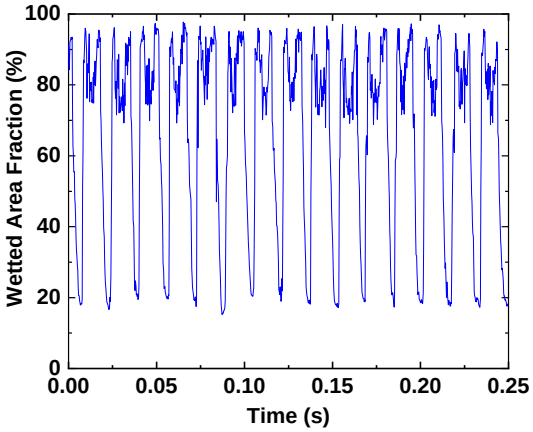

(i) P = 210 W

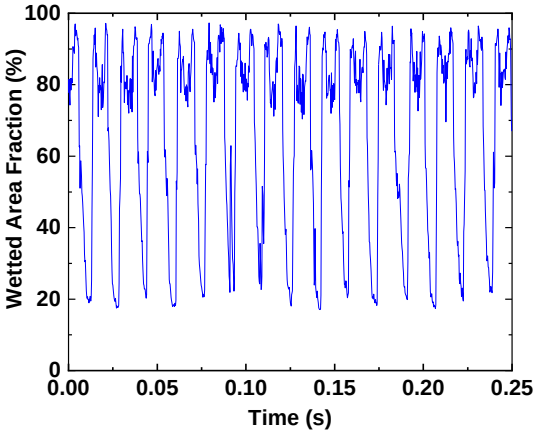

(j) P = 220 W

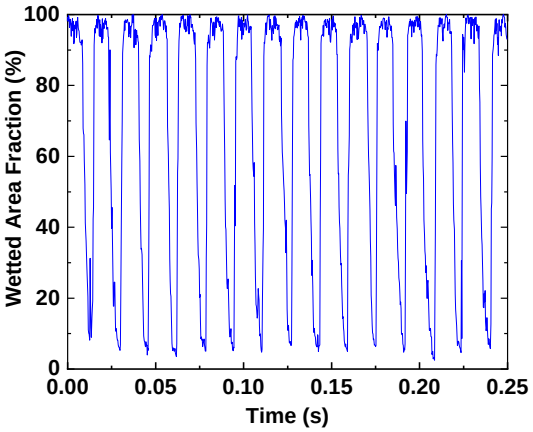

(k) P = 230 W

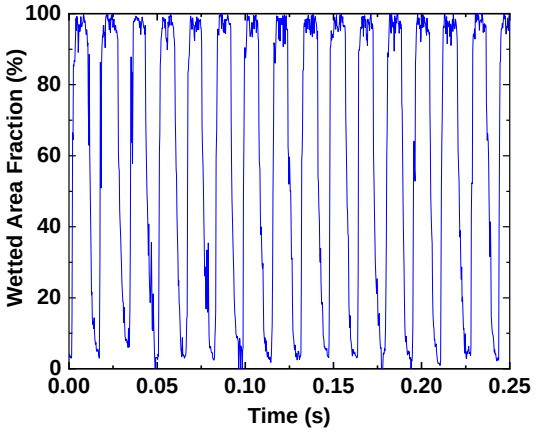

(l) P = 240 W

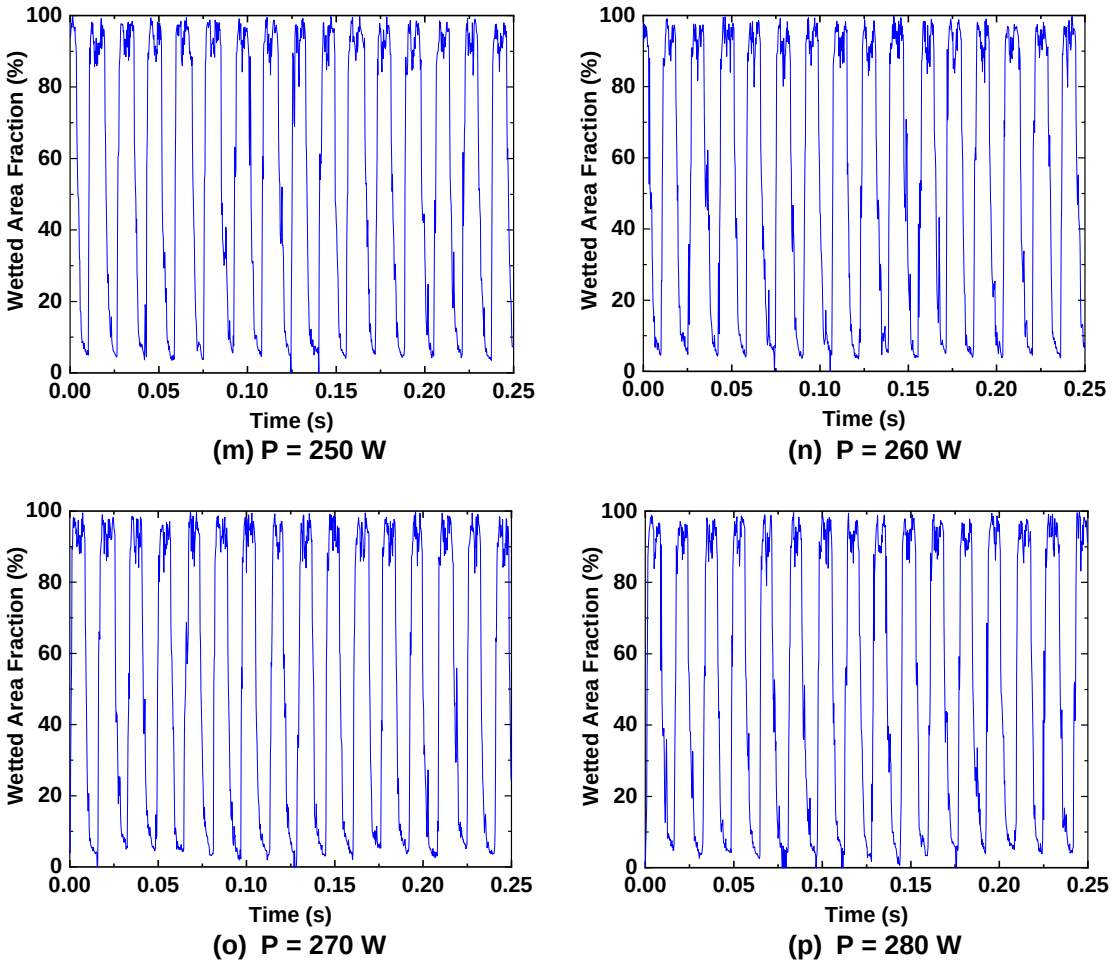

Fig. 6.12 (a) – (p) Time-series data of the wetted-area fraction obtained from TIRM experiments on pillar surface plotted for all the applied powers (*P = 0, 50, 150, 160, 170, 180, 190, 200, 210, 220, 230, 240, 250, 260, 270, and 280 W).* To obtain the heat flux values, the applied powers are divided by the heater area (*A = 1.3 cm^2*). CHF occurred at a heat flux value of ~ *215.38 W/cm^2*.

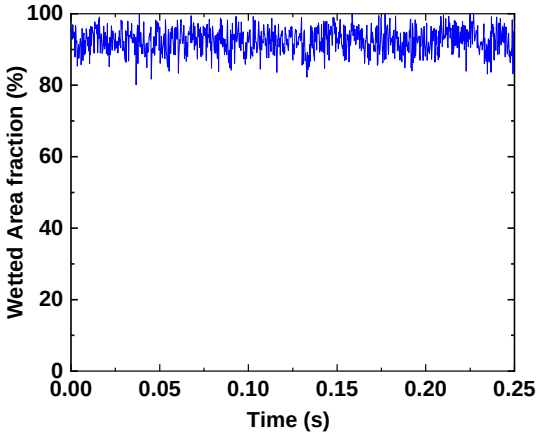

(a) P = 0 W

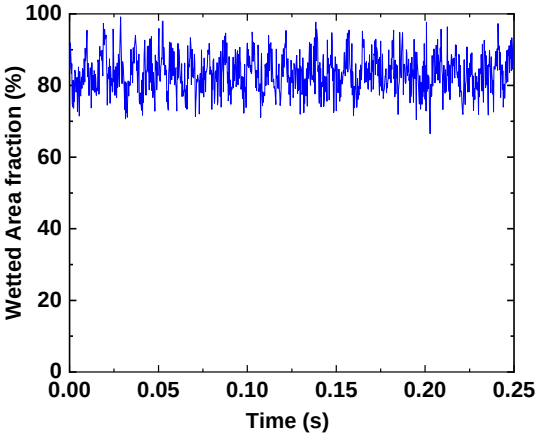

(b) P = 75 W

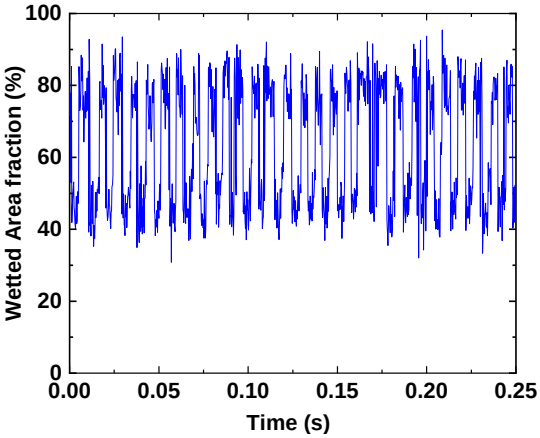

(c) P = 150 W

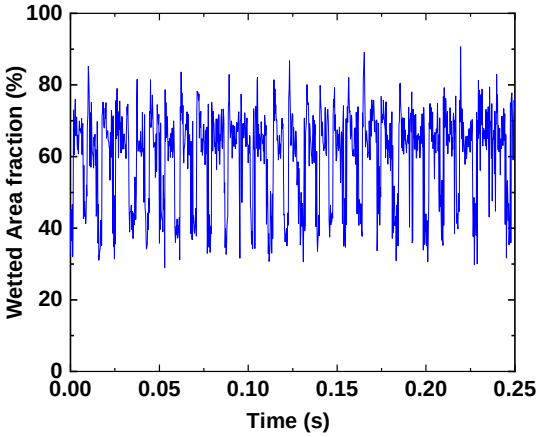

(d) P = 170 W

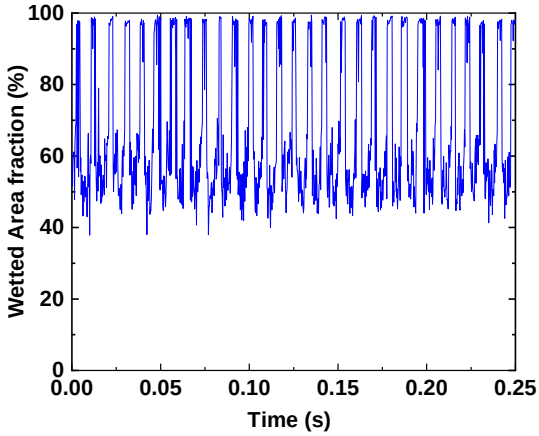

(e) P = 190 W

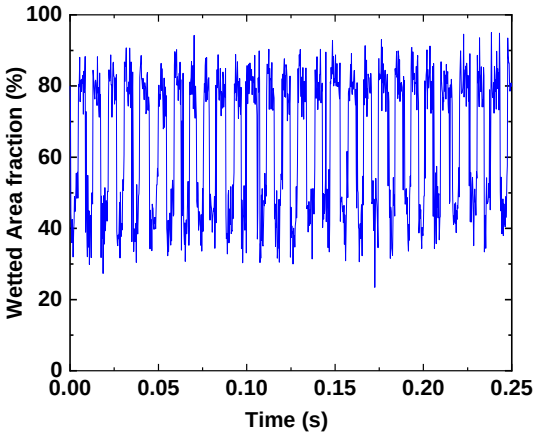

(f) P = 210 W

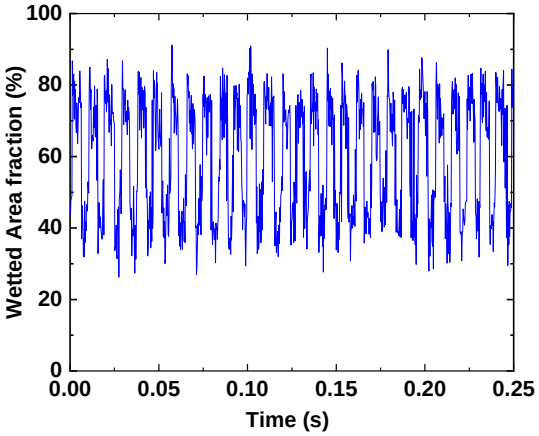

(g) P = 230 W

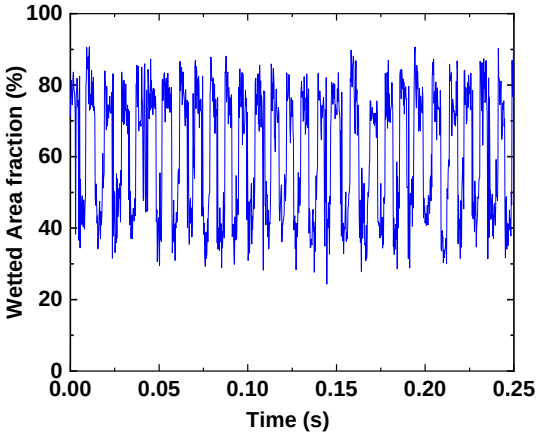

(h) P = 250 W

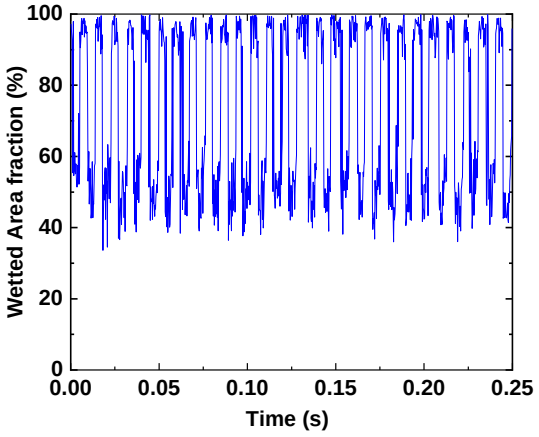

(i) P = 270 W

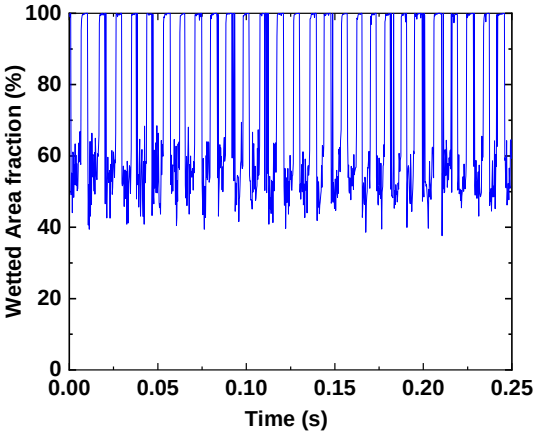

(j) P = 290 W

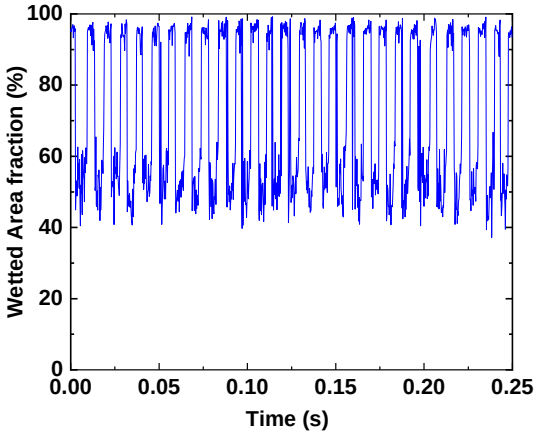

(k) P = 310 W

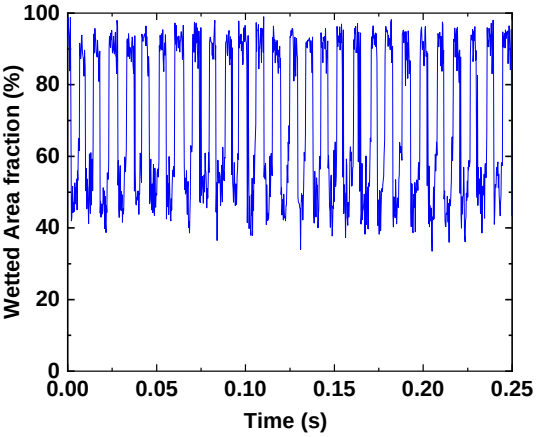

(l) P = 320 W

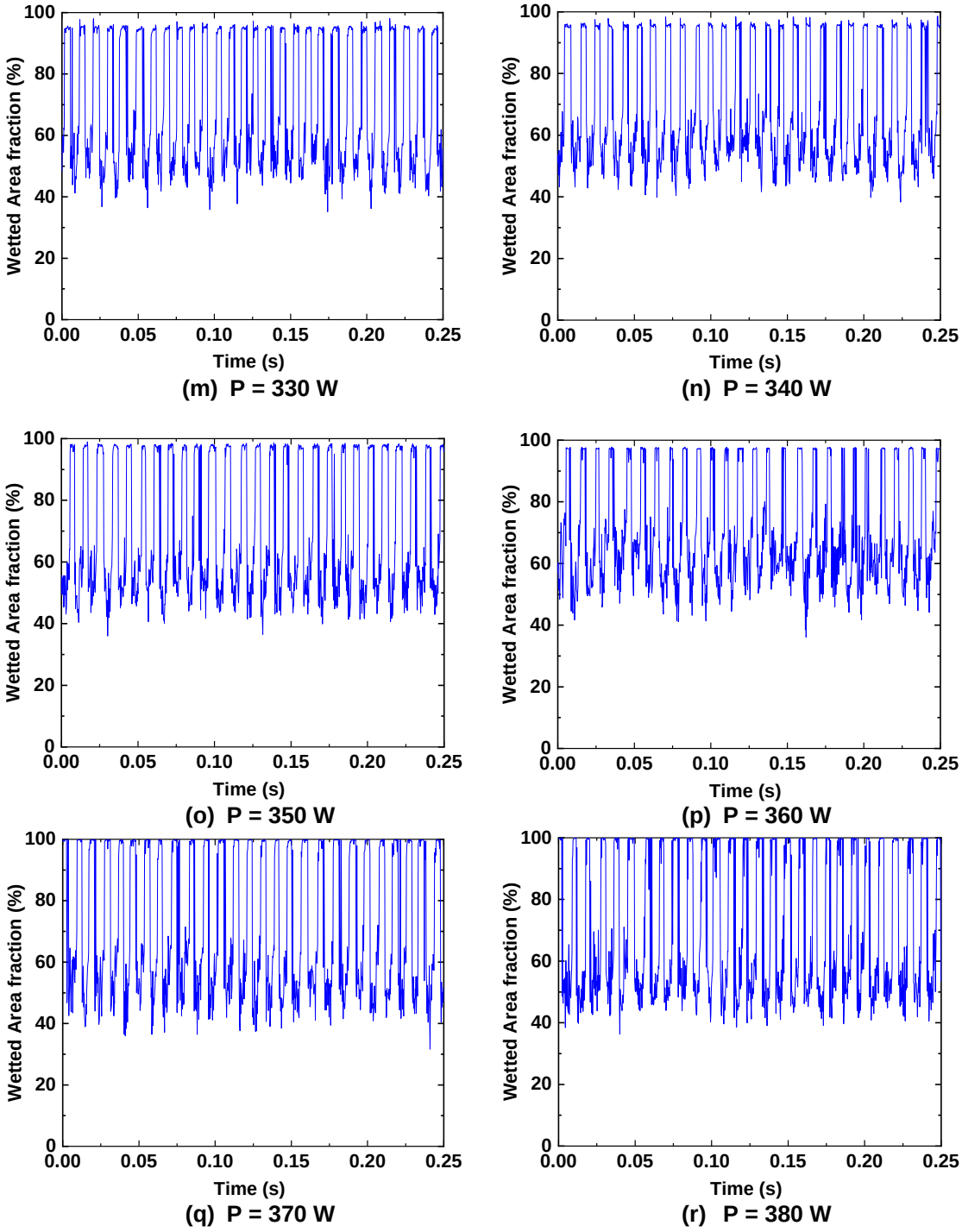

Fig. 6.13 (a) – (r) Time-series data of the wetted-area fraction obtained from TIRM experiments on 10-µm pillared surface plotted for all the applied powers (*P = 0, 75, 150, 170, 190, 210, 230, 250, 270, 290, 310, 320, 330, 340, 350, 360, 370, 380 W*). To obtain the heat flux values, the applied powers are divided by the heater area (*A = 1.3 cm^2*). CHF occurred at a heat flux value of ~ *292.31 W/cm^2*.

Based on the TIRM results obtained for the plain and 10-μm surface, it is clear that the capillary action plays a vital role in rewetting the dry spots and delaying the CHF. Hence we propose that when the heating time scale of the solid substrate as it approaches CHF is equivalent to the liquid imbibition time scale, CHF occurs. For the textured surfaces, the micropillars enhance the capillary action through the process of liquid imbibition. The liquid imbibition rate is governed by a balance between the capillary pressure developed across the advancing menisci and the viscous pressure drop that resists the liquid imbibition flow [79]. Capillary pressure is the additional pressure developed across a curved liquid-vapor interface due to surface tension. Due to the non-uniformities in the curvature of the advancing menisci (both spatially and temporally), a work-energy balance approach is used to get an approximate expression for the capillary pressure. Work done by the capillary pressure (P_c) to move a differential volume, δV, is given by

$$\delta W = P_c * \delta V \tag{6.1}$$

By the energy conservation principle,

$$\delta W + \delta E = 0 \tag{6.2}$$

$$P_c = \frac{-\delta E}{\delta V} = -\frac{\Delta E}{\Delta V} \tag{6.3}$$

In this case, the differential volume is the volume of wetted liquid inside a unit cell,

$$\Delta V = h[(w+p)^2 - w^2] \tag{6.4}$$

The change in the surface energy within the unit cell due to capillary wetting is the summation of the loss of solid-vapor interfacial energy ($\Delta E_1 = -[(w+p)^2 - w^2 + 4wh]\gamma_{sv}$) plus the energy added to the creation of new solid-liquid ($\Delta E_2 =$

$[(w+p)^2 - w^2 + 4wh]\gamma_{sl})$ and liquid-vapor $(\Delta E_3 = [(w+p)^2 - w^2]\gamma_{lv})$ interfaces. Therefore, ΔE is given by

$$\Delta E = [p(2w+p) + 4wh](\gamma_{sl} - \gamma_{sv}) + p(2w+p)\gamma_{lv} \tag{6.5}$$

Using Laplace equation, we can write

$$\gamma_{sl} - \gamma_{sv} = -\gamma_{lv} cos\theta \tag{6.6}$$

Where, θ is the apparent contact-angle. Substituting equations 6.4 and 6.6 in 6.3, we get,

$$P_c = -\frac{\Delta E}{\Delta V} = \gamma_{lv}\left[\frac{4w}{p(2w+p)} cos\theta - \frac{1}{h}(1 - cos\theta)\right] \tag{6.7}$$

Neglecting the inertial forces, the viscous pressure drop through the array of micropillars is given by

$$\nabla P_v = \mu \nabla^2 U \tag{6.8}$$

For larger spacing (i.e., $p > w$), the pressure gradient can be obtained by treating the liquid imbibition flow as flow over a flat plate with vertical length scale to be the pillar height and can be expressed as,

$$\nabla P_{v1} \sim C_1 \frac{\mu U_m}{h^2} \tag{6.9}$$

For smaller spacing (i.e., $w > p$), the imbibition flow can be modeled as flow between two parallel plates with the pressure gradient scaling with the pillar height,

$$\nabla P_{v2} \sim C_2 \frac{\mu U_m}{p^2} \tag{6.10}$$

Where C_1 and C_2 are integration constants. For intermediate pillar spacings (i.e., $w \sim p$), combining the results from equations 6.9 and 6.10 while scaling the P_{v2} with $w^2/(w+p)^2$ to account for the fractional contribution and the resultant pressure gradient is given by,

$$\nabla P_v \sim \mu U_m \left[\frac{C_1}{h^2} + \frac{C_2 w^2}{p^2(w+p)^2}\right] \tag{6.11}$$

Hence, the viscous pressure drop experienced by the liquid flow through the micropillar arrays can be expressed as,

$$P_v \sim \mu U_m L \left[\frac{C_1}{h^2} + \frac{C_2 w^2}{p^2(w+p)^2}\right] \tag{6.12}$$

Where L is the imbibition length. Equating the viscous pressure drop and the capillary pressure drop to obtain the imbibition time scale,

$$\tau_i \sim \frac{\mu L^2}{p_c} \left[\frac{C_1}{h^2} + \frac{C_2 w^2}{p^2(w+p)^2}\right] \tag{6.13}$$

For square micropillars, C_1 and C_2 were found to be 3 and 24, respectively. Assuming negligible temperature gradients along the substrate thickness and no lateral conduction across the surface, the heating timescale of a dry spot can be modeled using the lumped capacitance thermal model.

$$\tau_h \sim \frac{\rho_s C_s t_s (T_{crit} - T_0)}{q"} \tag{6.14}$$

Where ρ_s is the density, C_s is the specific heat capacity, t_s is the thickness of the substrate with $(T_{crit} - T_0)$ as the instantaneous temperature jump experienced during CHF (typically, found to be 10 ºC – 15 ºC).

Figure 6.14 shows the comparison between the two competing time scales (i.e., the heating time scale and the liquid imbibition scale) at high heat flux values for the 10-μm surface. As the heating time scale approaches the liquid imbibition scale, the substrate approaches CHF. Evidently, this behavior can be seen in the time-series data obtained for the 10-μm surface at higher heat flux values.

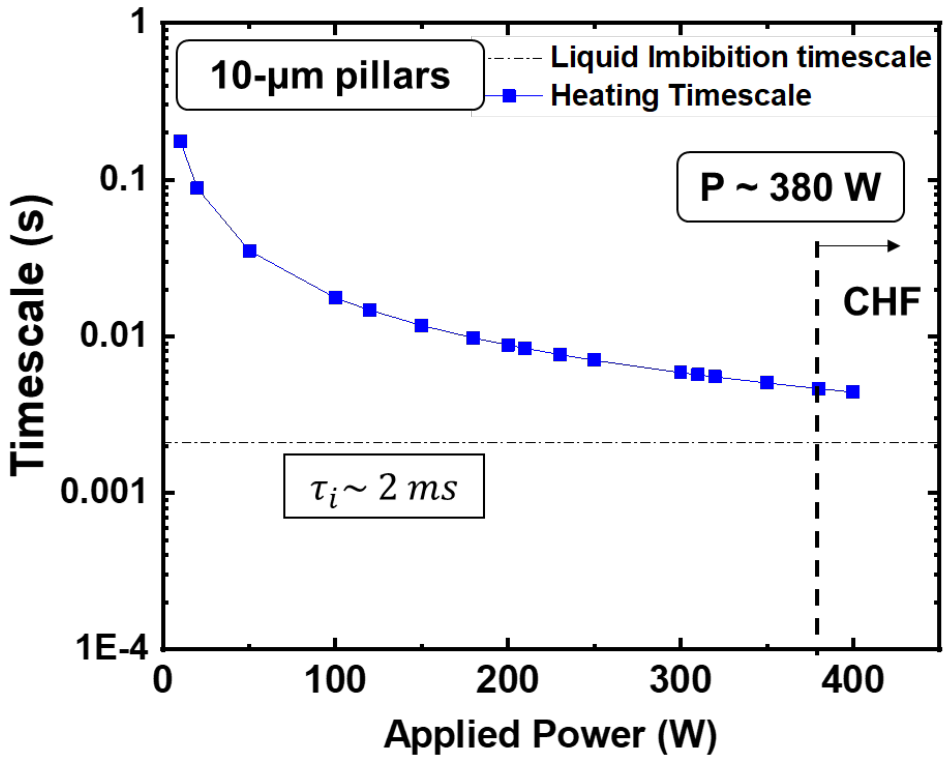

Fig. 6.14 Comparison of the substrate heating time scale with respect to the liquid imbibition time scale (~ 0.002 s) at various applied powers. Both the time scales were seen to converge as the applied power value approaches the crisis point (CHF)

6.5 Summary

The Total Internal Reflectance Microscopy (TIRM) technique was used to perform an in-situ visualization on the solid/liquid/vapor interface. For the first time in the history of TIRM/spray cooling literature, we showcased the possibility of high temperature TIRM experiments using water (estimated temperature ~ *150 ºC*). The effects of varying the roughness parameters on the contact-line parameters were investigated. Key outcomes and learnings of this study are as follows.

- For the plain surface, the wetted area fraction approaches *50%* at *CHF* as seen by Horacek et al. [5], [85]. The trends in contact-line perimeter per unit area vs. heat flux resembles the cooling curves obtained from the heat transfer experiments using silicon wafers.
- For the *10-μm* surface, the wetted area fraction approaches *60%* at an intermittent value of applied power and then grows to *70%* and above sustaining the evaporation process for comparatively higher values of power. The Contact Line Perimeter per unit area curves show sudden drops at a power value of $P = 250\ W$ and fluctuates over an average value of $4.75\ mm/mm^2$ until CHF is reached (@ $P = 380\ W$). CHF increments up to *35%* were observed for the low-aspect ratio, *10-μm* surface.
- The time-series data plots of the wetted-area fraction obtained for plain and *10-μm* surfaces reveal the superior wicking ability of microtextured surfaces, especially in the two-phase regime. These results strengthen the argument that contact-line evaporation is the predominant heat transfer mechanism in the two-phase regime of the spray cooling process.

Chapter 7

Conclusion and Future Works

7.1 Thesis Synopsis

Spray cooling is a versatile technology that can address future cooling demands, by removing very high heat fluxes using low fluid inventory while maintaining optimum temperature levels. The conventional cooling systems rely on the low efficiency air handling units and single-phase cooling. With the future demand for cooling in the order of 10^2 *to* 10^3 *W/cm*^{2}, the implementation of novel cooling techniques such as spray cooling is inevitable.

Given the numerous challenges associated with characterizing the spray cooling performance, certain parameters such as surface roughness, and water/air flow rates were varied systematically to conduct a parametric study covering roughness scales ranging from *50 μm to 0.8 μm*. For heat transfer experiments, Silicon substrates were used for fabricating the samples using standard and advanced lithography procedures coupled with dry etching. Each sample was tested using a air-assisted liquid spray generated by a counterflow nozzle operating at a water flow rate of *30 ml/min* corresponding to air-to-liquid ratio of *0.57* (standard flow setting). Three calibrated T-type thermocouples were used to obtain the temperature data.

For a 20-*μm* sample with a pillar height of 20 *μm*, experiments were carried out for three air flow rates (*= 6.7, 13.7, and 22.6 slpm*) with a constant water flow rate of *30 ml/min*

and for three water flow rates (= *30, 60, and 82 ml/min*) with a constant air flow rate of *13.7 slpm*. Important results and concluding remarks obtained from these experiments are enumerated below:

- CHF maxima exist for all the families of textured surfaces tested. Based on the results obtained and insights gained, surfaces with pillar diameter (*D*) ≈ pillar spacing (*P*) ≈ pillar height (*H*) is preferred. It is shown that *5-μm* and *10-μm* pillar arrays exhibited maximum spray cooling performance.
- Transition from Cassie–Baxter state to Wenzel state is critical for liquid penetration into the forest of micropillars. Surfaces with *2-μm* and *0.8-μm* pillar arrays exhibit inferior cooling performance due to low liquid penetration. This theory stands valid for surfaces with small pillar spacing, i.e., $P/D < 1$. In-plane Laplace pressures become important to ensure complete wetting. Hence, pillar-arrayed surfaces with $P/D > 1$ show diminishing results.
- Despite showing relatively low *CHF* values as compared to those of the *10-μm* and *5-μm* micropillar arrays, surfaces with *50-μm* and *20-μm* micropillar arrays recorded the highest heat transfer coefficients (*~20 W/cm^{2}K*). The availability of more floor area for menisci stretching during the wetting process and intense evaporation at the liquid-vapor interfacial area made these surfaces record higher HTC values.

High-speed images of the solid/liquid/vapor interface using TIR microscopy were obtained for plain and *10-μm* surfaces. Some of the key observations and learnings are listed below:

- CHF enhancements up to *35%* were observed for the low-aspect ratio *10-μm* surface. For the plain surface, the wetted area fraction approaches *50%* at CHF. The trends corresponding to the contact-line perimeter per unit area vs. heat flux resembles the cooling curves obtained from the heat transfer experiments using silicon wafers.
- For the *10-μm* surface, the wetted area fraction approaches *60%* at an intermittent value of applied power and then, grows to *70%* and above and sustains the evaporation process for comparatively higher values of power. The CLP per unit area curves show sudden drop at a power value of $P = 250\ W$ with rising heat flux and fluctuates over an average value of $4.75\ mm/mm^2$, until *CHF* is reached (@ $P = 380\ W$).
- The time-series data plots of the wetted-area fraction obtained for plain and *10-μm* surfaces reveal the superior wicking ability of the microtextured surfaces, especially in the two-phase regime. These results strengthen the argument that contact-line evaporation is the predominant heat transfer mechanism in the two-phase regime of the spray cooling process.

7.2 Future Works

Guidelines for future work are as follows:

- *50-μm and 20-μm* micropillar arrays recorded the highest heat transfer coefficients (*~20* W/cm^2K) while *10-μm* and *5-μm* micropillar arrays registered relatively higher CHF values. Thus, a hierarchical microstructure can be constructed and tested for various possible configurations. These hierarchical microstructures can possibly give the optimum performance values in terms of *CHF*, *HTC*, and cooling efficiency.

- More Total Internal Reflectance Microscopy experiments with surfaces containing various micropillar arrays would shed more light on the role of contact-line evaporation, in-plane capillary suction, and the evaporation time scale associated with the microtextured surfaces.

Bibliography

[1] J. L. Plawsky, M. Ojha, A. Chatterjee, and P. C. Wayner, “Review of the effects of surface topography, surface chemistry, and fluid physics on evaporation at the contact line,” *Chem. Eng. Commun.*, vol. 196, no. 5, pp. 658–696, 2009.

[2] J. Breitenbach, I. V. Roisman, and C. Tropea, “From drop impact physics to spray cooling models: a critical review,” *Exp. Fluids*, vol. 59, no. 3, pp. 1–21, 2018.

[3] J. Kim, “Spray cooling heat transfer : The state of the art,” vol. 28, pp. 753–767, 2007.

[4] T. A. Shedd, “Next generation spray cooling: High heat flux management in compact spaces,” *Heat Transf. Eng.*, vol. 28, no. 2, pp. 87–92, 2007.

[5] B. Horacek, K. T. Kiger, and J. Kim, “Single nozzle spray cooling heat transfer mechanisms,” *Int. J. Heat Mass Transf.*, vol. 48, no. 8, pp. 1425–1438, 2005.

[6] Z. Su and J. A. Malen, “Heat Dissipation in GaN Based Power Electronics,” *ECS Trans.*, vol. 58, no. 4, pp. 343–349, 2013.

[7] B. N. Pushpakaran, A. S. Subburaj, and S. B. Bayne, “Commercial GaN-Based Power Electronic Systems: A Review,” *J. Electron. Mater.*, vol. 49, no. 11, pp. 6247–6262, 2020.

[8] M. S. Shur, “GaN based transistors for high power applications,” *Solid. State. Electron.*, vol. 42, no. 12, pp. 2131–2138, 1998.

[9] A. Bar-Cohen and P. Wang, “Thermal Management of On-Chip Hot Spot,” *J. Heat Transfer*, vol. 134, no. 5, p. 051017, 2012.

[10] I. W. Kuncoro, N. A. Pambudi, M. K. Biddinika, I. Widiastuti, M. Hijriawan, and K. M. Wibowo, “Immersion cooling as the next technology for data center cooling: A review,” *J. Phys. Conf. Ser.*, vol. 1402, no. 4, 2019.

[11] A. Faghri, “Heat Pipes: Review, Opportunities and Challenges,” *Front. Heat Pipes*, vol. 5, no. 1, 2014.

[12] S. G. Kandlikar, “High flux heat removal with microchannels - A roadmap of challenges and opportunities,” *Heat Transf. Eng.*, vol. 26, no. 8, pp. 5–14, 2005.

[13] V. Singhal, S. V. Garimella, and A. Raman, “Microscale pumping technologies for microchannel cooling systems,” *Appl. Mech. Rev.*, vol. 57, no. 1–6, pp. 191–221, 2004.

[14] N. Fathi, J. Kim, S. Jun, R. M. King, M. Amaya, and S. M. You, “Evaporative

Cooling Heat Transfer of Water From Hierarchically Porous Aluminum Coating," *Heat Transf. Eng.*, vol. 0, no. 0, pp. 1–12, 2017.

[15] B. Porumb, P. Ungureşan, L. F. Tutunaru, A. Şerban, and M. BĂlan, "A Review of Indirect Evaporative Cooling Technology," *Energy Procedia*, vol. 85, no. November 2015, pp. 461–471, 2016.

[16] S. G. Kandlikar and A. V. Bapat, "Evaluation of jet impingement, spray and microchannel chip cooling options for high heat flux removal," *Heat Transf. Eng.*, vol. 28, no. 11, pp. 911–923, 2007.

[17] M. A. Ebadian and C. X. Lin, "A Review of High-Heat-Flux Heat Removal Technologies," *J. Heat Transfer*, vol. 133, no. 11, p. 110801, 2011.

[18] R. Xu, G. Wang, and P. Jiang, "Spray Cooling on Enhanced Surfaces: A Review of the Progress and Mechanisms," *J. Electron. Packag. Trans. ASME*, vol. 144, no. 1, pp. 14–16, 2022.

[19] I. Mudawar, "Assessment of high-heat-flux thermal management schemes," *IEEE Trans. Components Packag. Technol.*, vol. 24, no. 2, pp. 122–141, 2001.

[20] A. Bar-Cohen, M. Arik, and M. Ohadi, "Direct liquid cooling of high flux micro and nano electronic components," *Proc. IEEE*, vol. 94, no. 8, pp. 1549–1570, 2006.

[21] E. Masanet, A. Shehabi, N. Lei, S. Smith, and J. Koomey, "Recalibrating global data center energy-use estimates," *Science (80-.).*, vol. 367, no. 6481, pp. 984–986, 2020.

[22] M. Dayarathna, Y. Wen, and R. Fan, "Data center energy consumption modeling: A survey," *IEEE Commun. Surv. Tutorials*, vol. 18, no. 1, pp. 732–794, 2016.

[23] G. Liang and I. Mudawar, "Review of spray cooling – Part 1: Single-phase and nucleate boiling regimes, and critical heat flux," *Int. J. Heat Mass Transf.*, vol. 115, no. June, pp. 1174–1205, 2017.

[24] W. L. Cheng, W. W. Zhang, H. Chen, and L. Hu, "Spray cooling and flash evaporation cooling: The current development and application," *Renew. Sustain. Energy Rev.*, vol. 55, pp. 614–628, 2016.

[25] J. D. Benther, J. D. Pelaez-Restrepo, C. Stanley, and G. Rosengarten, "Heat transfer during multiple droplet impingement and spray cooling: Review and prospects for enhanced surfaces," *Int. J. Heat Mass Transf.*, vol. 178, p. 121587, 2021.

[26] B. V. Derjaguin, "Modern state of the investigation of long-range surface forces," *Prog. Surf. Sci.*, vol. 40, no. 1–4, pp. 254–259, 1992.

[27] A. W. Adamson and A. P. Gast, *Physical Chemistry of Surfaces*, vol. 150. New York: Interscience publishers, 1967.

[28] A. Yarin, I. Roisman, and C. Tropea, *Collision phenomena in liquids and solids*. Cambridge University Press, Cambridge, 2017.

[29] S. Chandra and C. T. Avedisian, "On the collision of a droplet with a solid surface," *Proc. R. Soc. A Math. Phys. Eng. Sci.*, vol. 432, no. 1884, pp. 13–41, 1991.

[30] J. D. Bernardin, C. J. Stebbins, and I. Mudawar, "Effects of surface roughness on water droplet impact history and heat transfer regimes," *International Journal of Heat and Mass Transfer*, vol. 40, no. 1. pp. 73–78, 1996.

[31] J. D. Bernardin, C. J. Stebbins, and I. Mudawar, "Mapping of impact and heat transfer regimes of water drops impinging on a polished surface," *Int. J. Heat Mass Transf.*, vol. 40, no. 2, pp. 247–267, 1997.

[32] V. Bertola, "An impact regime map for water drops impacting on heated surfaces," *Int. J. Heat Mass Transf.*, vol. 85, pp. 430–437, 2015.

[33] M. Khavari, C. Sun, D. Lohse, and T. Tran, "Fingering patterns during droplet impact on heated surfaces," *Soft Matter*, vol. 11, no. 17, pp. 3298–3303, 2015.

[34] H. J. J. Staat, T. Tran, B. Geerdink, and G. Riboux, "Phase diagram for droplet impact on superheated surfaces," vol. 113, pp. 1–12, 2015.

[35] T. Tran, H. J. J. Staat, A. Prosperetti, C. Sun, and D. Lohse, "Drop impact on superheated surfaces," *Phys. Rev. Lett.*, vol. 108, no. 3, pp. 2–5, 2012.

[36] Y. Takata, M. Kohno, S. Hidaka, and E. S. R. Negeed, "High speed camera investigation of the impingement of single water droplets on oxidized high temperature surfaces," *Int. J. Therm. Sci.*, 2013.

[37] Y. Takata, E. S. R. Negeed, and M. Albeirutty, "Dynamic behavior of micrometric single water droplets impacting onto heated surfaces with TiO2 hydrophilic coating," *Int. J. Therm. Sci.*, 2014.

[38] J. Breitenbach, I. V. Roisman, and C. Tropea, "Heat transfer in the film boiling regime: Single drop impact and spray cooling," *Int. J. Heat Mass Transf.*, vol. 110, pp. 34–42, 2017.

[39] Y. Y. Hsu, "On the size range of Active Nucleation Cavities on a Heating Surface," *J. heat*, pp. 207–213, 1962.

[40] T. A. Shedd and A. G. Pautsch, "Spray impingement cooling with single- and multiple-nozzle arrays. Part II: Visualization and empirical models," *Int. J. Heat Mass Transf.*, vol. 48, no. 15, pp. 3176–3184, 2005.

[41] A. G. Pautsch and T. A. Shedd, “Spray impingement cooling with single- and multiple-nozzle arrays. Part I: Heat transfer data using FC-72,” *Int. J. Heat Mass Transf.*, vol. 48, no. 15, pp. 3167–3175, 2005.

[42] I. Mudawar *et al.*, “Optimizing and Predicting CHF in Spray Cooling of a Square Surface,” *J. Heat Transfer*, vol. 118, no. 3, p. 672, 1996.

[43] J. R. Rybicki and I. Mudawar, “Single-phase and two-phase cooling characteristics of upward-facing and downward-facing sprays,” *Int. J. Heat Mass Transf.*, vol. 49, no. 1–2, pp. 5–16, 2006.

[44] R. Zhao, W. Cheng, Q. Liu, and H. Fan, “Study on heat transfer performance of spray cooling: model and analysis,” *Heat Mass Transf.*, vol. 46, no. 8–9, pp. 821–829, 2010.

[45] D. P. Rini, R.-H. Chen, and L. C. Chow, “Bubble Behavior and Nucleate Boiling Heat Transfer in Saturated FC-72 Spray Cooling,” *J. Heat Transfer*, vol. 124, no. 1, p. 63, 2002.

[46] S. S. Hsieh, T. C. Fan, and H. H. Tsai, “Spray cooling characteristics of water and R-134a. Part I: Nucleate boiling,” *Int. J. Heat Mass Transf.*, vol. 47, no. 26, pp. 5703–5712, 2004.

[47] S. S. Hsieh, T. C. Fan, and H. H. Tsai, “Spray cooling characteristics of water and R-134a. Part II: Transient cooling,” *Int. J. Heat Mass Transf.*, vol. 47, no. 26, pp. 5713–5724, 2004.

[48] L. Lin and R. Ponnappan, “Heat transfer characteristics of spray cooling in a closed loop,” *Int. J. Heat Mass Transf.*, vol. 46, no. 20, pp. 3737–3746, 2003.

[49] M. Visaria and I. Mudawar, “Effects of high subcooling on two-phase spray cooling and critical heat flux,” *Int. J. Heat Mass Transf.*, vol. 51, no. 21–22, pp. 5269–5278, 2008.

[50] M. Visaria and I. Mudawar, “Application of Two-Phase Spray Cooling for Thermal Management of Electronic Devices,” *IEEE Trans. Components Packag. Technol.*, vol. 32, no. 4, pp. 784–793, 2009.

[51] H. Honda and J. J. Wei, “Enhanced boiling heat transfer from electronic components by use of surface microstructures,” *Exp. Therm. Fluid Sci.*, vol. 28, no. 2–3, pp. 159–169, 2004.

[52] C. Sodtke and P. Stephan, “Spray cooling on micro structured surfaces,” *Int. J. Heat Mass Transf.*, vol. 50, no. 19–20, pp. 4089–4097, 2007.

[53] R. N. Wenzel, “Resistance of solid surfaces to wetting by water,” *Ind. Eng. Chem.*, vol. 28, no. 8, pp. 988–994, 1936.

[54] M. R. Pais, L. C. Chow, and E. T. Mahefkey, “Surface Roughness and Its Effects on the Heat Transfer Mechanism in Spray Cooling,” *J. Heat Transfer*, vol. 114, no. 1, p. 211, 1992.

[55] E. A. Silk, J. Kim, and K. Kiger, “Spray cooling of enhanced surfaces: Impact of structured surface geometry and spray axis inclination,” *Int. J. Heat Mass Transf.*, vol. 49, no. 25–26, pp. 4910–4920, 2006.

[56] B. S. Kang and K. J. Choi, “Cooling of a heated surface with an impinging water spray,” *KSME Int. J.*, vol. 12, no. 4, pp. 734–740, 1998.

[57] L. Ortiz and J. E. Gonzalez, “Experiments on steady-state high heat fluxes using spray cooling,” *Exp. Heat Transf.*, vol. 12, no. 3, pp. 215–233, 1999.

[58] E. Martínez-Galván, J. C. Ramos, R. Antón, and R. Khodabandeh, “Influence of surface roughness on a spray cooling system with R134a. Part II: Film thickness measurements,” *Exp. Therm. Fluid Sci.*, vol. 48, pp. 73–80, 2013.

[59] C.-C. Hsieh and S.-C. Yao, “Evaporative heat transfer characteristics of a water spray on micro-structured silicon surfaces,” *Int. J. Heat Mass Transf.*, vol. 49, no. 5–6, pp. 962–974, 2006.

[60] Y. Wang, M. Liu, D. Liu, K. Xu, and Y. Chen, “Experimental study on the effects of spray inclination on water spray cooling performance in non-boiling regime,” *Exp. Therm. Fluid Sci.*, vol. 34, no. 7, pp. 933–942, 2010.

[61] Z. Zhang, P. X. Jiang, D. M. Christopher, and X. G. Liang, “Experimental investigation of spray cooling on micro-, nano- and hybrid-structured surfaces,” *Int. J. Heat Mass Transf.*, vol. 80, pp. 26–37, 2015.

[62] S. J. Thiagarajan, S. Narumanchi, and R. Yang, “Effect of flow rate and subcooling on spray heat transfer on microporous copper surfaces,” *Int. J. Heat Mass Transf.*, vol. 69, pp. 493–505, 2014.

[63] Z. F. Zhou, Y. K. Lin, H. L. Tang, Y. Fang, B. Chen, and Y. C. Wang, “Heat transfer enhancement due to surface modification in the close-loop R410A flash evaporation spray cooling,” *Int. J. Heat Mass Transf.*, vol. 139, pp. 1047–1055, 2019.

[64] H. Bostanci, D. P. Rini, J. P. Kizito, and L. C. Chow, “Spray Cooling With Ammonia on Microstructured Surfaces: Performance Enhancement and Hysteresis Effect,” *J. Heat Transfer*, vol. 131, no. 7, p. 071401, 2009.

[65] A. G. Ulson De Souza and J. R. Barbosa, “Experimental evaluation of spray cooling of R-134a on plain and enhanced surfaces,” *Int. J. Refrig.*, vol. 36, no. 2, pp. 527–533, 2013.

[66] B. H. Yang, H. Wang, X. Zhu, Q. Liao, Y. D. Ding, and R. Chen, “Heat transfer

enhancement of spray cooling with ammonia by microcavity surfaces," *Appl. Therm. Eng.*, vol. 50, no. 1, pp. 245–250, 2013.

[67] J. L. Xie *et al.*, "Multi-nozzle array spray cooling for large area high power devices in a closed loop system," *Int. J. Heat Mass Transf.*, vol. 78, pp. 1177–1186, 2014.

[68] H. Wang, J. J. Wu, Q. Yang, X. Zhu, and Q. Liao, "International Journal of Heat and Mass Transfer Heat transfer enhancement of ammonia spray cooling by surface modification," vol. 101, pp. 60–68, 2016.

[69] J. X. Wang, Y. Z. Li, Y. F. Mao, E. H. Li, X. Ning, and X. Y. Ji, "Comparative study of the heating surface impact on porous-material-involved spray system for electronic cooling – an experimental approach," *Appl. Therm. Eng.*, vol. 135, no. December 2017, pp. 537–548, 2018.

[70] E. Martínez-Galván, R. Antón, J. C. Ramos, and R. Khodabandeh, "Influence of surface roughness on a spray cooling system with R134a. Part I: Heat transfer measurements," *Exp. Therm. Fluid Sci.*, vol. 46, pp. 183–190, 2013.

[71] R. Qi and L. Zhang, "Recent Developments in Heat Transfer and Energy Conservation : A Review of the Selected Papers from ISHTEC2016 Recent Developments in Heat Transfer and Energy Conservation : A Review of the Selected Papers from ISHTEC 2016," *Heat Transf. Eng.*, vol. 0, no. 0, pp. 1–4, 2018.

[72] Z. Zhang, P.-X. Jiang, Y.-T. Hu, and J. Li, "Experimental Investigation of Continual- and Intermittent-Spray Cooling," *Exp. Heat Transf.*, vol. 26, no. 5, pp. 453–469, 2013.

[73] Z. Zhang, P. X. Jiang, X. L. Ouyang, J. N. Chen, and D. M. Christopher, "Experimental investigation of spray cooling on smooth and micro-structured surfaces," *Int. J. Heat Mass Transf.*, vol. 76, pp. 366–375, 2014.

[74] W. Zhang and Z. Wang, "Heat transfer enhancement of spray cooling in straight-grooved surfaces in the non-boiling regime," *Exp. Therm. Fluid Sci.*, vol. 69, pp. 38–44, 2015.

[75] K. K. Lay, B. M. Y. Cheong, W. L. Tong, M. K. Tan, and Y. M. Hung, "Effective micro-spray cooling for light-emitting diode with graphene nanoporous layers," *Nanotechnology*, vol. 28, no. 16, 2017.

[76] J. Chen, X. Chen, and G. Wang, "Phenomenon and Mechanism of Spray Cooling on Nanowire Arrayed and Hybrid Micro / Nanostructured Surfaces," vol. 140, no. November, pp. 1–16, 2018.

[77] M. S. Sehmbey, M. R. Pais, and L. C. Chow, "A Study of Diamond Laminated Surfaces in Evaporative Spray Cooling," *Mater. Sci. Monogr.*, vol. 73, no. C, pp.

275–281, 1991.

[78] B. Lin, Lanchao, Ponnappan, Rengasamy, Yerkes, Kirk, Hager, “Large Area Spray Cooling,” in *42nd AIAA Aerospace Sciences Meeting and Exhibit, Aerospace Sciences Meetings*, 2004.

[79] N. S. Dhillon, J. Buongiorno, and K. K. Varanasi, “Critical heat flux maxima during boiling crisis on textured surfaces,” *Nat. Commun.*, vol. 6, pp. 1–12, 2015.

[80] E. S. R. Negeed, N. Ishihara, K. Tagashira, S. Hidaka, M. Kohno, and Y. Takata, “Experimental study on the effect of surface conditions on evaporation of sprayed liquid droplet,” *Int. J. Therm. Sci.*, vol. 49, no. 12, pp. 2250–2271, 2010.

[81] S. Muthukrishnan and V. Srinivasan, “Enhanced Spray Cooling Using Micropillar Arrays: A Systematic Study,” *J. Heat Transfer*, 2020.

[82] S. Muthukrishnan and V. Srinivasan, “A Systematic Study of Microstructure Length Scale on Heat Transfer Enhancement in Spray Cooling,” *IEEE ITherm Conf.*, 2020.

[83] Q. Yuan, X. Huang, and Y. P. Zhao, “Dynamic spreading on pillar-arrayed surfaces: Viscous resistance versus molecular friction,” *Phys. Fluids*, vol. 26, no. 9, 2014.

[84] D. Murakami, H. Jinnai, and A. Takahara, “Wetting transition from the cassie-baxter state to the wenzel state on textured polymer surfaces,” *Langmuir*, vol. 30, no. 8, pp. 2061–2067, 2014.

[85] B. Horacek, J. Kim, and K. T. K. T. Kiger, “Spray Cooling Using Multiple Nozzles: Visualization and Wall Heat Transfer Measurements,” *IEEE Trans. Device Mater. Reliab.*, vol. 4, no. 4, pp. 614–625, 2004.

[86] S. Nishio, T. Gotoh, and N. Nagai, “Observa tion of boiling structures in high heat-flux boiling,” *Int. J. Heat Mass Transf.*, vol. 41, no. 21, pp. 3191–3201, 1998.

[87] S. Nishio and H. Tanaka, “Visualization of boiling structures in high heat-flux pool-boiling,” *Int. J. Heat Mass Transf.*, vol. 47, no. 21, pp. 4559–4568, 2004.

[88] P. J. Child, “Total Internal Reflection Fluorescence Microscopy,” *METHODS CELL Biol. Vol 30 Fluoresc. Microsc. LIVING CELLS Cult. PART B Quant. Fluoresc. Microsc. Spectrosc.*, no. 17, pp. 246–247, 1989.

[89] R. L. Magin, B. W. Mangum, J. A. Statler, and D. D. Thornton, “Transition Temperatures of the Hydrates of Na2S04 , Na2HPO4, and KF as Fixed Points in Biomedical Thermometry.,” *J. Res. Natl. Bur. Stand. (United States)*, vol. 86, no. 2, pp. 181–192, 1981.

[90] H. Preston-Thomas, “The International Temperature Scale of 1990 (ITS-90),”

metrologia, vol. 27, no. 1, pp. 3–10, 1990.

Appendix A

Thermocouple Calibration

A.1 Platinum Resistance Thermometer Calibration

The SPRT (Rosemount Model 162CE) was calibrated with reference to two fixed points – (a) the triple point of water which occurs exactly at 273.16 K or 0.01 ºC and a partial vapor pressure of 611.657 Pa, (b) the hydrate transition temperature of Sodium Sulfate Decahydrate which occurs at 32.374 ºC at 1 atm [89]. The fixed point temperature values and the corresponding resistance measured were used to obtain the values of R_{tp} and a defined by the International Temperature Scale of 1990 (ITS-90) standards [90].

$$W = \frac{R}{R_{tp}} \tag{A.1}$$

$$W - W_r = a(W - 1) \tag{A.2}$$

$$T - T_{tp} = C_0 + \sum_{i=1}^{9} C_i \left[\frac{W_r - 2.64}{1.64}\right]^i \tag{A.3}$$

Where C_i are the constants given by Preston-Thomas [90].

A.1.1 Calibration procedure

(a) Triple point of water - A Fluke triple point cell was used to create a thermal equilibrium (occurs at 273.16 K or 0.01 ºC) between the three phases of water – solid, liquid, and gas. A combination of dry ice and isopropyl alcohol (endothermic reaction) was used to achieve a temperature close 0ºC and activate the triple point cell. Care must be taken to apply

warmth (using your palms) on the outer sides of the triple point cell to prevent the formation of ice bridges at the interface. The dry ice and isopropyl alcohol were added slowly until a clear ice sheath is formed encapsulating the measure well as shown in Fig. A.1. To stabilize the triple point, the Fluke cell is kept inside an ice bath for at least 4 – 5 hours before introducing the SPRT. Later, the SPRT is inserted into the measure well 12 cm deep into the leftover isopropyl alcohol mixture and the resistance data from the SPRT (using 4-wire resistance method) were acquired using a Keithley 2750 ethernet multimeter. The resistance data measured at steady state (see fig. A.2) has a mean value of 25.5637 Ω with a measurement uncertainty close to 0.0005 Ω.

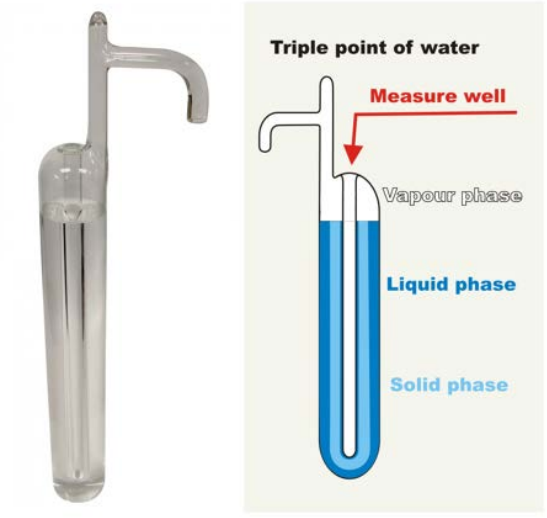

Fig. A.1 (a) A picture of the Fluke™ triple point cell (left) (b) A schematic of the triple point cell at thermal equilibrium with the three phases – Solid, liquid, and gas.

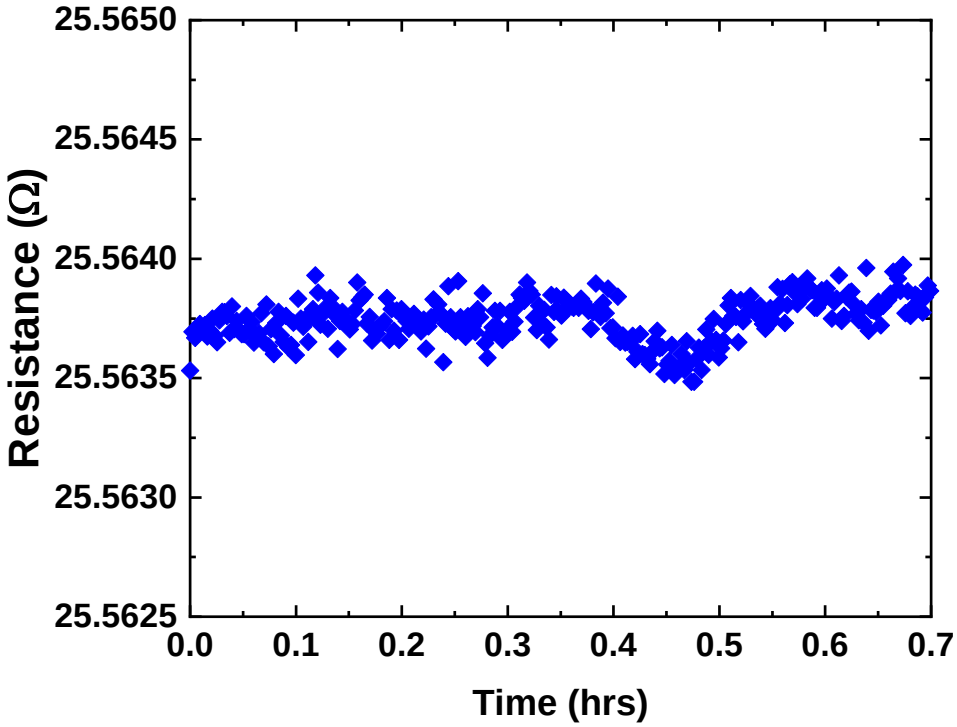

Fig. A.2 Time-series resistance data plot obtained at the triple point of water using the Model 162CE SPRT. Note that the measurement uncertainty is less than 0.0005 Ω.

(b) Hydration point of Na_2SO_4 – Sodium Sulfate anhydrous salt (34 – 44% by weight) was added to a 4-liter beaker and mixed with distilled water. The resulting solution was heated up to 40 °C on a hot plate while stirring using a magnetic bead. At the point, the SPRT was introduced 12 cm deep inside the beaker and the data acquisition was started. Then, the solution was cooled down slowly to 32 °C. If needed, add 5 - 10 g of Sodium Sulphate anhydrous salt to initiate the crystallization process while stirring the solution vigorously. At some instant, a sudden jump in the resistance (i.e., the temperature) of the SPRT, indicating the inception of the hydration of the sodium sulfate crystals. Ensure that stirring was continued using magnetic stirrer until the end of the experiment. The beaker was encapsulated by a thermal insulation layer made of aluminum foil and glass fiber to prevent heat loss due to natural convection. The resistance data measured at steady state (see fig. A.4) has a mean value of 28.8447 Ω with a measurement uncertainty close to 0.0015 Ω.

Fig. A.3 A picture of the hydration point cell as seen from the top, featuring a magnetic bead, Model 162CE SPRT, and the thermal insulation pack (around the beaker).

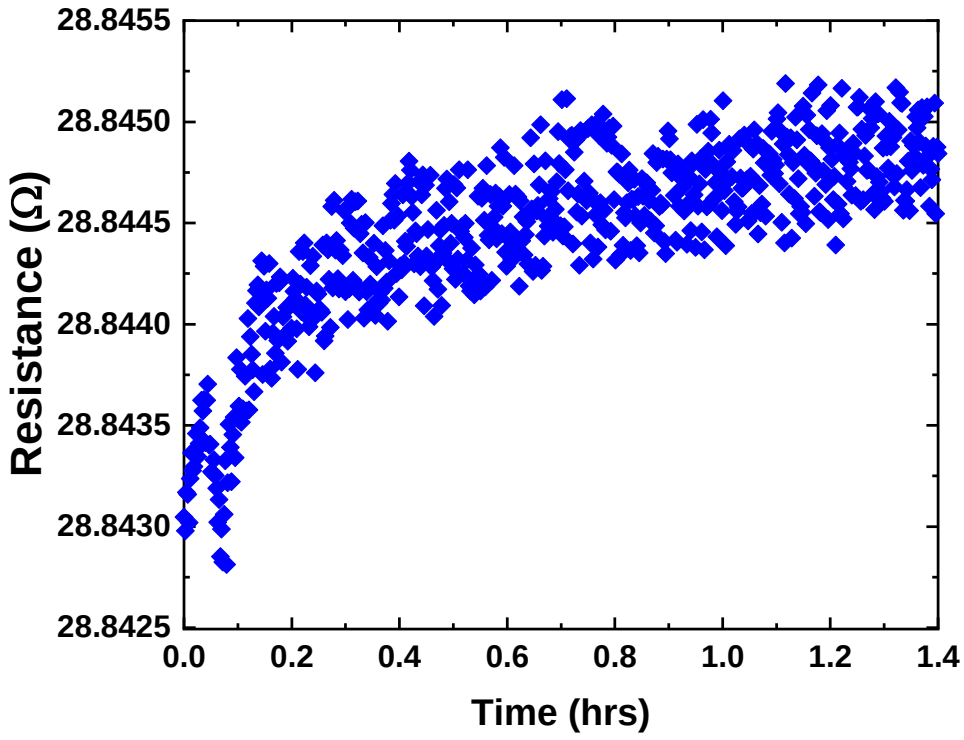

Fig. A.4 Time-series resistance data plot obtained at the transition hydration point of Sodium Sulfate Decahydrate using the Model 162CE SPRT. Note that the measurement uncertainty is less than 0.002 Ω.

A.2 T-type Thermocouple Calibration

The T-type thermocouples (Omega^{TM} TT-T-30SLE (ROHS)) used in the heat transfer experiments were calibrated against a standard platinum resistance thermometer (SPRT). The thermocouples were bonded using a spot-welder and ten such bonded thermocouples were randomly chosen for the calibration experiments.

A.2.1 Calibration procedure

Both the 10-set of thermocouples and the SPRT were immersed into a silicone bath (See fig. A.6) contained in Neslab RTE-111 chiller/heater recirculator (See fig. A.5) to maintain temperatures between 5°C - 145°C. The other ends of each thermocouple junctions were placed inside a glass test tube containing motor oil and the test tubes are immersed into an reference ice bath with a Styrofoam lid (See fig. A.7). Temperatures were incremented by 5°C starting at 5°C and the corresponding temperature and resistance data were acquired at steady state through Keithley^{TM} 2750 ethernet multimeter using a Python code displayed in Appendix B.1.

Fig. A.5 Pictures showing the front and back view of the Neslab RTE-111 chiller/heater recirculator

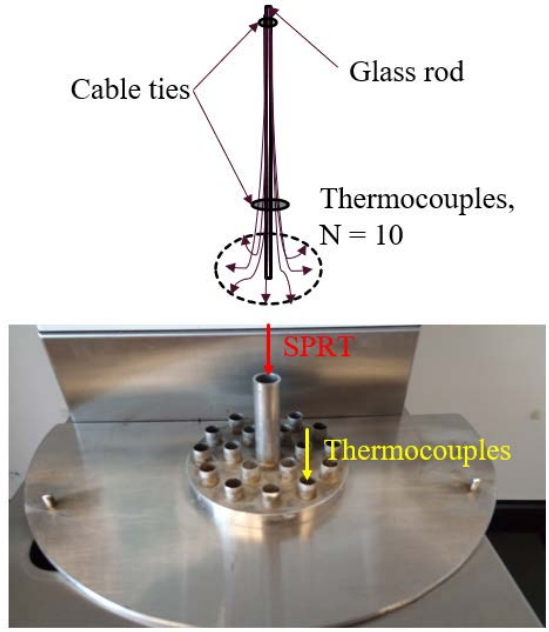

Fig. A.6 Picture and schematic showing the arrangement of the Model 162CE SPRT and the thermocouples inside the Silicone bath.

Fig. A.7 Pictures showing the arrangement of thermocouples junctions inside the reference ice bath and the corresponding wire connections.

The obtained results were processed, and the resulting curve fit produced a polynomial equation (eq. A.4) relating the temperature and the differential voltage values measured by the thermocouples. The total uncertainty in the temperature was found to be 0.03 K (using eq. A.5).

$$T - 273.26 = (2.49E07)\,V^3 - 669600\,V^2 + 25751\,V \tag{A.4}$$

$$U_{temp\_total} = \sqrt{U_{temp\_volt}^2 + U_{temp\_res}^2 + U_{temp\_conv}^2 + U_{RMSE}^2} \tag{A.5}$$

Appendix B

Python Modules

The following codes were used to acquire temperature, and applied power values from the DAQ and the programmable power supply during thermocouple calibration, heat transfer experiments, and Total internal reflection microscopy.

All the codes given below are coded to execute in Python version 3.8.5. For obtaining the full Python package, please download the latest version of Anaconda from https://www.anaconda.com/products/individual

B.1 Thermocouple Calibration

```
import time
#import socket
import serial
import numpy as np
import matplotlib.pyplot as plt
import matplotlib.ticker as ticker

def reset():
    p.write("*RST\n".encode())          #Returns model 2701 to
the *RST default conditions
    p.write("*CLS\n".encode())         #Clears all event
registers and error queue
    p.write("TRAC:CLE\n".encode())      #Clears buffer
    p.write("ROUT:OPEN:ALL\n".encode())  #Opens up all the
channels in slot 7700 to ensure no erroneous readings are
recorded
    p.write("SYST:LSYN ON\n".encode())    #Setting Line Cycle
Synchronization ON. This reduces common mode and normal mode
noise in the readings


def display():
    p.write("DISP:TEXT:STAT ON\n".encode()) #turn on the text
message mode
```

```
    p.write("DISP:TEXT:DATA 'READY'\n".encode())  #displays
'READY' on the screen

#basic scan process does the following: (1) opens any closed
channel, (2) perform the measurement, (3) close a channel. This
is repeated for each channel specified
#refer to section 7-5 of the Keithley 2701 manual to understand
difference between SCAN and STEP & TIMER and Delay.
#roughly, when using scan, delay controls the time between each
channel scan and timer controls the time between two sets of
scans
#(for eg., 1 set of scan = 10 channels (say) and number of scans
performed = 3 (say))

def setDCV():
    p.write("FUNC 'VOLT:DC', (@101, 102, 103, 104, 105, 106, 107,
108, 109, 110, 113)\n".encode())           #sets the instrument
to measure voltage in DC
    p.write("VOLT:DC:DIG 7, (@101, 102, 103, 104, 105, 106, 107,
108, 109, 110, 113)\n".encode())           #makes the display
show digits up to the 7th decimal place
    p.write("VOLT:DC:NPLC 5, (@101, 102, 103, 104, 105, 106, 107,
108, 109, 110, 113)\n".encode())           #number of power life
cycles. It signifies a balance between accuracy and speed. Higher
the NPLC, lower the speed and higher the accuracy, and vice versa
def set4WOHM():
    p.write("FUNC 'FRES', (@119)\n".encode())              #sets
the instrument to measure voltage in DC
    p.write("FRES:NPLC 5, (@119)\n".encode())         #number of
power life cycles. It signifies a balance between accuracy and
speed. Higher the NPLC, lower the speed and higher the accuracy,
and vice versa
    p.write("FRES:AVER:TCON REP\n".encode())
    p.write("FRES:AVER:WIND 0.01\n".encode())
    p.write("FRES:AVER:COUN 20, (@119)\n".encode())
    p.write("FRES:AVER ON, (@119)\n".encode())
#    p.write("ROUT:CLOS (@119)\n".encode())

def scanVoltConfig():
    # configure the scanning operation
    # when a simple scan is configured, the present function and
range setting applies to all channels in the scan.

    # auto delay is configured such that there is sufficient
settling period for function changes, autorange changes and
multi-phase measurements
    p.write("TRAC:CLE\n".encode())
    p.write("TRIG:SOUR IMM\n".encode())
    p.write("TRIG:COUN 1\n".encode())
    p.write("SAMP:COUN 11\n".encode())
    p.write("ROUT:SCAN (@101, 102, 103, 104, 105, 106, 107, 108,
109, 110, 113)\n".encode())
```

```
    p.write("ROUT:SCAN:TSO IMM\n".encode())                    #
start scan when it is enabled and triggered
    p.write("ROUT:SCAN:LSEL INT\n".encode())                   #
initiate scanning process

def scanFResConfig():
    # configure the scanning operation
    # when a simple scan is configured, the present function and
range setting applies to all channels in the scan.

    # auto delay is configured such that there is sufficient
settling period for function changes, autorange changes and
multi-phase measurements
    p.write("FRES:AVER:TCON REP\n".encode())
    p.write("FRES:AVER:WIND 0.01\n".encode())
    p.write("FRES:AVER:COUN 20, (@119)\n".encode())
    p.write("FRES:AVER ON, (@119)\n".encode())
    p.write("ROUT:CLOS (@119)\n".encode())
    p.write("TRAC:CLE\n".encode())
    p.write("TRIG:SOUR IMM\n".encode())
    p.write("TRIG:COUN 1\n".encode())
    p.write("SAMP:COUN 1\n".encode())
    p.write("ROUT:SCAN (@119)\n".encode())
    p.write("ROUT:SCAN:TSO IMM\n".encode())
    p.write("ROUT:SCAN:LSEL INT\n".encode())

def scanVoltDo(filename):
    # initializes scan and stores data to a file
    p.write("READ?\n".encode())                    # read and
return the values scanned
    p.write("ROUT:SCAN:LSEL NONE\n".encode())     # stop the
scanning process
    time.sleep(1)
    a = p.readline()     # 44 is the buffer size taken by a
single reading (includes time stamp and reading no.). The size of
the buffer should be 44(~50) x scans x channels
    a = str(a)
    text=open(filename,"w")
    text.write(a)                                 # write the
obtained data to a file in the format:
(eg.)0.00001DCV,00000SECS,#00001RDNG
    text.close()

def scanFResDo(filename):
    # initializes scan and stores data to a file
    p.write("READ?\n".encode())    # read and return the values
scanned
    p.write("ROUT:SCAN:LSEL NONE\n".encode())     # stop the
scanning process
    time.sleep(1)
```

```
    b = p.readline()     # 44 is the buffer size taken by a
single reading (includes time stamp and reading no.). The size of
the buffer should be 44(~50) x scans x channels
    b = str(b)
#    print (a)
    text=open(filename,"w")
    text.write(b)                                # write the
obtained data to a file in the format:
(eg.)0.00001VDC,00000SECS,#00001RDNG
    text.close()

def returnVoltage(from_filename):
     #returns the voltage value recorded. Return type is a list
of only voltage readings. Also reads the data to a file
    text = open(from_filename, "r")
    data = text.read()                       #reads all the data
into a single string 'data'
    data = data.replace('b\'','')
#    print (data)
    data = data.split(',')                   #splits the entire
string at every ','
#    print (data)
    voltage =[]
    for i in range(0, len(data), 3) :
        word = data[i]
        word1 = word.replace('VDC','')           # removes the
unit attached to the voltage readings
        word2 = abs(float(word1))                # converts the
value to float for easy manipulation
        voltage.append(word2)                    # appends the
converted number to a list
    return voltage

def returnResistance(from_filename):
     #returns the voltage value recorded. Return type is a list
of only voltage readings. Also reads the data to a file
    text = open(from_filename, "r")
    data = text.read()                       #reads all the data
into a single string 'data'
    data = data.split(',')                   #splits the entire
string at every ','
    word = data[0]
    word1 = word.replace('b\'','')           # removes the unit
attached to the voltage readings
    word2 = word1.replace('OHM4W','')
    Res_value = abs(float(word2))                # converts the
value to float for easy manipulation
#    print (Res_value)
    return Res_value

def close():
```

```
     #close the socket connection. Have to close the socket
after every operation without fail. Even if the program is
stopped in between using keyboard interrupt, the socket
connection should be closed before restarting it

    p.write("DISP:TEXT:DATA 'CLOSING'\n".encode())
    time.sleep(3)
    p.write("DISP:TEXT:STAT OFF\n".encode())
    p.write("ROUT:OPEN:ALL\n".encode())
    p.close()


########################
#     MAIN PROGRAM     #
########################

p = serial.Serial("/dev/ttyUSB0", 9600, xonxoff = True)

# User Input: Heat Flux in watts
print ("Enter the Temperature Applied (deg. C):")
temperature = float(input())

reset()                                                 #clearing
and resetting buffer
#display()                                              #set up
the display screen
set4WOHM()

#scanFResConfig()

h=open("Thermocouple_Calibration_"+str(time.strftime("%d-%m-
%Y"))+"_Temperature="+str(int(temperature))+".txt",'a')
h.write("Temperature = "+str(temperature)+"\n")
h.write("PRT_Resistance\tVoltage_1\tVoltage_2\tVoltage_3\tVoltage
_4\t \
Voltage_5\tVoltage_6\tVoltage_7\tVoltage_8\tVoltage_9\tVoltage_10
\tZero_error\n ")
h.close()

Resistance = []
plot_time=[]
plt.ion()
y_formatter=ticker.ScalarFormatter(useOffset=False)
start_time=time.time()

lower_index = 0
for i in range(0,2000):
    scanFResConfig()
    scanFResDo("temp.txt")            #scanning takes place
    current_time=time.time()-start_time
    plot_time=np.append(plot_time,current_time)
```

```
    Resistance.append(returnResistance("temp.txt"))         #only
the float values of the DC voltages are returned; First reading -
Heater; Second reading - atmosphere
    #dynamicplot(Resistance,plot_time)
    plt.clf()
    plt.plot(plot_time/3600.0,Resistance)
    ax = plt.gca()
    ax.ticklabel_format(useOffset=False)
    plt.draw()
#    plt.show()
    plt.pause(0.001)

    if i > 50:
        upper_index = i
        local_Res= Resistance[lower_index:upper_index]
        STD_Res = np.std(local_Res)
        print(STD_Res)
        if STD_Res > 6E-4:
#            print "Temperature is UNSTEADY...\n"
            lower_index = lower_index + 1
            continue
        else:
            print ("Temperature is STABLE...\n")
            print ("Acquring data...\n")
#            setDCV()
            for j in range(0,250):
                #Acquiring resistance values from SPRT
                Resistance_final = 0.0
                set4WOHM()
                scanFResConfig()
                scanFResDo("temp.txt")           #scanning takes
place
                current_time=time.time()-start_time
                plot_time=np.append(plot_time,current_time)
                Resistance_final = returnResistance("temp.txt")
     #only the float values of the DC voltages are returned;
First reading - Heater; Second reading - atmosphere
                Resistance.append(Resistance_final)         #only
the float values of the DC voltages are returned; First reading -
Heater; Second reading - atmosphere
                plt.clf()
                plt.plot(plot_time/3600.0,Resistance)
                ax = plt.gca()
                ax.ticklabel_format(useOffset=False)
                plt.draw()
                plt.pause(0.001)

                #Acquiring voltage values from 10 thermocouples
                setDCV()
                scanVoltConfig()
                scanVoltDo("temp1.txt")               #scanning
takes place
```

```
                voltage = []
                voltage = returnVoltage("temp1.txt")


h=open("Thermocouple_Calibration_"+str(time.strftime("%d-%m-
%Y"))+"_Temperature="+str(int(temperature))+".txt",'a')

h.write('{}\t{}\t{}\t{}\t{}\t{}\t{}\t{}\t{}\t{}\t{}\t{}\t{}\t\n'.form
at(str(Resistance_final), \
                str(voltage[0]), str(voltage[1]),
str(voltage[2]), str(voltage[3]), str(voltage[4]),
str(voltage[5]),\
                str(voltage[6]), str(voltage[7]),
str(voltage[8]), str(voltage[9]), str(voltage[10])))
                h.close()
            break
    time.sleep(1)
print ("Data Acquisition complete...\n")
print ("Set the next temperature and rerun the code...\n")
close()
```

B.2 Heat Transfer Experiments

```
import serial
import time
import socket
import numpy as np
import matplotlib.pyplot as plt
import matplotlib.ticker as ticker

def InitialResistance():
#    s.sendall("*RST\n".encode())
    s.sendall("*CLS\n".encode())
    s.sendall("VOLT 10\n".encode()) # Applied voltage
    s.sendall("VOLT:PROT:LEV 300\n".encode())
    s.sendall("CURR:PROT:STAT 0\n".encode())
    s.sendall("OUTP ON\n".encode()) # Turning the output
    print ("\n Calculating resistance of the chip and setting
power...\n")
    #time.sleep(5)
    s.sendall("MEAS:CURR?\n".encode())
    s.sendall("READ?\n".encode())   # Reads the output voltage
and current from the power supply
    a = s.recv(30)
#    print (a)
#    time.sleep(2)
    s.sendall("*CLS\n".encode())
    s.sendall("MEAS:VOLT?\n".encode())
    s.sendall("READ?\n".encode())   # Reads the output voltage
and current from the power supply
```

```
    b = s.recv(30)
#    print (b)
#    s.sendall("OUTP OFF\n".encode())

    a1 = str(a)
    a2 = a1.replace('b\'','')
    a3 = a2.replace('\\n\'','')
    I = float(a3)

    b1 = str(b)
    b2 = b1.replace('b\'','')
    b3 = b2.replace('\\n\'','')
    V = float(b3)

    R = V/I
    print ("Initial resistance = %f" %R)
    return R

def SetInitialPower(P,R):
    V = ((P*R)**0.5)
    print ("\n Setting voltage to %f\n" %V)
    str1 = "VOLT "+str(V)+"\n"
    s.sendall(str1.encode()) # Applied voltage
    time.sleep(5)
    print ("The power has been set to %f" %P)

def SetPower(P,R):
#    s.sendall("OUTP ON\n")
    V = ((P*R)**0.5)
    print ("\n Setting voltage to %f\n" %V)
    str1 = "VOLT "+str(V)+"\n"
    s.sendall(str1.encode()) # Applied voltage
    time.sleep(2)
    print ("The power has been reset to %f W" %P)

def CheckResistance():
    print ("\n Checking resistance...\n")
    #time.sleep(5)
    s.sendall("MEAS:CURR?\n".encode())
    s.sendall("READ?\n".encode())   # Reads the output voltage
and current from the power supply
    a = s.recv(30)
#    time.sl eep(1)
#    print (a)
#    time.sleep(2)
    s.sendall("MEAS:VOLT?\n".encode())
    s.sendall("READ?\n".encode())   # Reads the output voltage
and current from the power supply
    b = s.recv(30)
#    time.sleep(1)
#    print (b)
#    s.sendall("OUTP OFF\n".encode())
```

```
    a1 = str(a)
    a2 = a1.replace('b\'','')
    a3 = a2.replace('\\n\'','')
    I = float(a3)

    b1 = str(b)
    b2 = b1.replace('b\'','')
    b3 = b2.replace('\\n\'','')
    V = float(b3)

    R = V/I
    Par = [R, V, I]
    return Par

def reset():
     #attribute for clearing the buffer and the display screen
of the Keithley. To ensure no error in the program, use before
every significant function that the Keithley performs
    p.write("*RST\n".encode())          #Returns model 2701 to
the *RST default conditions
    p.write("*CLS\n".encode())         #Clears all event
registers and error queue
    p.write("TRAC:CLE\n".encode())      #Clears buffer
    p.write("ROUT:OPEN:ALL\n".encode())  #Opens up all the
channels in slot 7700 to ensure no erroneous readings are
recorded
    p.write("SYST:LSYN ON\n".encode())    #Setting Line Cycle
Synchronization ON. This reduces common mode and normal mode
noise in the readings

def setDCV():
    p.write("FUNC 'VOLT:DC'\n".encode())              #sets the
instrument to measure voltage in DC
    p.write("VOLT:DC:DIG 7\n".encode())               #makes the
display show digits up to the 7th decimal place
    p.write("VOLT:DC:NPLC 5\n".encode())              #number of
power life cycles. It signifies a balance between accuracy and
speed. Higher the NPLC, lower the speed and higher the accuracy,
and vice versa
#    p.write("VOLT:AVER:TCON REP\n".encode())    time.sleep(10)

#    p.write("VOLT:AVER:WIND 0.01\n".encode())
#    p.write("VOLT:AVER:COUN 20, (@102)\n".encode())
#    p.write("VOLT:AVER ON, (@102)\n".encode())

def scanConfig():
    # configure the scanning operation
    # when a simple scan is configured, the present function and
range setting applies to all channels in the scan.
```

```
    # auto delay is configured such that there is sufficient
settling period for function changes, autorange changes and
multi-phase measurements
    p.write("TRAC:CLE\n".encode())
    p.write("TRIG:SOUR IMM\n".encode())
    p.write("TRIG:COUN 1\n".encode())
    p.write("SAMP:COUN 3\n".encode())
    p.write("ROUT:SCAN (@101,103,104)\n".encode())
    p.write("ROUT:SCAN:TSO IMM\n".encode())                    #
start scan when it is enabled and triggered
    p.write("ROUT:SCAN:LSEL INT\n".encode())                   #
initiate scanning process

def scanDo(filename):
    # initializes scan and stores data to a file
    p.write("READ?\n".encode())                    # read and
return the values scanned
    p.write("ROUT:SCAN:LSEL NONE\n".encode())     # stop the
scanning process
    time.sleep(3)
    a = p.readline()     # 44 is the buffer size taken by a
single reading (includes time stamp and reading no.). The size of
the buffer should be 44(~50) x scans x channels
    a = str(a)
    text=open(filename,"w")
    text.write(a)                                  # write the
obtained data to a file in the format:
(eg.)0.00001DCV,00000SECS,#00001RDNG
    text.close()

def returnVoltage(from_filename):
     #returns the voltage value recorded. Return type is a list
of only voltage readings. Also reads the data to a file
    text = open(from_filename, "r")
    data = text.read()                        #reads all the data
into a single string 'data'
    data = data.replace('b\'','')
#    print (data)
    data = data.split(',')                    #splits the entire
string at every ','
#    print (data)
    voltage =[]
    for i in range(0, len(data), 3) :
        word = data[i]
        word1 = word.replace('VDC','')          # removes the
unit attached to the voltage readings
        word2 = abs(float(word1))               # converts the
value to float for easy manipulation
        voltage.append(word2)                   # appends the
converted number to a list

    return voltage
```

```
def close():
     #close the socket connection. Have to close the socket
after every operation without fail. Even if the program is
stopped in between using keyboard interrupt, the socket
connection should be closed before restarting it
    p.write("ROUT:OPEN:ALL\n".encode())
    p.write("SYST:BEEP ON\n".encode())
    time.sleep(2)
    p.close()
    s.close()

########################
#     MAIN PROGRAM     #
########################

s = socket.socket(socket.AF_INET, socket.SOCK_STREAM) # Creating
socket using the socket family and socket type, respectively
s.connect(("169.254.57.3",5025))            # Establishing the
connection with the created socket (Through LAN).

p = serial.Serial("COM5", 9600, xonxoff = True) #For Windows
#p = serial.Serial("/dev/ttyUSB0", 9600, xonxoff = True) #For
Linux

Flow_rate = 30 #Volumetric flow rate

for i in range(0,6):
    P = (i+1)*30
    print ("Enter the HEAT INPUT in W: %f" %(P))
    print ("Enter the LIQUID FLOW RATE in ml/min: %d"
%(Flow_rate))
    if i == 0:
        R_i = InitialResistance()                #
initialresistance() - User-defined function to calculate the
initial resistance
    else:
        text = open("temp1", "r")
        data = text.read()                      #reads all the
data into a single string 'data'
        R_i = abs(float(data))
        pass

    SetInitialPower(P, R_i)                          # setpower()
- User-defined function to calculate the voltage based on
changing resistance
    time.sleep(10)
    reset()
     #clearing and resetting buffer
    setDCV()
```

```
    #h=open("Main_experiments_"+str(time.strftime("%d-%m-
%Y"))+"_HeatInput="+str(int(P))+"_FlowRate="+str(int(flow_rate))+
".txt",'a')
    #h.write("Heat Input = "+str(P)+"\n")
    #h.write("Flow rate = "+str(flow_rate)+"\n")

#h.write("Chip_Resistance\tSupply_Voltage\tSupply_Current\tTC1_vo
ltage\tTC2_voltage\tTC3_voltage\tTC4_voltage\tTemperature_1\tTemp
erature_2\tTemperature_3\tTemperature_4\tTC5_voltage\tTemperature
_subcool\n ")
    #h.close()

    Temperature1 = []
    Temperature2 = []
    Temperature3 = []

    Resistance = []
    plot_time=[]
    plt.ion()
    y_formatter=ticker.ScalarFormatter(useOffset=False)
    start_time=time.time()

    lower_index = 0
    #lower_index_R = 0
    for i in range(0,2000):
        Par = CheckResistance()
        Resistance_local = Par[0]
        V_local = Par[1]
        I_local = Par[2]
        Power = V_local*I_local
        Resistance.append(Resistance_local)
        SetPower(P,Resistance[i-1])
        #scanning for acquiring temperature readings
        scanConfig()
        scanDo("temp")                #scanning takes place
        current_time=time.time()-start_time
        plot_time=np.append(plot_time,current_time)
        TC_Voltage = returnVoltage("temp")       #only the float
values of the DC voltages are returned; First reading - Heater;
Second reading - atmosphere
        TC_Voltage_mV1 = TC_Voltage[0]*1000
        TC_Voltage_mV2 = TC_Voltage[1]*1000
        TC_Voltage_mV3 = TC_Voltage[2]*1000

    #    Temperature_local = -7.293422E-7*(TC_Voltage_mV**6) +
6.048144E-5*(TC_Voltage_mV**5) - 0.002165394*(TC_Voltage_mV**4) +
0.04637791*(TC_Voltage_mV**3) - 0.7602961*(TC_Voltage_mV**2) +
25.928*(TC_Voltage_mV)  #T-type thermocouples (From NIST curve)
        Temperature_local1 = 0.0249*(TC_Voltage_mV1**3) -
0.6696*(TC_Voltage_mV1**2) + 25.751*(TC_Voltage_mV1) + 0.11  #T-
type thermocouples (From Calibration curve)
```

```
        Temperature_local2 = 0.0249*(TC_Voltage_mV2**3) -
0.6696*(TC_Voltage_mV2**2) + 25.751*(TC_Voltage_mV2) + 0.11  #T-
type thermocouples (From Calibration curve)
        Temperature_local3 = 0.0249*(TC_Voltage_mV3**3) -
0.6696*(TC_Voltage_mV3**2) + 25.751*(TC_Voltage_mV3) + 0.11  #T-
type thermocouples (From Calibration curve)

    #    print (Temperature_local1, Temperature_local2)
        Temperature1.append(Temperature_local1)
        Temperature2.append(Temperature_local2)
        Temperature3.append(Temperature_local3)

        #dynamicplot(Resistance,plot_time)
        plt.clf()
        plt.plot(plot_time/3600.0, Temperature1,
plot_time/3600.0, Temperature2, plot_time/3600.0, Temperature3)
        ax = plt.gca()
        ax.ticklabel_format(useOffset=False)
        plt.draw()
        plt.show()
        plt.pause(0.001)
        h=open("Main_experiments_"+str(time.strftime("%d-%m-
%Y"))+"_HeatInput="+str(int(P))+"_FlowRate="+str(int(Flow_rate))+
".txt",'a')

h.write('{}\t{}\t{}\t{}\t{}\t{}\t{}\t{}\t{}\t{}\t{}\t\n'.format(str(R
esistance_local), str(V_local), str(I_local), str(Power),
str(TC_Voltage_mV1), str(TC_Voltage_mV2), str(TC_Voltage_mV3),
str(Temperature_local1), str(Temperature_local2),
str(Temperature_local3)))
        h.close()
        time.sleep(1)
        if i > 50:
            upper_index = i-1
            local_Temp1= Temperature1[lower_index:upper_index]
            local_Temp2= Temperature2[lower_index:upper_index]
            local_Temp3= Temperature3[lower_index:upper_index]
            STD_Temp1 = np.std(local_Temp1)
            STD_Temp2 = np.std(local_Temp2)
            STD_Temp3 = np.std(local_Temp3)

            print ("\n Standard deviation of temperature: %f, %f,
%f\n" %(STD_Temp1, STD_Temp2, STD_Temp3))
    #        print(STD_Temp)
            if (STD_Temp1 > 0.75):
    #        if (STD_Temp1 > 0.5) or (STD_Temp2 > 0.5):
    #            print "Temperature is UNSTEADY...\n"
                R1 = str(Resistance_local)
                text=open("temp1","w")
                text.write(R1)                                  #
write the obtained data to a file in the format:
(eg.)0.00001DCV,00000SECS,#00001RDNG
```

```
                text.close()
                lower_index = lower_index + 1
                continue
            else:
                R1 = str(Resistance_local)
                text=open("temp1","w")
                text.write(R1)                                  #
write the obtained data to a file in the format:
(eg.)0.00001DCV,00000SECS,#00001RDNG
                text.close()
                print ("Temperature is STABLE...\n")
                break


    #fig = plt.figure()
    #fig.savefig('Main_experiments_'+str(time.strftime("%d-%m-
%Y"))+'_HeatInput='+str(int(P))+'_FlowRate='+str(int(flow_rate))+
'.pdf')
    print ("Moving on to next heat flux setting...\n")

for i in range(0,200):
    P = 180 + (i+1)*10
    print ("Enter the HEAT INPUT in W: %f" %(P))
    print ("Enter the LIQUID FLOW RATE in ml/min: %d"
%(Flow_rate))
    text = open("temp1", "r")
    data = text.read()                      #reads all the data
into a single string 'data'
    R_i = abs(float(data))
    SetInitialPower(P, R_i)                          # setpower()
- User-defined function to calculate the voltage based on
changing resistance
    time.sleep(10)
    reset()
     #clearing and resetting buffer
    setDCV()

    #h=open("Main_experiments_"+str(time.strftime("%d-%m-
%Y"))+"_HeatInput="+str(int(P))+"_FlowRate="+str(int(flow_rate))+
".txt",'a')
    #h.write("Heat Input = "+str(P)+"\n")
    #h.write("Flow rate = "+str(flow_rate)+"\n")

#h.write("Chip_Resistance\tSupply_Voltage\tSupply_Current\tTC1_vo
ltage\tTC2_voltage\tTC3_voltage\tTC4_voltage\tTemperature_1\tTemp
erature_2\tTemperature_3\tTemperature_4\tTC5_voltage\tTemperature
_subcool\n ")
    #h.close()

    Temperature1 = []
    Temperature2 = []
    Temperature3 = []
```

```
    Resistance = []
    plot_time=[]
    plt.ion()
    y_formatter=ticker.ScalarFormatter(useOffset=False)
    start_time=time.time()

    lower_index = 0
    #lower_index_R = 0
    for i in range(0,2000):
        Par = CheckResistance()
        Resistance_local = Par[0]
        V_local = Par[1]
        I_local = Par[2]
        Power = V_local*I_local
        Resistance.append(Resistance_local)
        SetPower(P,Resistance[i-1])
        #scanning for acquiring temperature readings
        scanConfig()
        scanDo("temp")                #scanning takes place
        current_time=time.time()-start_time
        plot_time=np.append(plot_time,current_time)
        TC_Voltage = returnVoltage("temp")       #only the float
values of the DC voltages are returned; First reading - Heater;
Second reading - atmosphere
        TC_Voltage_mV1 = TC_Voltage[0]*1000
        TC_Voltage_mV2 = TC_Voltage[1]*1000
        TC_Voltage_mV3 = TC_Voltage[2]*1000
    #    Temperature_local = -7.293422E-7*(TC_Voltage_mV**6) +
6.048144E-5*(TC_Voltage_mV**5) - 0.002165394*(TC_Voltage_mV**4) +
0.04637791*(TC_Voltage_mV**3) - 0.7602961*(TC_Voltage_mV**2) +
25.928*(TC_Voltage_mV)  #T-type thermocouples (From NIST curve)
        Temperature_local1 = 0.0249*(TC_Voltage_mV1**3) -
0.6696*(TC_Voltage_mV1**2) + 25.751*(TC_Voltage_mV1) + 0.11  #T-
type thermocouples (From Calibration curve)
        Temperature_local2 = 0.0249*(TC_Voltage_mV2**3) -
0.6696*(TC_Voltage_mV2**2) + 25.751*(TC_Voltage_mV2) + 0.11  #T-
type thermocouples (From Calibration curve)
        Temperature_local3 = 0.0249*(TC_Voltage_mV3**3) -
0.6696*(TC_Voltage_mV3**2) + 25.751*(TC_Voltage_mV3) + 0.11  #T-
type thermocouples (From Calibration curve)

    #    print (Temperature_local1, Temperature_local2)
        Temperature1.append(Temperature_local1)
        Temperature2.append(Temperature_local2)
        Temperature3.append(Temperature_local3)

        #dynamicplot(Resistance,plot_time)
        plt.clf()
        plt.plot(plot_time/3600.0, Temperature1,
plot_time/3600.0, Temperature2, plot_time/3600.0, Temperature3)
        ax = plt.gca()
```

```
        ax.ticklabel_format(useOffset=False)
        plt.draw()
        plt.show()
        plt.pause(0.001)
        h=open("Main_experiments_"+str(time.strftime("%d-%m-
%Y"))+"_HeatInput="+str(int(P))+"_FlowRate="+str(int(Flow_rate))+
".txt",'a')

h.write('{}\t{}\t{}\t{}\t{}\t{}\t{}\t{}\t{}\t{}\t{}\t{}\t\n'.format(str(R
esistance_local), str(V_local), str(I_local), str(Power),
str(TC_Voltage_mV1), str(TC_Voltage_mV2), str(TC_Voltage_mV3),
str(Temperature_local1), str(Temperature_local2),
str(Temperature_local3)))
        h.close()
        time.sleep(1)
        if i > 50:
            upper_index = i-1
            local_Temp1= Temperature1[lower_index:upper_index]
            local_Temp2= Temperature2[lower_index:upper_index]
            local_Temp3= Temperature3[lower_index:upper_index]
            STD_Temp1 = np.std(local_Temp1)
            STD_Temp2 = np.std(local_Temp2)
            STD_Temp3 = np.std(local_Temp3)

            print ("\n Standard deviation of temperature: %f, %f,
%f\n" %(STD_Temp1, STD_Temp2, STD_Temp3))
    #        print(STD_Temp)
            if (STD_Temp1 > 0.75):
    #        if (STD_Temp1 > 0.5) or (STD_Temp2 > 0.5):
    #            print "Temperature is UNSTEADY...\n"
                R1 = str(Resistance_local)
                text=open("temp1","w")
                text.write(R1)                                  #
write the obtained data to a file in the format:
(eg.)0.00001DCV,00000SECS,#00001RDNG
                text.close()
                lower_index = lower_index + 1
                continue
            else:
                R1 = str(Resistance_local)
                text=open("temp1","w")
                text.write(R1)                                  #
write the obtained data to a file in the format:
(eg.)0.00001DCV,00000SECS,#00001RDNG
                text.close()
                print ("Temperature is STABLE...\n")
                break


    #fig = plt.figure()
```

```
    #fig.savefig('Main_experiments_'+str(time.strftime("%d-%m-
%Y"))+'_HeatInput='+str(int(P))+'_FlowRate='+str(int(flow_rate))+
'.pdf')
    if (P == 350):
        print ("Moving on to next heat flux setting?\n")
        print ("Press 0 to continue\n")
        flag = int(input())
    else:
        continue


close()
```

B.3 Data Processing for heat transfer experiments

```
# -*- coding: utf-8 -*-
"""
Created on Wed Mar 14 20:50:33 2018
@author: $ankar
Created for retrieving and processing the data from the text
files
Each text file contains following columns
Electrical input parameters: Chip resistance, Supply voltage,
Supply current,
                                  Supply power
Thermocouple on chip (TC) output: TC Voltage, TC Temperature (for
each TC)
Thermocouple on water line output: TC Voltage, TC Temperature
"""
import glob
import numpy as np
#import matplotlib.pyplot as plt
import time

flow_rate = 30
print ("Surface type: [(1) NanoWires (NW) (2) Micropillars (MP)
(3) Plain surface]" )
S_type = int(input())
print ("Enter the no. of thermocouples on the chip:")
TC = int(input())
Col = 4 + 2*(TC)
N = 30 #Number of samples per thermocouple to reach steady-state
Chip_res_mean = []
Supply_pow_mean = []
TC1_mean = []
TC2_mean = []
TC3_mean = []
TC4_mean = []
TC5_mean = []
```

```
Chip_res_std = []
Supply_pow_std = []
TC1_std = []
TC2_std = []
TC3_std = []
TC4_std = []
TC5_std = []
for fil in glob.glob('*.txt'):
    f=open(fil,"r")
    lines=f.readlines()
    result=[]
    for x in lines:
        for i in range(0, Col):
            result.append(x.split('\t')[i])
            result1 = []
            for j in range(0, len(result)):
                result1.append(float(result[j]))            #
converts the list value into float
    Chip_res = []
    Supply_volt = []
    Supply_curr = []
    Supply_pow = []
    TC_V1 = []
    TC_V2 = []
    TC_V3 = []
    TC_V4 = []
    TC_V5 = []
    TC_T1 = []
    TC_T2 = []
    TC_T3 = []
    TC_T4 = []
    TC_T5 = []
    for k1 in range(0, len(result1), Col):
        Chip_res.append(float(result1[k1]))
#    for k2 in range(1, len(result1), 10):
#        Supply_volt.append(float(result1[k2]))
#    for k3 in range(2, len(result1), 10):
#        Supply_curr.append(float(result1[k3]))
    for k4 in range(3, len(result1), Col):
        Supply_pow.append(float(result1[k4]))
#    for k5 in range(4, len(result1), 10):
#        TC_V1.append(float(result1[k5]))
#    for k6 in range(5, len(result1), 10):
#        TC_V2.append(float(result1[k6]))
#    for k7 in range(6, len(result1), 10):
#        TC_V3.append(float(result1[k7]))
    for k9 in range(7, len(result1), Col):
        TC_T1.append(float(result1[k9]))
    for k10 in range(8, len(result1), Col):
        TC_T2.append(float(result1[k10]))
    for k11 in range(9, len(result1), Col):
        TC_T3.append(float(result1[k11]))
```

```
    # Calculating the mean and standard deviation of the last 50
samples
    Chip_res_mean_local = np.mean(Chip_res[len(Chip_res)-
N:len(Chip_res)])
    Supply_pow_mean_local = np.mean(Supply_pow[len(Supply_pow)-
N:len(Supply_pow)])
    TC1_mean_local = np.mean(TC_T1[len(TC_T1)-N:len(TC_T1)])
    TC2_mean_local = np.mean(TC_T2[len(TC_T2)-N:len(TC_T2)])
    TC3_mean_local = np.mean(TC_T3[len(TC_T3)-N:len(TC_T3)])


    Chip_res_std_local = np.mean(Chip_res[len(Chip_res)-
N:len(Chip_res)])
    Supply_pow_std_local = np.std(Supply_pow[len(Supply_pow)-
N:len(Supply_pow)])
    TC1_std_local = np.std(TC_T1[len(TC_T1)-N:len(TC_T1)])
    TC2_std_local = np.std(TC_T2[len(TC_T2)-N:len(TC_T2)])
    TC3_std_local = np.std(TC_T3[len(TC_T3)-N:len(TC_T3)])


    Chip_res_mean.append(Chip_res_mean_local)
    Supply_pow_mean.append(Supply_pow_mean_local)
    TC1_mean.append(TC1_mean_local)
    TC2_mean.append(TC2_mean_local)
    TC3_mean.append(TC3_mean_local)

    Chip_res_std.append(Chip_res_std_local)
    Supply_pow_std.append(Supply_pow_std_local)
    TC1_std.append(TC1_std_local)
    TC2_std.append(TC2_std_local)
    TC3_std.append(TC3_std_local)

    if S_type == 1:
        h=open("Output_SurfaceType=NW_"+str(time.strftime("%d-%m-
%Y"))+"_HeatInput=_FlowRate="+str(int(flow_rate))+".txt", 'a')

h.write('{}\t{}\t{}\t{}\t{}\t{}\t{}\t{}\t\n'.format(str(Chip_res_
mean_local), str(Supply_pow_mean_local), str(TC1_mean_local),
str(TC1_std_local), str(TC2_mean_local), str(TC2_std_local),
str(TC3_mean_local), str(TC3_std_local)))
        h.close()
    elif S_type == 2:
        h=open("Output_SurfaceType=MP_"+str(time.strftime("%d-%m-
%Y"))+"_HeatInput=_FlowRate="+str(int(flow_rate))+".txt", 'a')

h.write('{}\t{}\t{}\t{}\t{}\t{}\t{}\t{}\t\n'.format(str(Chip_res_
mean_local), str(Supply_pow_mean_local), str(TC1_mean_local),
str(TC1_std_local), str(TC2_mean_local), str(TC2_std_local),
str(TC3_mean_local), str(TC3_std_local)))
        h.close()
    else:
```

```
        h=open("Output_SurfaceType=Plain_"+str(time.strftime("%d-
%m-%Y"))+"_HeatInput=_FlowRate="+str(int(flow_rate))+".txt", 'a')

h.write('{}\t{}\t{}\t{}\t{}\t{}\t{}\t{}\t{}\t\n'.format(str(Chip_res_
mean_local), str(Supply_pow_mean_local), str(TC1_mean_local),
str(TC1_std_local), str(TC2_mean_local), str(TC2_std_local),
str(TC3_mean_local), str(TC3_std_local)))
        h.close()
    f.close()
```

B.4 TIRM experiments – Acquiring input power

```
import time
import pyvisa as visa

def connect_PSup():
    rm = visa.ResourceManager()
    inst1 =
rm.open_resource('USB0::0x0957::0xA807::US18J1943R::0::INSTR')
    inst1.write('*IDN?')
    print('Connected to ', inst1.read())
    return inst1

def InitialResistance():
#    s.sendall("*RST")
    s.write("*CLS")
    s.write("VOLT 1") # Applied voltage
    s.write("VOLT:PROT:LEV 300")
    s.write("CURR:PROT:STAT 0")
    s.write("OUTP ON") # Turning the output
    print ("\n Calculating resistance of the chip and setting
power...\n")
    s.write("MEAS:CURR?")
    a = s.read()
    s.write("*CLS")
    s.write("MEAS:VOLT?")
    b = s.read()

    a1 = str(a)
    a2 = a1.replace('b\'','')
    a3 = a2.replace('\\n\'','')
    I = float(a3)

    b1 = str(b)
    b2 = b1.replace('b\'','')
    b3 = b2.replace('\\n\'','')
    V = float(b3)

    R = V/I
    print ("Initial resistance = %f" %R)
```

```
    return R

def SetInitialPower(P,R):
    V = ((P*R)**0.5)
    print ("\n Setting voltage to %f\n" %V)
    str1 = "VOLT "+str(V)
    s.write(str1) # Applied voltage
    time.sleep(5)
    print ("The power has been set to %f" %P)

def SetPower(P,R):
#    s.sendall("OUTP ON")
    V = ((P*R)**0.5)
    print ("\n Setting voltage to %f\n" %V)
    str1 = "VOLT "+str(V)
    s.write(str1) # Applied voltage
    time.sleep(2)
    print ("The power has been reset to %f W" %P)

def CheckResistance():
    print ("\n Checking resistance...")
    #time.sleep(5)
    s.write("MEAS:CURR?")
    a = s.read()
    s.write("MEAS:VOLT?")
    b = s.read()

    a1 = str(a)
    a2 = a1.replace('b\'','')
    a3 = a2.replace('\\n\'','')
    I = float(a3)

    b1 = str(b)
    b2 = b1.replace('b\'','')
    b3 = b2.replace('\\n\'','')
    V = float(b3)

    R = V/I
    Par = [R, V, I]
    return Par

def close():
    time.sleep(2)
    s.close()

########################
#     MAIN PROGRAM     #
########################

#s = serial.Serial("COM5", 9600, xonxoff = True) #For Windows
#p = serial.Serial("/dev/ttyUSB0", 9600, xonxoff = True) #For
Linux
```

```
s = connect_PSup()

print ("Enter the HEAT INPUT in W:")
P = float(input())
##power=100

# User Input: Check for first run
print ("Is this first run? (1 - Yes; 0 - No)")
flag = int(input())

if flag == 1:
    R_i = InitialResistance()                #
initialresistance() - User-defined function to calculate the
initial resistance
else:
    text = open("temp1", "r")
    data = text.read()                      #reads all the data
into a single string 'data'
    R_i = abs(float(data))
    pass

SetInitialPower(P, R_i)                            # setpower() -
User-defined function to calculate the voltage based on changing
resistance
time.sleep(10)                                          #clearing
and resetting buffer
Resistance = []

for i in range(0,15):
    Par = CheckResistance()
    Resistance_local = Par[0]
    V_local = Par[1]
    I_local = Par[2]
    Power = V_local*I_local
    Resistance.append(Resistance_local)
    SetPower(P,Resistance[i-1])
    h=open("TIRM_experiments_"+str(time.strftime("%d-%m-
%Y"))+"_HeatInput="+str(int(P))+".txt",'a')
    h.write('{}\t{}\t{}\t{}\n'.format(str(Resistance_local),
str(V_local), str(I_local), str(Power)))
    h.close()
    time.sleep(1)

close()
```

Appendix C

ImageJ Macro

The following macro was used with ImageJ for image processing. Please refer to the ImageJ User Guide to obtain a deeper understanding of the commands used (https://imagej.nih.gov/ij/docs/guide/).

```
run("8-bit");
run("Set Scale...", "distance=996 known=6.06 unit=mm global");
makeRectangle(0, 214, 802, 414); // Crop area may vary for different power settings
run("Crop");
getStatistics(area, mean, min, max, std, histogram)
if (mean>=100) {
        setAutoThreshold("Default");
        setOption("BlackBackground", false);
        run("Convert to Mask");
  } else {
        setAutoThreshold("Default");
        //run("Threshold...");
        getThreshold(lower,upper);
        setThreshold(lower,upper*1.5);
        setOption("BlackBackground", false);
        run("Convert to Mask");
  }
run("Set Measurements...", "area perimeter limit redirect=None decimal=3");
run("Analyze Particles...", "display summarize");
```